Taihoro Nukurangi

Coastal stability in the South Taranaki Bight - Phase 2

Potential effects of offshore sand extraction on physical drivers and coastal stability

Prepared for Trans-Tasman Resources Ltd

Updated November 2015

Authors/Contributors:
Terry Hume
Richard Gorman
Malcolm Green
Iain MacDonald

For any information regarding this report please contact:

Dr Terry M Hume
National Projects Manager
Principal Scientist - Coastal Geomorphology
+64-7-856 1729
terry.hume@niwa.co.nz

National Institute of Water & Atmospheric Research Ltd
Gate 10, Silverdale Road
Hillcrest, Hamilton 3216
PO Box 11115, Hillcrest
Hamilton 3251
New Zealand

Phone +64-7-856 7026
Fax +64-7-856 0151

NIWA Client Report No:	HAM2013-082
Report date:	October 2013
NIWA Project:	TTR12203

Contents

Tables

Figures

Reviewed by

Murray Hicks

Approved for release by

David Roper

Formatting checked by

Executive summary

Trans-Tasman Resources Ltd (TTR) propose to extract ironsands from the seabed in the South Taranaki Bight of the West Coast, North Island. The proposed extraction area is in the Exclusive Economic Zone (EEZ) between 22 km and 35 km off the coast of Patea and in 25 to 55 m water depth. The plan is to extract up to 50 million tonnes of seabed sediment per year with an annual production of up to 5 million tonnes of iron ore concentrate separated from this for export. A 10 year sand extraction plan has been developed with the intention of applying for a 20 year mining permit for the area.

The change in shape of the seabed morphology due to the sand extraction operation will take the form of elongate pits (or lanes) about 1 m deep some mounds <9 m tall, and pits to 10 m deep on the margins of the lanes. Depressions (pits or lanes due to sediment extraction) and mounds (de-ored sand returned to the seabed) in/on the seabed can potentially affect waves by refraction (bending the wave path) and diffraction (lateral dispersion of wave energy) and locally by shoaling (changing the wave height) them as they pass over the modified seabed. Any such changes in the wave field at the extraction site will be propagated shoreward, leading to changes in wave conditions nearshore with potential consequent changes in shoreline processes (erosion and accretion) inshore of the operations. Extracting sand from the seabed can also alter the patterns of sand transport across the inner shelf seabed and potentially reduce the supply of sand to the nearshore and beaches. The magnitude of the changes will depend on the scale of the operations. How long the effects on the shoreline last will depend on how quickly the pits/lanes infill and the mounds diminish in height after extraction ceases.

This report makes an assessment of the effects of sand extraction on the landforms and geomorphic character of the shore, physical drivers (waves and currents) of coastal processes, sediment processes and coastal stability. It is based on studies made of the natural landforms and geomorphic character along the 140 km long stretch of coast between Opunake and Whanganui, a review of information on historical rates of seacliff erosion along the shore, an analysis of beach profile monitoring data from eight sites along the shore, measurements of currents and waves, and wave modelling to assess the potential effects of seabed modifications due to extraction on wave characteristics and sediment transport potential at the shore.

The coast between Opunake and Wanganui forms part of a 200 km-long littoral cell extending from Cape Taranaki in the north to about Kapiti Island in the south. It is characterised by near-vertical, actively eroding, 35 – 50 m tall seacliffs and narrow beaches formed at the base of the cliffs and in coastal re-entrants. Sand beaches can develop in relatively low energy zones provided by the shallow coastal re-entrants. Here they comprise small, narrow (about 100 m wide), mixed sand and gravel or pure sand beaches built at the base of tall cliffs. The sand accumulates as a thin veneer, possibly only metres thick over the rocky shore platform, sometimes exposed at low tide at the base of the beach, left by the retreating cliff line. Some of these re-entrants form where streams and small rivers emerge on the coast and others where the geology allows that section of the coastal cliffs to erode and retreat more rapidly than adjacent sections of cliffs. Here small, narrow, dune systems can develop. The beach profile data show that the sediment in these beaches is very mobile. The beach level goes up and down 1 – 2 m and the beach face shows excursions back-and-forth of about 10 – 40 m over time scales of weeks and months. The beach face erodes during storms (with vertical elevation changes of 2 m) and builds up in the calmer periods between, so that the sand is “parked-up” temporarily before it is redistributed along the shore. Sediment transfers along the coast are driven primarily by waves, with the principle direction of energy transfer by the waves from NW to SE along the shore. Sand is driven back-and-forth, NW and SE along the shore, depending on the wave direction, but primarily to the SE. Big waves and a surf zone 100’s of metres wide provide a highway for sand to move from re-entrant to re-entrant along the shore and bypass the small protruding headlands and river mouths.

The study made an assessment of how sand extraction activities might affect the geomorphic character, erosion and physical drivers and processes along the shore. The key findings relating to consenting requirements are summarised as follows:

The natural landforms and geomorphic character of the beaches is unlikely to change due to sand extraction: Geomorphic character of the beaches is determined by environmental setting, tide range, grain size and wave climate. Environmental setting, tide range and grain size will not be changed by sand extraction. Wave climate will be modified as waves pass over the pits and mounds on the seabed but as our wave modelling has shown the extent of the modification will be minor and will not alter the existing geomorphic character which under natural conditions exhibits a large degree of temporal and spatial variation in wave characteristics.

Public access to the marine environment will not be adversely affected: Coastal erosion will not change significantly in the future with sand extraction offshore and therefore public access to the marine environment will not be hindered. However, continual cycles of cut and fill on the beaches due to natural events will hinder access from time to time as they have in the past.

There will be no adverse effects from deposition of substances to the foreshore and seabed: Very fine sands and muds generated by sand extraction operations will not make the beaches muddy. While sediment plumes from extraction operations will reach the shore, the absence of mud beach sediments despite that fact that river flood events deliver 2 M m^3 of fine sediment and turbid water to the shoreline and adjacent to beaches, indicates that if deposited on the beaches fine sediment will be quickly winnowed from the beach sediment by wave action and transported offshore not build-up on the beach.

Extraction will not adversely affect physical drivers and processes that cause coastal change – Currents: Bathymetric irregularities such as the pits (to 10 m deep) and mounds (to 9 m tall) at the extraction sites form features of the order of several kilometres long and 0.5 km wide and of a size to naturally occurring ridges on the seabed. While producing a localized effect on currents they are not expected to impact prevailing or ambient currents and flow characteristics. Weak cross shore currents and modelling of sediment dispersal of sands from the extraction area suggest that there is little connection between seabed sediments in the extraction area and the surf zone, and seabed sand in the area of the extraction operations some 22 to 35 km off the coast is not a significant source for sand on the beaches. Therefore, sand extraction will not have significant effects on sand supply to the beaches and will not promote beach erosion.

Extraction will not adversely affect physical drivers and processes that cause coastal change – Waves: Wave modelling of six scenarios of offshore wave conditions showed that close to shore at the 10 m isobath, which is about the seaward edge of the surf zone, the magnitude of change as a percentage of the baseline value (no seabed modifications) for significant wave height and mean period to be less than 9.2% for the case 1 bathymetry modifications (representing the most extensive seabed modifications containing the greatest number of pits and mounds and represents extraction over 10 years with no pit infilling or mound deflation or slumping by natural processes). The changes were about 4.8% for other cases. Changes in wave direction are generally less than 1 degree (increasing locally to 3 degrees west of Manawapou) which is insignificant when compared to the natural variability in wave approach throughout the year. A 12-month long simulation of waves which allows for the effects of the bathymetry modifications on the wave characteristics to be tested for case 1 over a wide sampling of the local wave climate, showed that close to shore at the 10 m isobath, the bathymetry modifications introduce a mean decrease (by less than 5 cm) in significant wave height on the coast near Patea, with smaller increases (of less than 2.5 cm) further west, mean wave period decreases (by less than 0.1 seconds) in the vicinity of Patea, and increases (by less than 0.06 seconds) to the west, mean wave direction is slightly decreased (i.e., changes in an anticlockwise sense) on average along the majority of the coast. The differences associated with the bathymetry changes are considerably less than the natural range of variability in baseline (no extraction) values.

Extraction will not adversely affect physical drivers and processes that cause coastal change – Longshore transport: Longshore transport is the process by which waves arriving at an angle to the shore drive sediment along the shore and is a primary mechanism for supplying sand to beaches from alongshore sources. Statistics derived from the 12-month model simulations were used to evaluate a criterion for “accepting” or “rejecting” a potential sand extraction site based on a range of one-half the standard deviation ($\pm$0.5s) about the mean (m) of the longshore transport potential. The analysis showed that for the case 1 (worst case situation in terms of potential effects on the shore), the differences in longshore wave energy flux and sediment transport potential as a consequence of the proposed extraction lie well within the envelope of one-half a standard deviation of the natural longshore transport potential. That is to say, the extraction proposed by TTR for the case 1 situation meets the criterion for “accepting” a sand extraction site.

Effects on the risk of accelerated coastal erosion and accretion along the region's coastline and modification to natural hazard processes will not be significant: Beach profile surveys and observations made at eight sites between Ohawe and Kai Iwi, spanning a stretch of about 70 km of coast show that the beaches are very active. The level of the beach fluctuates up and down 1 – 2 m and the beach face shows excursions back and forth of about 10 – 40 m over time scales of weeks and months in response to erosion during storm events and the calmer periods of beach building in between. These fluctuations occur under natural conditions (no extraction) as a consequence of this environmental setting. For a shoreline of this character, that experiences a wide variety of wave conditions and large variability in sediment transport rates and changes in sand storage on the beaches, the level of acceptable impacts from sand extraction offshore should be relatively high, compared for instance to a shore that experiences a more limited range of wave conditions. Changes in wave characteristics due to pits and mounds on the seabed resulting from sand extraction operations some 22 – 35 km offshore have been shown to have no significant influence on the wave climate in the nearshore. Also the extraction site has been shown to have no significant connection with the coast in terms of sand supply. It follows that sand extraction offshore will have no significant effect on the beaches in terms of the natural processes of erosion and accretion which under natural conditions are highly variable.

Modelling the fate of the pits and mounds over time found that at 50-m water depth it will take around 500 years for waves and currents to reduce the pit volume by 90% (around 300 years for 50% reduction). At the same depth, it will take around 350 years for 90% of the mound to be deflated (150 years for 50% deflation). Infilling and deflation will be faster at 35-m water depth: 100 years for 90% infilling of the pit (50 years for 50% infilling), and 20 years for 90% deflation of the mound (10 years for 50% deflation).

Information relating to TTR’s additional scientific work undertaken since 2014 has been provided and the conclusions is this report remain valid.

1 Introduction

1.1 Background

Trans-Tasman Resources Ltd (TTR) has secured permits and is prospecting for ironsands on the seabed in the South Taranaki Bight of the West Coast, North Island. The prospecting licence areas lie within and seaward of the 12 nm territorial sea. The proposed extraction area is in the Exclusive Economic Zone (EEZ) between 22 km and 35 km off the coast of Patea. The plan is to extract up to 50 million tonnes of seabed sediment per year with an annual production of up to 5 million tonnes of iron ore concentrate separated from this for export. A 10 year mining plan has been developed with the intention of applying for a 20 year mining permit for the area. TTR are applying for Crown Minerals Act (CMA) mining permits and environmental (EEZ) marine consents under the new EEZ legislation in 2013. NIWA is undertaking a range of biogeophysical studies in the South Taranaki Bight for TTR to meet the likely requirements of consenting procedures to extract sand from the seabed.

1.2 Project description

The ironsand extraction area will be 22 to 35 km offshore from Patea and in 25 to 55 m water depth and in the vicinity of the area named the Rolling Ground on LINZ chart NZ45 (Figure 1-1).

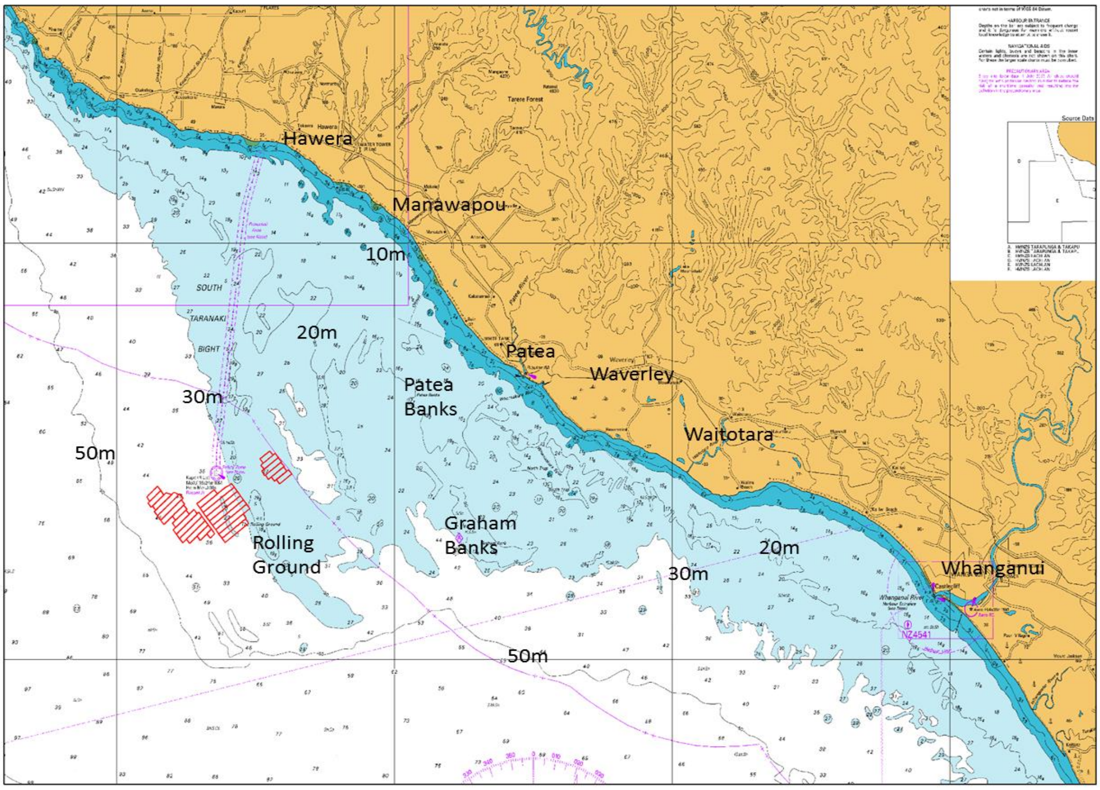

Figure 1-1: The Patea Shoals and sand extraction site. Excerpt from LINZ chart NZ45 (http://charts.linz.govt.nz/tifs/nz45.tif).

Sand will be extracted by a Submerged Sediment Extraction Device (SSED) connected to and operated remotely by a single FPSO (Floating Production Storage Offloading) vessel. The SSED, located on the sea bed, is connected to the FPSO via an umbilical delivery pipe (power cable, hydraulic hose and delivery hose). The SSED operates under the stern of the FPSO at the base of the defined “ore body” and cuts to the full depth face[1] (creating a ‘lane’ approx. 3 to 10 m deep and approx. 10 m wide) in a single operation, meaning there is no need to return. The process of excavation and backfilling is simultaneous. Sediment is pumped to the FPSO for processing. A winching system locates the FPSO relative to the SSED, which will be working 300 m × 300 m blocks in a predetermined sequence. De-ored (remaining) sediment (about 90% of the total dredged volume) will be slurried by pipe from the bow of the FPSO to largely backfill the cut lanes as the FPSO follows the SSED.

A single FPSO vessel contains the extraction, processing and de-ored sediment management functions of the project. Sediment from the SSED is processed on board to separate iron ore concentrate from the rest of the sediment using on board magnetic separators and grinding mechanisms. The final iron ore concentrate is dewatered to ~10% moisture and stored temporarily on the FPSO before being slurried with fresh water to the FSO (Floating Storage Offloading) from the FPSO. From the FSO the iron ore tranships to a cape-sized ore carrier either in the open sea or at a sheltered area if necessary, depending on weather conditions. The cape-size vessel delivers the iron ore concentrate to China and other export markets. Figure 1-2 sets out the proposed TTR mine plan layout, illustrating the three extraction blocks, and the corridors or lanes in which extraction will take place. The seabed morphology resulting from the sand extraction operation will take the form of elongate pits (or lanes) and mounds at the start and ends of the lanes. Remnant mounds (maroon) have heights of 8 m or 9 m, remnant pits have depths of 9 m or 10 m, while backfilled lanes (light green) are assumed to have a depth of 1 m and are about 500 m wide. The pits and mounds at the end of each lane are about 300 m long (SW-NE) and 500 m wide (NW-SE). The bathymetry cases number anticlockwise from top left panel (Case 01) to bottom right panel (Case 08).

The proposed direction of each extraction corridor (or lane) is parallel to the prevailing SW wind/wave direction as this is the preferred alignment for directional control of both the FPSO and the SSED. The lanes are about 500 m wide and vary in length from about 1 – 14 km. The SSED will extract sand from under the stern of the 330 m long FPSO and the de-ored sediment will be discharged to the seabed (to backfill the cut) from the bow of the FPSO as the vessel is winched backwards and toward the NE.

The resulting pattern of cut and fill in general terms is for a pit to about 300 x 500 m dimension and 10 m depth at the SW end of the lane, a depression 1 m deep in the backfilled lane (90% of the extracted volume will be returned), and a mound about 300 x 500 m dimension and 10 m tall at the NE end of the lane. However the exact pattern of cut and fill, and therefore whether there are 10 m deep pits and 10 m tall mounds at the start and end of each lane, depends on the path that the operation takes.

[1] Cut made from seabed surface to full depth of the ore body.

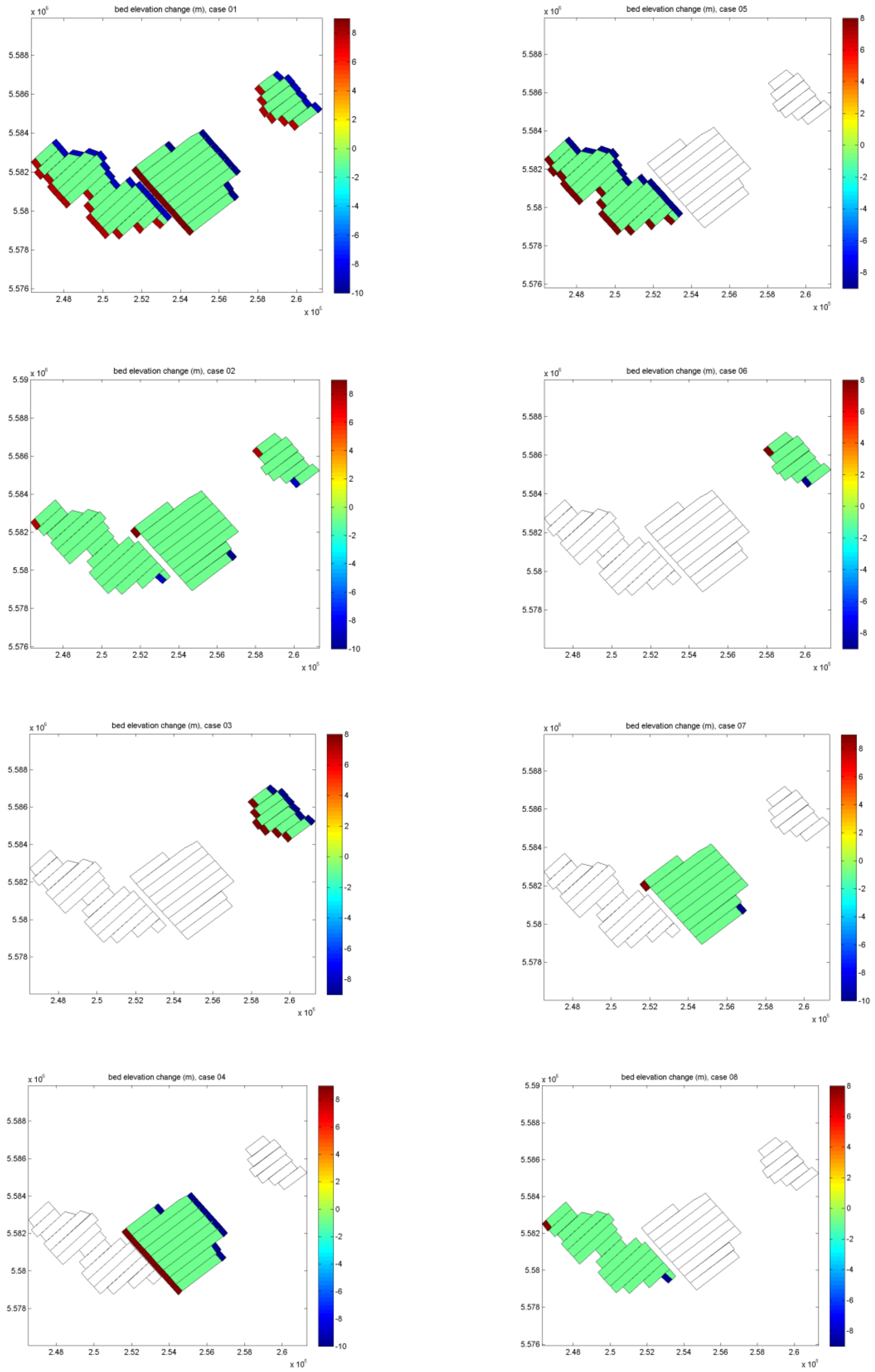

Figure 1-2: Outlines of the 8 hypothetical bathymetry changes tested. The bathymetry cases number from the top left panel (Case 01) to bottom left (Case 04) to bottom right panel (Case 08).

1.3 Potential effects on coastal stability

Depressions (pits or lanes due to sediment extraction) and mounds (de-ored sand returned to the seabed) in/on the seabed can potentially affect waves by refraction (bending the wave path) and diffraction (lateral dispersion of wave energy) and locally by shoaling (changing the wave height) them as they pass over the modified seabed. Such changes in the wave field at the extraction site may be propagated shoreward, leading to changes in nearshore wave conditions with consequent changes in shoreline processes (erosion and accretion) inshore of the operations. The magnitude of the changes will depend on the scale of the operations (the location, volumes extracted and depth/height of the pits/lanes/mounds). How long the effects on the shoreline last for will depend on how quickly the pits/lanes infill and the mounds smooth out after extraction ceases.

Extracting sand from the seabed can also alter sand transport across the inner shelf seabed and potentially reduce the supply of sand to the nearshore and littoral drift system resulting in shoreline erosion. The magnitude of the changes will depend on the location and scale of the extraction (the location, depth of water, volumes extracted, shape and depth of the lanes and size of the mounds) and how connected the offshore extraction sites are with the nearshore and beach. How long the effects on the shoreline last for will also depend on how quickly the seabed lanes infill with sand from the surrounding seabed.

A related issue is that of future climate change and whether it will influence wave conditions and sediment transport processes to such an extent that it will change the predicted effects of sand extraction at the shore.

A search of policy and plans (provided by the draft evidence analysis by G. Venus for TTR in November 2011) relevant to TTR's consent application found that the key issues relating to potential changes to the coastal physical environment depend on whether TTR's activities will:

- Adversely affect natural landforms, physical drivers, erosion, geomorphic character, influences that humans have and/or are having on the coast.
- Adversely affect public access to the marine environment.
- Involve the deposition of substances to the foreshore and seabed (such as mud deposition on the beaches from the dredge plume).
- Adversely affect physical drivers and processes that cause coastal change.
- Adversely affect the risk of accelerated coastal erosion or accretion along the region's coastline.
- Modify natural hazard processes.
- And whether the effects of climate change and associated sea level rise will affect any of the above.

1.4 This report

TTR requested that NIWA undertake an assessment of the effects of sand extraction on physical drivers and coastal stability of the South Taranaki Bight and provide information in a technical report that will inform and underpin evidence to be presented at the consent hearing. This work was carried out under Schedules T and T V1.

Phase 1 of the work (Schedule T, reported in Hume et al. 2012) provided an assessment of the stability of the shoreline of the South Taranaki Bight extending 140 km from about Opunake to Wanganui. It reviewed the historical and present day rates of change in the position of the shoreline and temporal variations in sand storage on the beaches, in order to provide a context and scale against which to gauge the potential effects of the sand extraction of the offshore seabed.

Phase 2 of the work (Schedule TV1, this report) integrates that information along with investigations of how extraction might alter wave and sediment transport potential at the shore and in the proposed extraction area and therefore the potential effects of offshore sand extraction on coastal stability.

2 Coastal geomorphology and processes

Hume et al. (2012) provide a description of the coastal geomorphology and rates of erosion and accretion for four sections that extend along the 140 km of coast, between Mangahume (near Opunake) Stream and Whangaehu (near the mouth of the Wanganui River) (Figure 2-1).

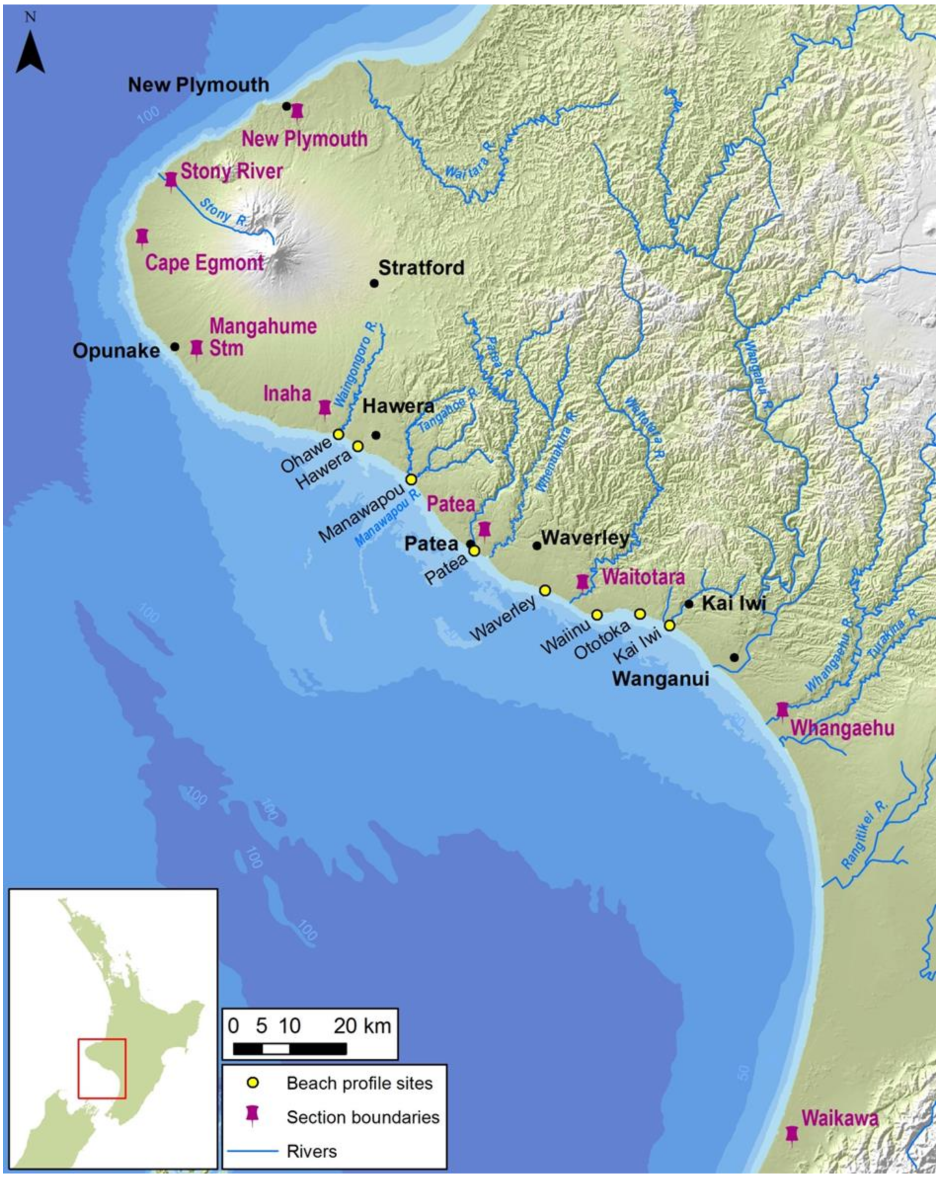

Figure 2-1: Study area and beaches surveyed (yellow dots).

2.1 Geology

The northern section (Opunake to Inaha) is dominated by the Mount Taranaki Ring Plain volcanics and lahar deposits. The lahar deposits extend south to about the Inaha Stream near Hawera. Uplift of the ring plain and changes in sea level plus the energetic westerly wave climate have caused parts of the coast to be cliffed, although the cliffs are generally small and eroding slowly. In places, the cliffs are taller where they are capped by erodible overlying sedimentary sections. This shoreline consists mainly of cliffs and rocky, wave-cut intertidal platforms with a thin veneer of sand or gravelly sand, cobbles or boulders. Areas of rocky seabed with thin, intermittent sand cover are common in the nearshore. Terrestrial sediment inputs to this section of shoreline are dominated by erosion of volcanic materials from Mount Taranaki (Taranaki Regional Council 2009). There are many small streams but few rivers, resulting in only small quantities of sediment being delivered to the coast and limited occurrence of sand beaches and dunes at the shore. The southern section (Inaha Stream to Wanganui) has seen continual tectonic uplift (McGlone et al. 1984) to produce a coast characterised by almost continuous near-vertical, 30 – 50 m tall, sedimentary seacliffs. Sandy beaches occur at the base of the cliffs, and in small re-entrants[2] where streams emerge on the coast. In places there is reef exposed in the low tide part of the beach or in the nearshore.

2.2 Beach morphology and sand storage

Major coastal landform types are summarised in Figure 2-2.

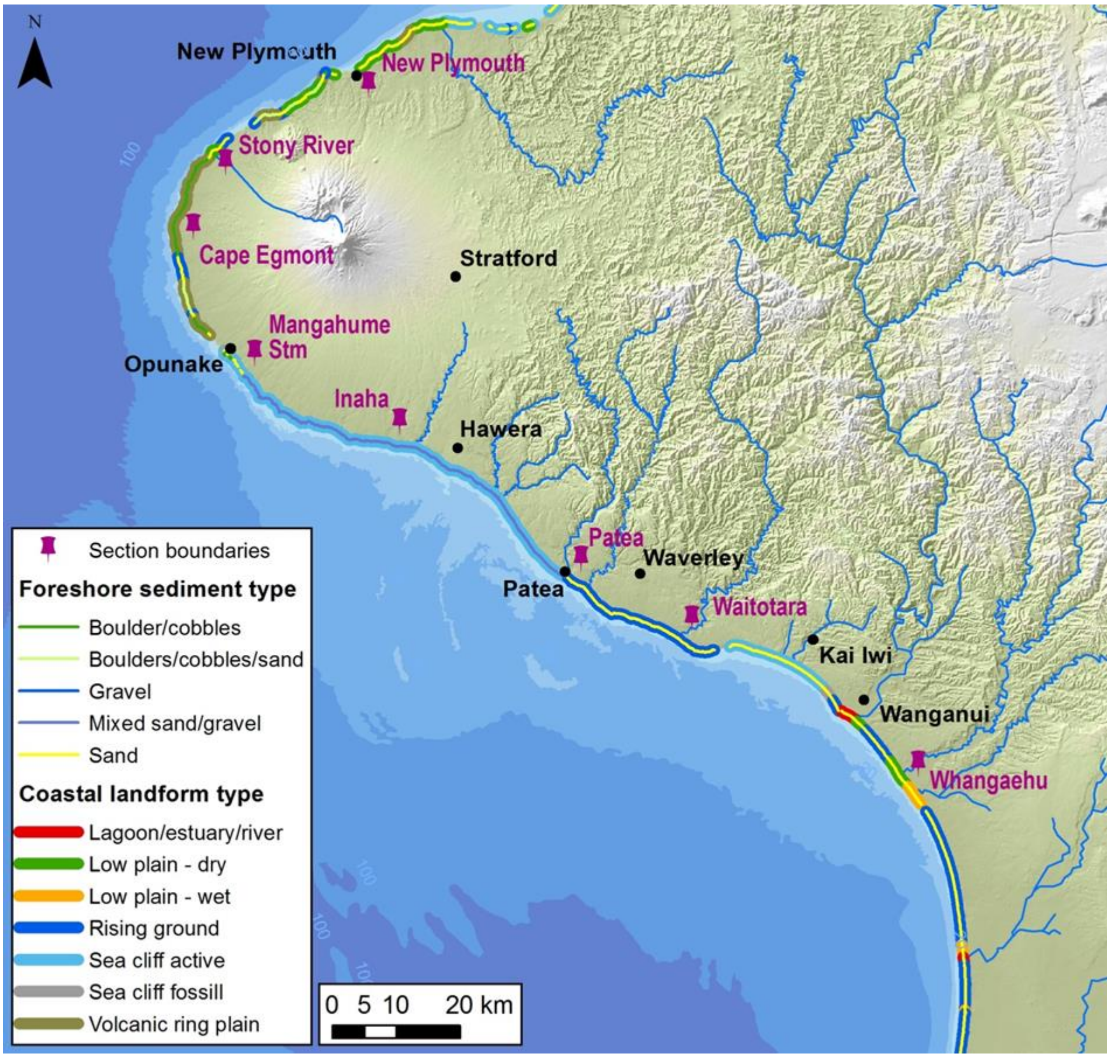

Figure 2-2: Major coastal landform types & foreshore sediment types (source: Coastal Explorer, NIWA website).

[2] Prominent indentations into a coastline.

Along the South Taranaki Bight, between Inaha and Wanganui, narrow beaches form at the base of the tall near-vertical seacliffs and in coastal re-entrants that occur along about 70% of the coast. Wider beaches with small dune systems form where cliffs give way to rising ground. Beaches are absent where cliffed coast is exposed directly to waves. South from Inaha to Patea the foreshore is largely mixed sand and gravel with cobbles and boulders on parts of the shore. To the south of Patea sandy foreshore predominates in front of the cliffs. Sandy foreshore backed by foredunes, with transgressive dunes extending inland over rising ground, characterise the coast between Patea and Waitotara and Waiinu. South of Waiinu sandy foreshore fronts the cliffs. To the south of Wanganui the foreshore is largely sandy beach backed by dunes extending inland over rising ground.

Beaches develop in relatively low energy zones provided by the shallow coastal re-entrants. They comprise small narrow (about 100 m wide) mixed sand and gravel or pure sand beaches built at the base of the seacliffs (Figure 2-3 and Figure 2-4). Beach sand accumulates as a thin veneer, possibly only metres thick over the rocky shore platform left by the retreating cliff line and also on occasions in a nearshore bar. The rocky shore platform is sometimes exposed at low tide at the base of the beach.

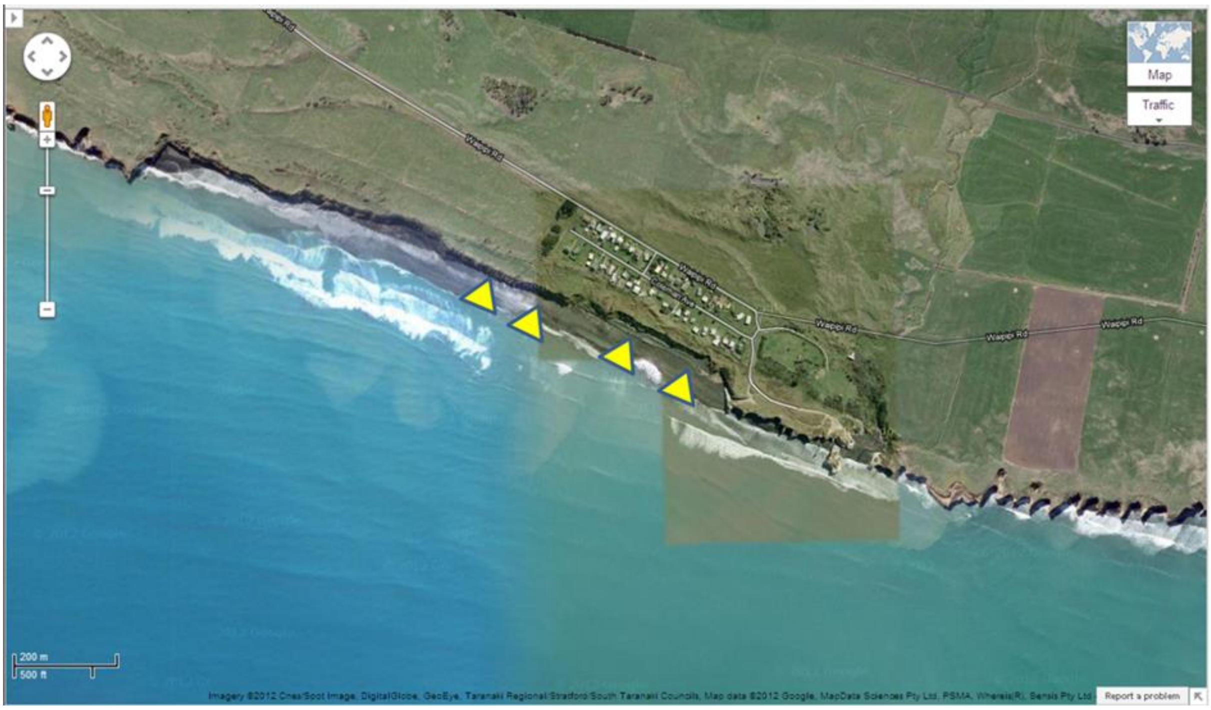

Figure 2-3: Beach formed in a coastal re-entrant at Waverley. The yellow triangles show where the beach profiles were surveyed each month.

Some re-entrants form where streams and small rivers emerge on the beach (e.g., beach profile sites Ohawe, Hawera, Manawapou, Kai Iwi). Others form where the geology allows that section of the coastal cliffs to erode and retreat more rapidly (e.g., beach profile site Ototoka and Waverley Figure 2-3) than adjacent sections of seacliffs.

Figure 2-4: Mixed sand and gravel beach at the base of the seacliffs at Hawera.

As the beach profile data show, the sediment in these beaches is very mobile, it erodes during storms and builds up in the calmer periods between, so that the sand is parked-up temporarily before it is redistributed along the shore. Small unvegetated dunes form in the re-entrants at the stream mouths, but are absent from the base of the cliffs where high tides, combined with storm surge and large waves reaching right up to the seacliffs and enhanced by backwash from the cliffs (Figure 2-5) mean that the entire beach is subjected to erosion,. Erosion is further enhanced by ground water and surface water flow from the cliffs. This flows through the beach where it emerges as seepage lines and springs at mid to low tide level[3] (Figure 2-6).

Figure 2-5: Waves reflecting off the coastal cliffs at Patea.

[3] Wet beaches erode more easily than dry beaches because of their high water content.

Figure 2-6: Ground water springs emerging on the beach at Ototoka.

Sand is stored in foredunes along a sandy section of coast, where there are no cliffs, that runs from the Patea River to about Waiinu (Figure 2-7 and Figure 2-8). Sand comprises transgressive dunes formed when sand picked-up from the beach by strong winds, prevalent on this coast, is blown inland to smother low lying topography and rising ground. However, these inland dunes are now, in most part, stabilised under farm pasture.

Figure 2-7: Waiinu Beach. The yellow triangles show where beach profiles were surveyed. Transgressive dunes are visible in farmland in the left of the image.

Figure 2-8: Sand dunes at Waiinu Beach.

A small amount of sand is stored in bars and spits at the mouths of the rivers such as the Patea and Wanganui (Figure 2-9).

Figure 2-9: Patea River mouth and beach.

Pits dug in the beach show alternating layers of coarse and fine sediments made up of fine black sands and shelly pebbly sands and gravels (Figure 2-10). This provides evidence of the intermittent injection of coarse sediment from seacliff collapse, and that the beach face is substantially reworked and sorted during wave events (producing a coarse lag) and the calmer periods (producing a build-up of finer material) in between. There is a considerable proportion of gravelly sands making up the beach in some locations.

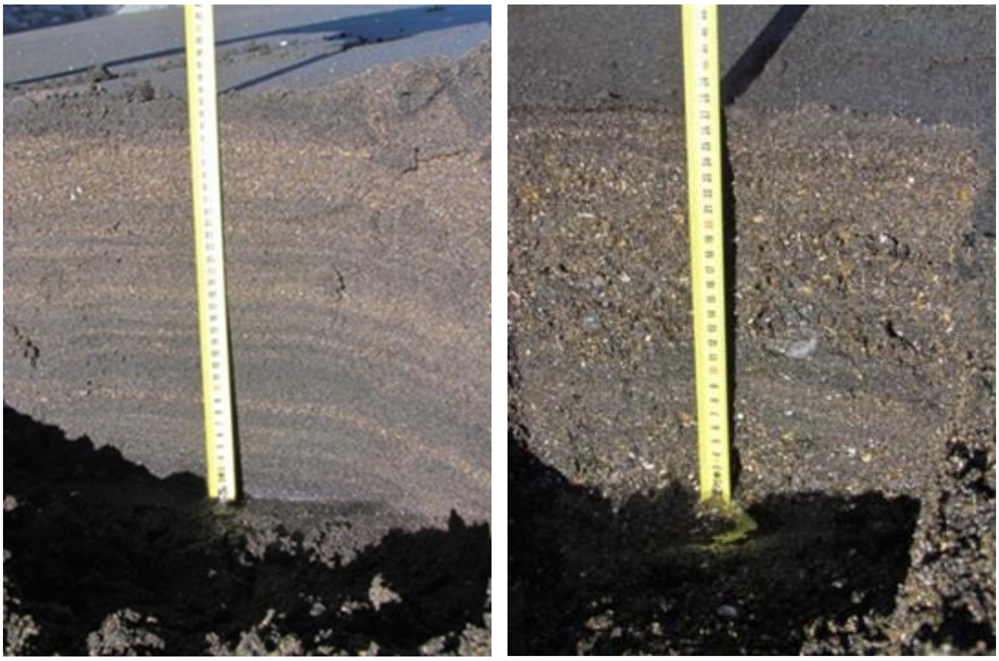

Figure 2-10: Pits dug in the beach at Manawapou show alternating layers of coarse and fine sediments (ruler scale in centimetres).

The overall trend in beach sediment grain size along the South Taranaki Bight coast is for the beach sediments to be coarser in the north than in the south. In the north at Ohawe and Hawera (Figure 2-4), where the beaches are largely poorly sorted gravelly medium to coarse sands and fine gravels, with much of the coarser material appearing to derive from cliff collapse. In the south the beaches are sandier being primarily moderately sorted gravelly medium sands.

In the north at Ohawe and Hawera the beaches also tend to be narrower and steeper (slope ranging from 4 – 7 degrees) than the beaches to the south (e.g., Waiinu Figure 2-8) (slope ranging from 2 – 4 degrees). This is a reflection of the grain size of the sediment (coarse sediment builds steeper beaches) and also sediment supply. Seacliff erosion is the primary sediment source for the coarser sediment.

2.3 Historical and present day shoreline stability

The historical record of rates of seacliff retreat is sparse, patchy and discontinuous for this coast (Hume et al. 2012). For instance, in the Inaha to Patea coastal section, one study in 1978 of all historic information (field measurements, maps, aerial photographs from the late 1800s to mid-1970s) points to cliff erosion rates ranging from 0.05 m/yr – 1.1 m/yr. Erosion was recorded at Ohawe (0.63 m/year) and at two sites in Manawapou (0.64 m/year and 0.67 m/year). Another study in 1996, which used a map from 1871 and aerial photos from 1951, 1972, 1984 and 1993 as well as field measurements in 1996, reported long-term cliff retreat as 0.48 m/year (1871 – 1996), but the rate of retreat varied between 0.03 m/year (1951 – 1984) and 0.35 m/year (1984 – 1996). Apart from a report of cliffs near Waipipi (near Waverley) eroding at 0.35 m/year made by comparing surveys from 1906 to 2005, there are no measurements of historical rates of erosion or accretion on the shore between Patea and Waitotara/Waiinu. Active erosion of the cliffs is expected, as they are composed of soft sedimentary material, largely Pliocene Wanganui Series mudstones, sandstones, shellbeds, limestone and conglomerates. In places this is capped with Pleistocene conglomerates, marine sand, dune sand, volcanic sand and lignite bands. The cliff face erodes catastrophically by slumping, also aided by groundwater seepage through the strata and joints in the cliffs, large waves undercutting the base and removing slumped material and perhaps tectonic activity such as earthquakes. The overall picture is one of active erosion all along the cliffed shore.

Figure 2-11 summarises shoreline stability in the South Taranaki Bight in historical times.

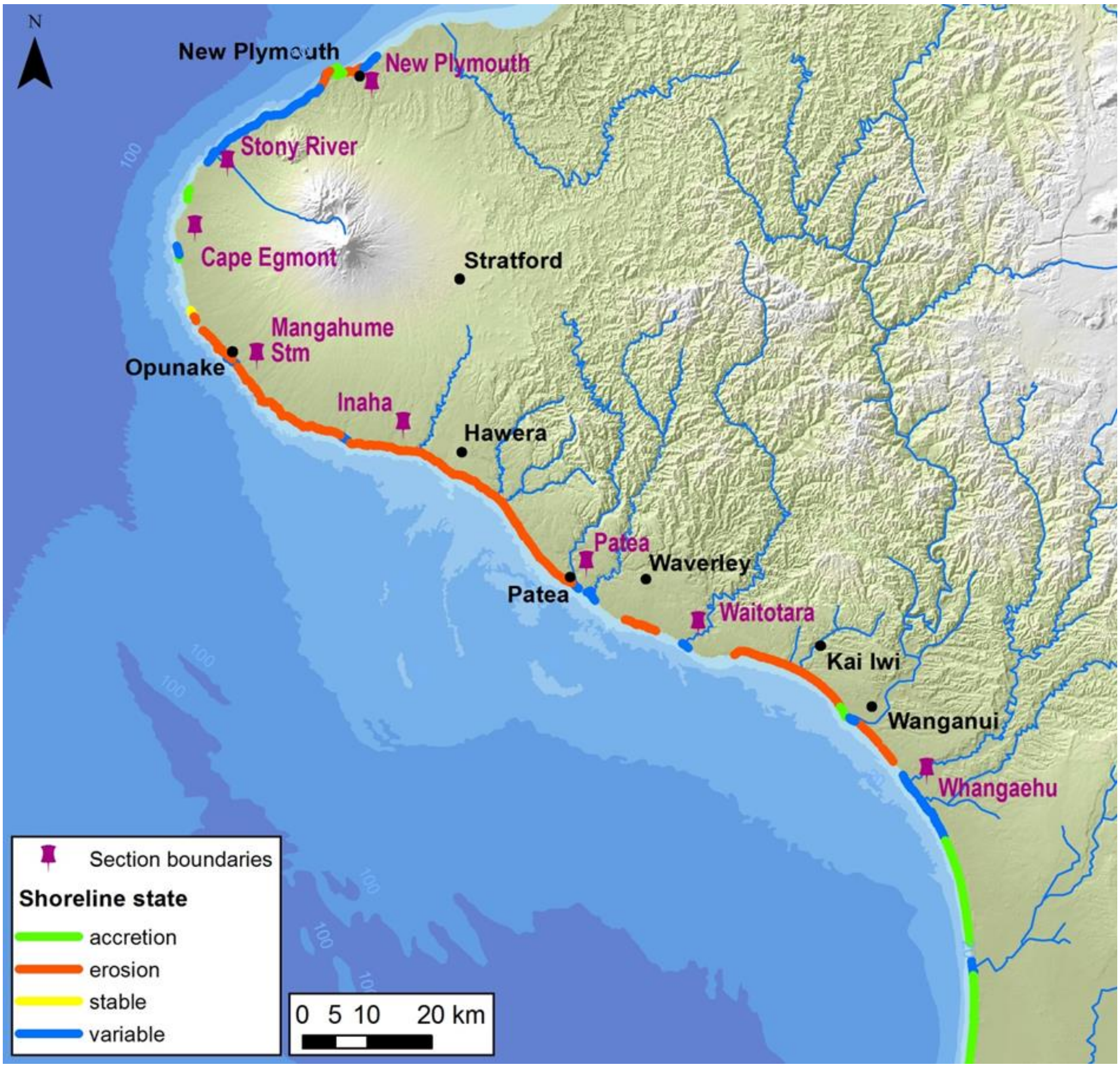

Figure 2-11: Shoreline stability in the South Taranaki Bight in historical times. Areas for which there are no data are left blank. (Map modified from MacDiarmid et al. 2010).

Present day changes in beaches along the 70 km of shoreline between Ohawe and Kai Iwi are evidenced in the (albeit short) record of beach profiles surveyed monthly at 8 sites for one year (June 2011 to April 2012) as part of TTR investigations (Hume et al. 2012 and MacDonald et al. 2012a). These record changes in the level of sand on the narrow, largely sandy beaches, fronting 30 – 50 m tall near-vertical cliffs, or sometimes located in small coastal re-entrants such as stream and river mouths, that are a feature of about 70% of this coast. These beaches appear to form a thin veneer of sediment, possibly only metres thick over the rocky shore platform left by the retreating cliff line, and there is generally no space between the back beach and cliff for a dune to form. The beach profile data show there is a very high flux of sand both across shore and longshore through the system. The beach elevation goes up and down 1 to 2 m and the beach face shows excursions back and forth of about 10 – 40 m over time scales of weeks and months. For example, Figure 2-12 and Figure 2-13 show the beach change measured over a period of 11 months at Ototoka Beach. The ‘spaghetti’ plots of profiles (e.g., Figure 2-12) show the actual survey profiles and how the elevation (in metres above a datum, where 0 = Taranaki MSL) of the beach changes with distance (in metres from a start point) between the dune/high tide and low tide levels. The plot of all the profiles together displays the range of fluctuation over the entire survey record. The plots show only a small vertical change in elevation of the beach surface above high tide. In the middle of the beach the elevation has fluctuated by more than 2 metres. Near low tide mark the change is of the order of a metre. The plots also show beach berms[4] building on the upper beach above high water and swash bars[5] on the lower beach. Swash bars typically signify shoreward migrating pulses of sand.

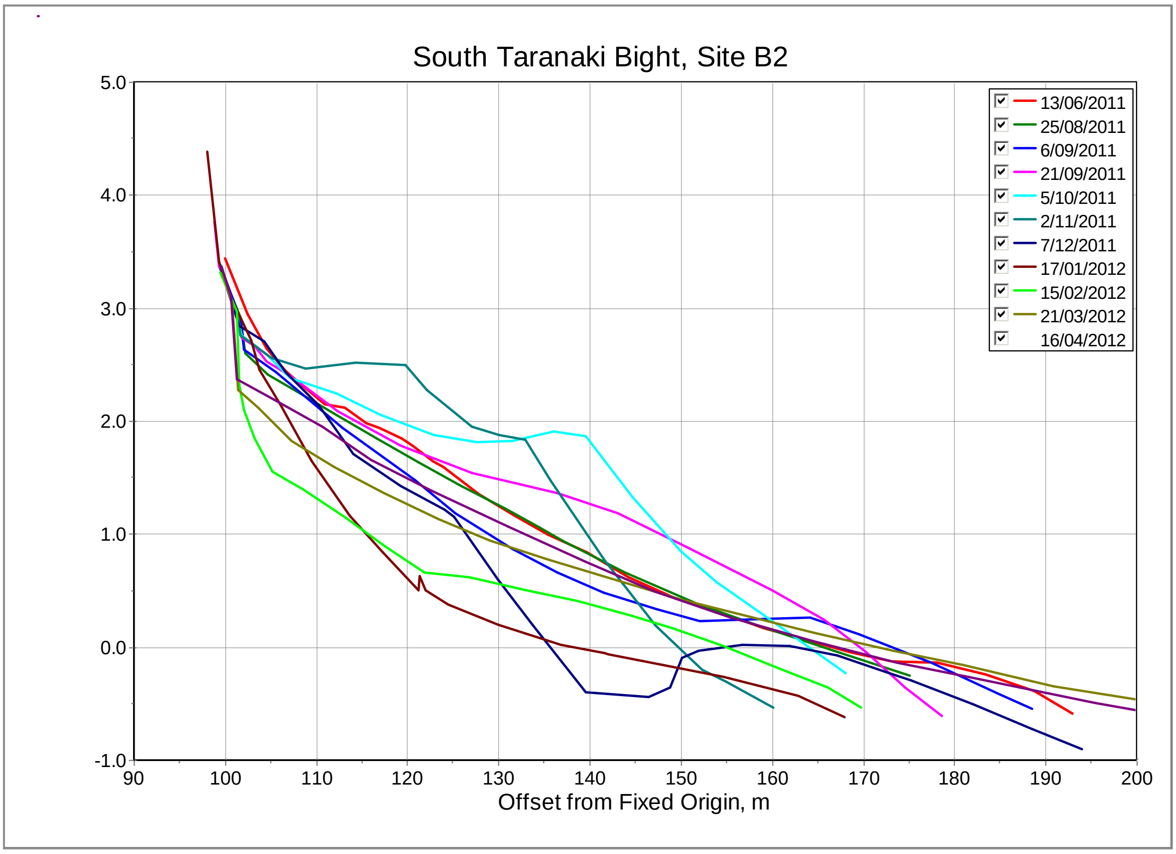

Figure 2-12: Spaghetti plot of 11 profile surveys at Ototoka. The elevation is in metres above Taranaki Mean Sea Level datum.

The excursion distance plots (e.g., Figure 2-13) show the amount of horizontal back and forth movement of the beach face at selected heights above a datum. The example below shows a very small amount of back and forth movement of the beach face on the upper beach (at 3

[4] Nearly horizontal plateaus on the beach face or backshore, formed by the deposition of sand by wave action.
[5] Low broad sandy bars formed by sediment in the surf and swash zones, separated by linear depressions, or runnels, running parallel to the shore. See Figure 2-8 right-hand panel.

m elevation) and more back and forth movement (about 32 m) on the mid-beach (at 1.0 m elevation). The left and right hand end of the box represent the 25th and 75th percentile. The ends of the whiskers represent the minimum and maximum of the data. Any data not included between the whiskers are plotted as outliers with dots or stars. The red line defines the mean profile shape.

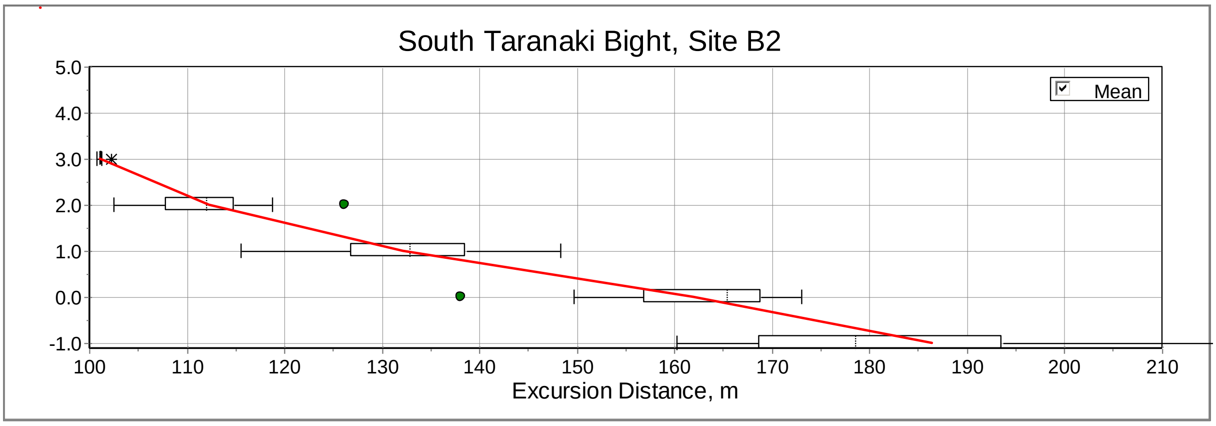

Figure 2-13: Excursion distance plot showing the amount of back and forth movement of the beach face at 0.5 m intervals above Taranaki MSL.

Sand also moves back and forth in swash bars between the nearshore bars and the beach, and alongshore as slugs of sediment in low broad shore normal bars. Storms do not always result in erosion on all parts of the beach, as a consequence of these pulses of sand moving along shore or sand shifting back-and-forth from one end of the beach to the other. This highly variable geomorphology is driven by the large waves on this coast that run right to the top of the beach in storms and high tides.

Changes in sand volumes measured by beach profile surveys at the eight sites between Ohawe and Kai Iwi over the period June 2011 to April 2012 show that the net change in beach volume and sand storage varies from erosion at some sites to accretion at others (Table 2-1).

Table 2-1: Sand volume changes from beach profile data - June 2011 to April 2012.

Site	Length of beach spanned by profiles (m)	Net change in beach volume (m^3/km of shoreline)	Total amount of sand moving on and off the beach (m^3/km of shoreline)
Ohawe	500	+23,200	137,000
Hawera	530	-7,300	67,000
Manawapou	680	+25,700	247,000
Patea	360	-15,900	169,500
Waverley	400	+4,700	109,600
Waiinu	400	-10,100	100,500
Ototoka	630	-6,100	205,100
Kai Iwi	420	-5,300	203,300

The 11 months of profile data show no spatial or temporal pattern of change in erosion and accretion along the shore, just considerable change. The total movements of sand on and off the beach over the year were of the order of at least 6-times to 39-times greater than the net change in sand storage. The beaches are continually changing as large volumes of sand enter and leave and are redistributed in the beach system.

2.4 Littoral processes and sediment budget

It is relevant in the context of predicting the impacts of offshore sand extraction on the shoreline to examine sediment transfers in the coastal sand system and the sediment budget. Sand transfers are the pathways that sand takes as it is driven through the system by waves and currents. The sediment budget is a consideration of the rate at which sand is brought into the system versus the rate at which sand leaves the system and the balance of inputs and outputs. Developing the budget involves evaluating the relative importance of the various sediment sources and losses to the nearshore zone and a comparison with any gain or loss in the observed rate of beach erosion or accretion. Developing a budget may offer an explanation of the effect of cutting off any of these sediment sources. Sand extraction offshore may for instance significantly reduce the supply of sand to the beach and cause a sediment deficit in the littoral cell resulting in beach erosion. However, for reasons outlined in the following discussion we consider that an analysis of sediment budget is of little value in predicting the effects of sand extraction on the shoreline.

The coastal sand system or littoral cell is large, extending over 200 km from Cape Taranaki in the north to about Kapati Island in the south. It is bounded in the north where the wave energy flux diverges at Cape Egmont, being directed NE to the north of the Cape and SE to the south of the Cape. It is bounded in the south at Kapiti Island where a wave shadow zone and the consequent salient in the lee of the island restricts sand movement further south. The landward boundary of the littoral cell is well defined as the shoreline. The seaward boundary is more diffuse and some distance offshore where cross shore sand transfers between the beach and the seabed become insignificant. At a finer scale within this littoral cell there are smaller obstacles to sand transport along the shore such as small headlands, which can temporarily inhibit sand transport. The large size of the sand system and the distance offshore of the extraction means that any potential effects of extraction, while focussed inshore of the extraction site, are potentially spread over a large length of shoreline and therefore minimised.

Sediment transfers along the coast are driven primarily by waves. Considerations of wave climate later in this report show that the large waves are found off the western end of Taranaki Peninsula: wave height decreases along the coast to the south with increasing shelter from SE swell (Figure 5-2). This pattern is also seen in the average of wave energy flux (Figure 5-3), which is a vector quantity reflecting the magnitude and direction of energy transfer by the waves, which shows relatively strong energy transfer (principally from the WSW) at the northern end of the South Taranaki Bight, while further south there is less energy transfer as the more southerly energy components become blocked. The orientation of energy flux is significant, as wave energy reaching the coast at an oblique angle will drive longshore sediment transport to the SE. With the exception of the sand stored in the transgressive dunes, the sand storage on beaches in the South Taranaki Bight is rather transient in a system of highly connected sand storage units. Sand is exchanged on and off the shore between the beaches and the nearshore bars. Sand is driven to the NW and SE along the shore depending on the wave direction, but primarily to the SE. Big waves and a surf zone 100’s of metres wide provide a highway for sand to move from re-entrant to re-entrant along the shore and to bypass the river mouths.

The coastal sediment budget in the South Taranaki Bight is primarily made up of inputs from longshore transport into the area, onshore transport, river transport and seacliff erosion. Sediment is lost through longshore transport out of the area, wind transport away from the beach, offshore transport and solution and abrasion and potentially through activities such as sand extraction. While it is easy to identify the inputs and outputs of sediment they are much more difficult to quantify.

Wave modelling described later in the report provides statistics for the longshore component of the wave energy flux vector, which sets the longshore sediment transport potential and the onshore component. The longshore sediment transport potential is large and of the order of 20 M m^3/yr in the NW at Ohawe. It reduces southeastward along the shore to about 2 M m^3/yr at Kai Iwi (Figure 5-28). The onshore wave energy flux is also large (Figure 5-27). The geomorphic evidence however does not support significant longshore or onshore transport, there being little beach development in the north of Patea where the transport potential is greatest. That is to say, the longshore transport potential outstrips the rate of supply and inhibits sand accumulation in front of cliffs. However sand can build beaches in places where it can shelter from waves in low energy areas provided by the coastal re-entrants. In summary, longshore and cross shore transport into the area is difficult to estimate and does not supply reliable numbers for a sediment budget. Furthermore, and as will be reported in section 4 of this report, sand extraction will be a long distance offshore and largely disconnected from littoral system. Therefore, the cross shore flux of sand from the seabed in the extraction site to the shore will be a relatively small (albeit unquantified) term in the budget.

Rivers along the project shore deliver sediment derived primarily from erosion of sedimentary and volcanic rocks in their catchments. These sediment inputs are visible as nearshore plumes of muddy water extending several kilometres offshore and along the coast from the river mouths after flood events (Figure 2-14). Estimates of the suspended sediment yield from the major rivers is given in Table 2-2. Most sediment derives from the Patea, Whenuakura, Waitotara and Whanganui Rivers. The total annual yield from the rivers is of the order of 2,930,600 m^3/yr (or 5,861,200 tonnes/yr). However we do not know what proportion of the input from each of these rivers is beach grade material and therefore this is an unreliable estimate for the budget.

Figure 2-14: Plumes of muddy water being discharged from the rivers after a flood event. Note the muddy suspended sediment is being transported to the north and west by tide and currents, while coarser beach grade sediment is driven primarily to the south by wave energy.

Table 2-2: Mean water flows and mean annual suspended sediment inputs from the rivers flowing into the study area. The data is sourced from NIWA's WRENZ model (http://wrenz.niwa.co.nz/webmodel/), and has been compiled in a manner described in Hicks et al. 2011). A factor of 2 has been used to convert sediment yield in tonnes/yr to cubic metres/yr.

River	Upstream area (km^2)	Mean flow (m/s)	Sediment yield (tonnes/yr)	Sediment yield (m^3/yr)
Waiaua River (Opunake)	46.4	3.6	4900	2450
Kaupokonui Stream	146.3	8.6	9700	4850
Waingongoro R (Ohawe)	233.1	7.8	9100	4550
Tangahoe River	285.1	4.2	43900	21950
Manawapou River	120.9	1.9	15000	7500
Patea River	1048.5	30.4	310600	155300
Whenuakura River	465.3	9.9	275900	137950
Waitotara River	1162.0	23.3	475400	237700
Kai Iwi Stream	191.0	1.8	16900	8450
Whanganui River	7113.8	229.0	4699800	2349900

Seacliff erosion supplies sand to the beaches and nearshore seabed, where it is sorted and redistributed by waves and currents (Figure 2-15). The cliffs, that comprise 70% of the shoreline, are composed of soft sedimentary material, largely Pliocene Wanganui Series mudstones, sandstones, shell beds, limestone and conglomerates. In places this is capped with Pleistocene conglomerates, marine sand, dune sand, volcanic sand and lignite bands. The cliff face erodes catastrophically by slumping, also aided by groundwater seepage though the strata and joints in the cliffs, large waves undercutting the base and removing slumped material and perhaps tectonic activity such as earthquakes. Slumped sediment and rock protects the cliff base until wave action removes the debris (Cowie et al. 2009, TRC 2009). Our field observations made during monthly profile surveys suggest that the soft sedimentary sandstone and mudstone components of this material break down rapidly: slumped deposits seen at the toe of the cliffs on one survey may have been partially washed away by waves on a subsequent visit. The total supply of sandy and gravelly material to the beaches has been estimated by assuming that if cliffs averaging 30 m tall were eroding at 0.3 m/yr over 70% of the 100 km of coast between Ohawe and Wanganui, then the supply of sediment to the coast would be about 630,000 m^3/yr. There is considerable uncertainty in estimating this statistic as it is derived from a few measurements of erosion rate and multiplied by a long distance. Furthermore, we do not know what proportion of the input from each of these rivers is beach grade material and therefore this is a poor estimate for the budget.

Figure 2-15: Seacliff erosion by catastrophic failure feeds sediment to the beaches and nearshore.

In summary, while the analysis of the sediment budget is useful in providing a picture of processes and scale, we consider that an analysis of the budget is of little value in predicting the effects of sand extraction on the shoreline of the South Taranaki Bight because of uncertainties involved in the calculations of the budget terms.

3 Seabed morphology and sediments

The inner continental shelf out to 50 m depth is about 30 km wide off Hawera, widens to about 40 km off Patea, and then narrows immediately south of this to about 20 km wide to as far south as Whanganui (Figure 3-1). Its topography between about 10 m and 50 m depth is characterised by banks and shoals and ridges off Patea and Waitotara (Figure 3-2). These features extend seawards from about the 20 m isobath, making angles of c.110 – 170 degrees to the shore. At their seaward end in 30 – 40 m water depth they curve in a SE to E direction. As described later in this report, these features tend to be aligned with the prevailing (net) current which flows NW to SE through the region. They can be large in size with individual features offshore from Patea more than 20 km long and 5 – 10 m in elevation.

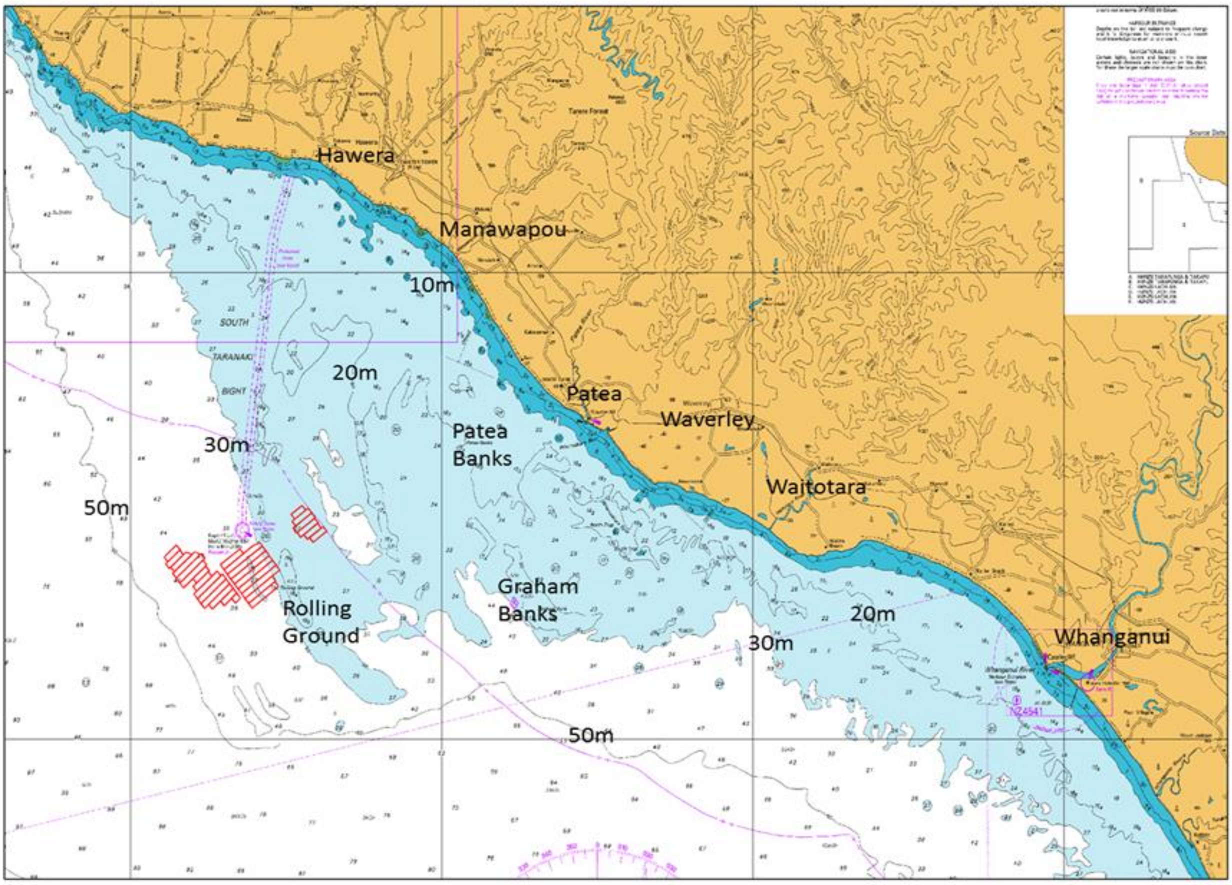

Figure 3-1: Seabed morphology and bathymetry in the South Taranaki Bight.

The description of the nature and origin of seabed morphology that follows has been extracted from Orpin (2009). According to Lewis (1979), seabed features determined from sidescan sonar and high-resolution seismic surveys form two basic types: (1) those in the nearshore zone are mainly erosional and (2) those offshore are depositional. Erosional features occur at <30 m water depth, such as rock outcrops and ancient buried river valleys from differential weathering of the underlying Plio-Pleistocene mudstone. In contrast, at >30 m water depth storm-generated depositional bedforms occur, including ironsand ridges, sand ribbons, symmetrical megaripples and sand waves. The largest sediment bodies are situated immediately southeast of the mouth of the Wanganui River (Figure 3-2). These deposits are 4 – 12 m high, several hundred metres wide, several kilometres long, and aligned subparallel to the coastline. Their surface is composed of ironsand and volcanic pebbles, interpreted to be sourced from Mt Taranaki. These sand ridges are located on relatively flat seafloor.

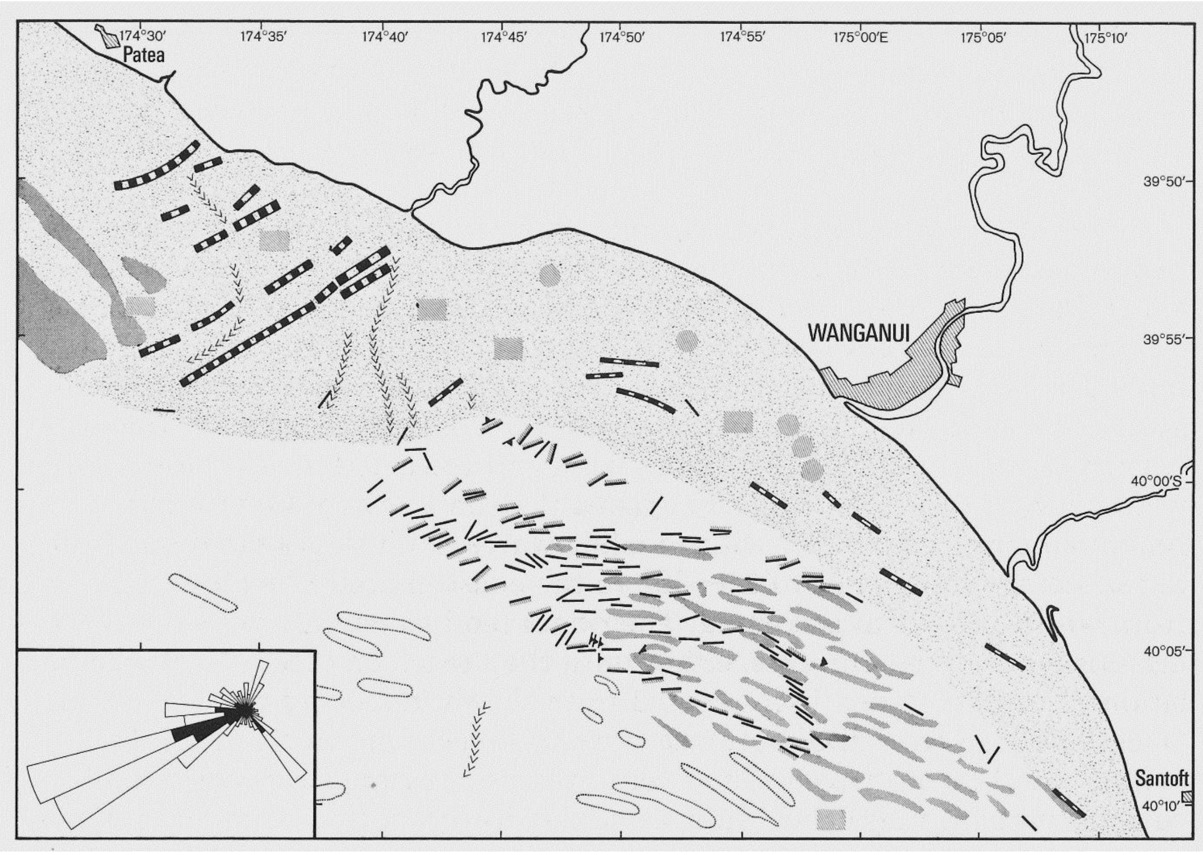

Figure 3-2: A diagrammatic summary of seabed features by Lewis (1979) determined from sidescan sonar and high-resolution seismic surveys. Features close to shore within the stippled belt were interpreted to be erosional. These include rock outcrops (heavy broken lines) and ancient buried river valleys (line of V's). Seaward of the stippled zone, the features were interpreted to be depositional. These include ironsand ridges (grey dense stipple; also summarised in Carter, 1980), sand ribbons (bold lines), symmetrical megaripples (fine lines), and sand waves (arrowed lines). Inset: direction of large waves stirring fine sand at 30 m (white fill) and 50 m (solid black fill). The wave orientation is predominantly west-southwest.

An analysis by Lewis (1979) of the hydrodynamic motions required to create bedforms of this size at 30 – 50 m water depth inferred that they are more likely to be relic features that formed 9,000 – 12,000 years ago as shore-connected shoals. Their location and orientation on the shelf is consistent with the estimated position of the transgressive shoreline at that time (Proctor and Carter 1989; Lewis 1994). Lewis (1979) infers that their formation ceased about 9,000 years ago with rising sea level, when Plio-Pleistocene rock promontories around 25 km west of Wanganui began to act as natural barriers to the supply of ironsand within the littoral drift system. As the sea transgressed the inner shelf, these outcrops of shelly sandstone formed headlands and reefs that dammed the eastward, longshore supply of ironsand. Supply was not re-initiated until present-day sea level was attained c. 6,500 years ago and headlands were eroded back to allow longshore drift to develop once again (but along a new pathway displaced NE to the current shoreline). Ironsand shoals of similar size and morphology have not been described on the modern shoreface.

Within the intervening toughs, between large ironsand ridges, are a complex array of smaller active bedforms, including sand ribbons, ripples (0.1 – 0.5 m wavelength), symmetrical megaripples (1 – 3 m wavelength) and sand waves. These bedforms persist to depths of at least 50 m, and are presumably formed by strong oscillatory currents, approaching 1 m/s, which occur during the passage of large storms.

Sand ridges and dunes, 3 – 12 m in height, occur in two large zones around 100 km^2 in size off Wanganui (cf. Lewis 1979), and as isolated patches <20 km^2 in the area of The Rolling Ground off Patea (Appendix 3B). Data collected during Voyage CR2033 (Nodder 1990) indicates that the bottom topography is a series of northwest-southeast trending, submarine ridges and troughs, composed of coarse sand-gravel, but with a thin, patchy veneer of fine sand. Similar to the ironsand ridges observed off Patea by Lewis (1979), the coarse deposits are believed to have formed during the last phase of the sea level transgression around 8,000 – 10,000 years ago, whereas the fine-sand cover is probably a modern deposit at the seaward edge of the shore-attached sediment prism.

Seabed sediment sediments on the shelf vary from fine sands to gravelly fine sands, although sediments are mostly fine to medium sands, with a general trend of more fine sand to the north and west of the study site and a greater proportion of coarse sand and gravel/shell to the south and west (Figure 3-3). The gravel fraction in the shelf sediments is mostly composed of shell fragments.

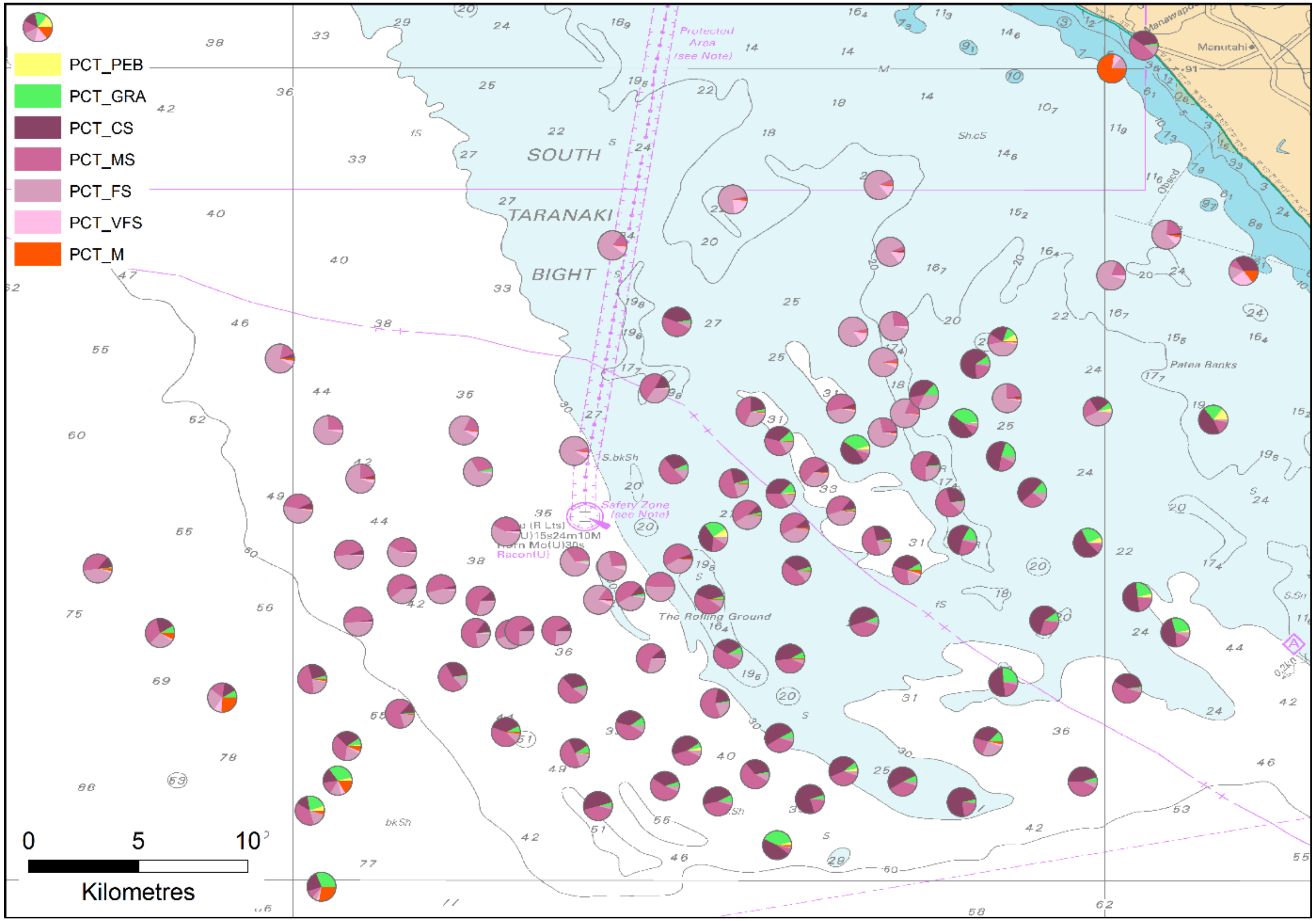

Figure 3-3: Grain size of seabed sediments in the South Taranaki Bight shown as percentages in different size classes. PCT_PEB: pebbles, PCT_GRA: gravel, PCT_CS: coarse sand (500 µm – 1.6 mm), PCT_MS: medium sand (250 µm – 500 µm), PCT_FS: fine sand (125 µm – 250 µm), PCT_VFS: very fine sand (63 µm – 125 µm), PCT_M: mud (<63 µm). Modified after Beaumont et al. 2013 and Anderson et al. 2013.

4 Inner shelf and nearshore currents

Numerical modelling and field measurements reveal strong currents in the South Taranaki Bight region driven by ocean forcings, the tide and wind stress. These currents entrain and transport sediment across the shelf, particularly when aided by seabed stirring by waves.

4.1 Modelled tidal currents

Numerical modelling reported in MacDiarmid et al. (2010), using the NZ Tidal Model on an unstructured grid for the full EEZ and covering the wider Cook Strait area at approximately 1 km resolution, provides a picture of the strength and direction of tidal currents.

Tidal currents flow at up to 0.4 m/s (0.8 knots) in the extensive region of relatively shallow waters off Patea (Figure 4-1). Tidal currents reduce southeast of the Patea Banks, with peak speeds less than 0.1 m/s in nearshore waters between Wanganui and Foxton. Throughout the study region the principal current (or net) direction is generally shore-parallel. There are weak cross-shore minimum currents (transverse to the peak current)[6]. In the shallow waters off Patea the minimum current is less than 0.1 m/s (0.2 knots).

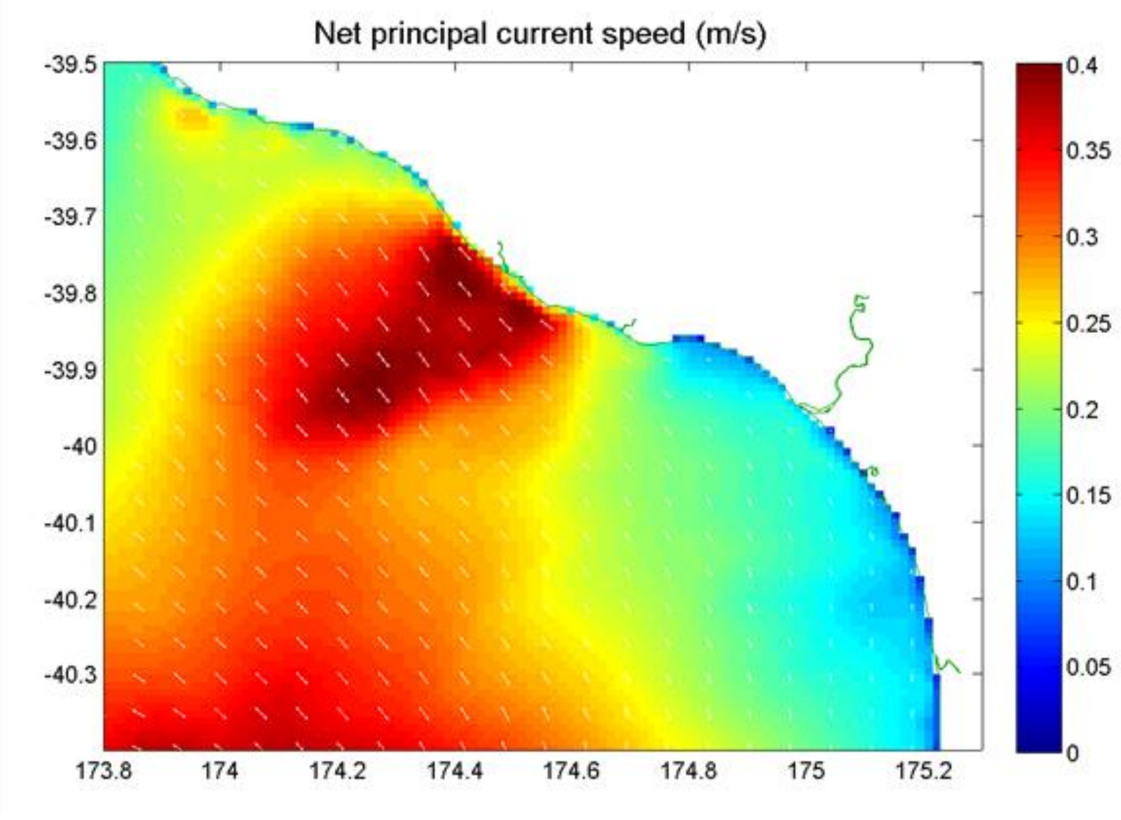

Figure 4-1: Net principal tidal currents in the STB. The maximum speed is shown by the colour scale. The double-headed arrows show the principle flood and ebb directions of flow and are scaled to speed. The nearshore area of high currents lies off Patea. Source MacDiamid et al. 2010.

[6] A single tidal constituent (e.g., M2) has a current vector rotating through an elliptical path during each tidal period. Adding multiple constituents adds multiple tidal ellipses, and the "net" tidal ellipse is the "best fit" ellipse to the total motion. The "principal" speed and direction refer to the semi major axis of this "net" tidal ellipse.

4.2 Field measurements of currents

Currents were measured as part of a programme of field measurements in South Taranaki Bight, involving instrument deployments at several sites for three periods between September 2011 and June 2012 (Figure 4-2). Details are given in MacDonald (2012b). The range of winds experienced during the field programme was typical of the long-term wind climate and included a more extreme weather-bomb event (3 March 2012).

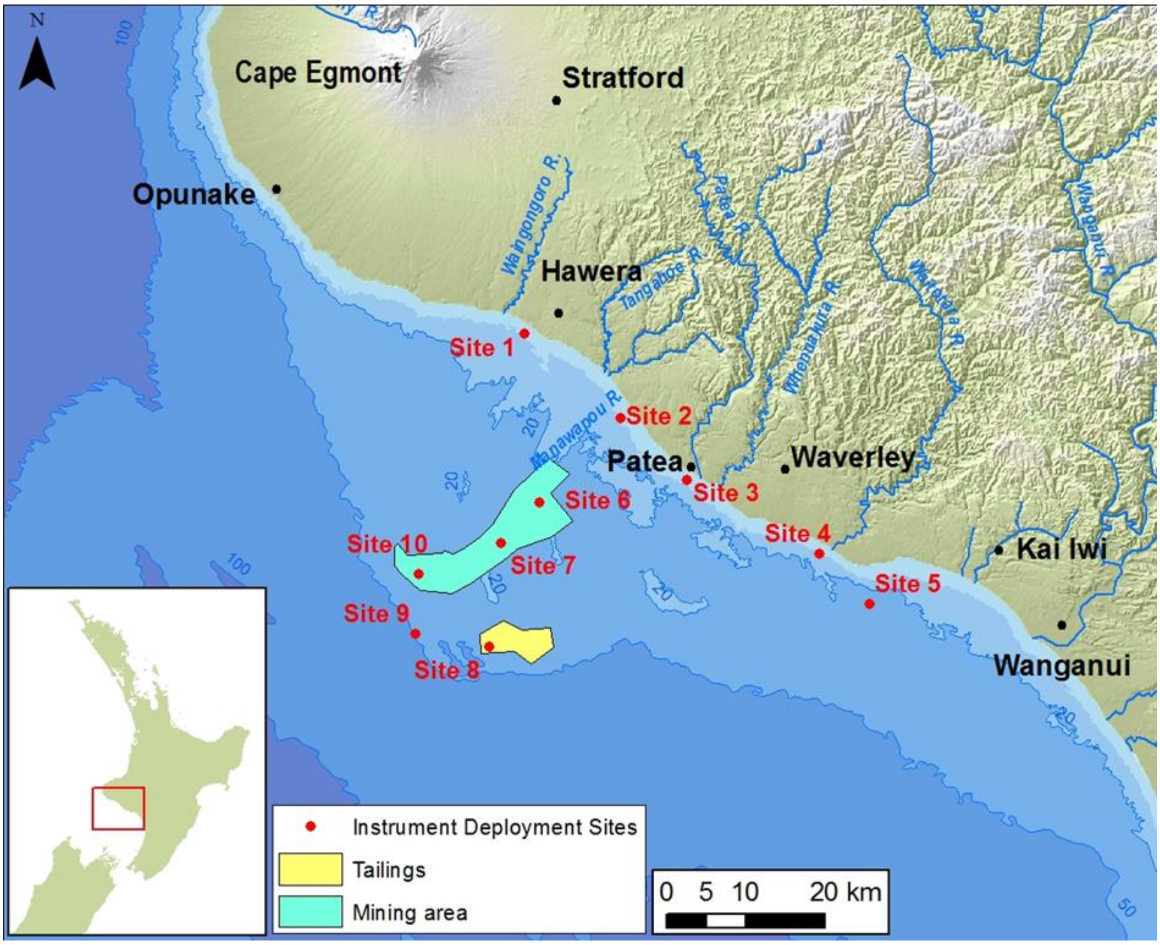

Figure 4-2: Instrument locations in the South Taranaki Bight. Currents were measured at sites 5, 6, 7 and 8. Source MacDonald 2012b**.**

By way of example of the current information the record of currents from one of the two deployments at site 6 in 23 m water depth, on the landward boundary of the sand extraction area, is described below.

The time series plots for the first deployment at Site 6 (S6/D1) are shown in Figure 4-3. Currents were typically less than 0.5 m/s. Near the sea bed, the maximum recorded current speed of 0.65 m/s was measured on 10/11/2011 at 17:15. In the 12-hour period prior, wind speeds ranged between 10.0 and 12.3 m/s (mean 11.2 m/s) with direction from the SE. Higher in the water column, at 16.6 m above bed, the maximum recorded current speed of 0.73 m/s was measured on 10/11/2011 at 17:00 (roughly the same time as the maximum near-bed current). In the 12-hour period prior, wind speeds ranged between 10.0 and 12.3 m/s (mean 11.2 m/s) blowing from the SE.

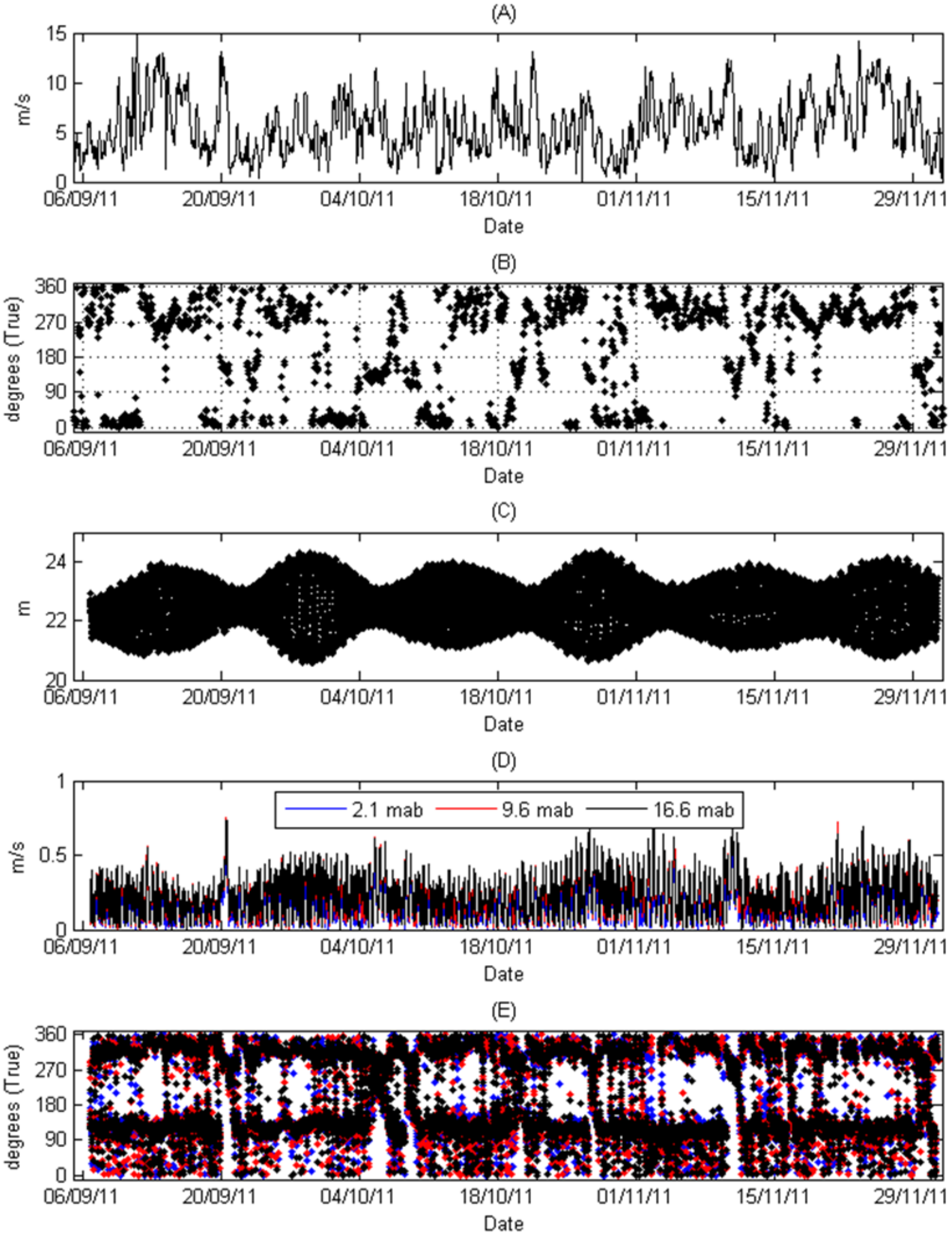

Figure 4-3: Current and wind time series for deployment S6/D1. Panels: (A) wind speed, (B) wind direction (in meteorological convention "blowing from"), (C) water depth, (D) current speed at three elevations above the bed (mab = metres above bed), and (E) current direction (in oceanographic convention "flowing to").

Scatter plots of the velocity vector components from the three elevations above the sea bed are shown in Figure 4-4. Currents measured during the S6/D1 deployment had a principal orientation of SE – NW, but are directed slightly more towards the S than those measured at the inshore coastal site 5. As expected, Figure 4-4 also shows that current speeds increased with elevation above the sea bed. The figures show the prevailing current flows shore parallel.

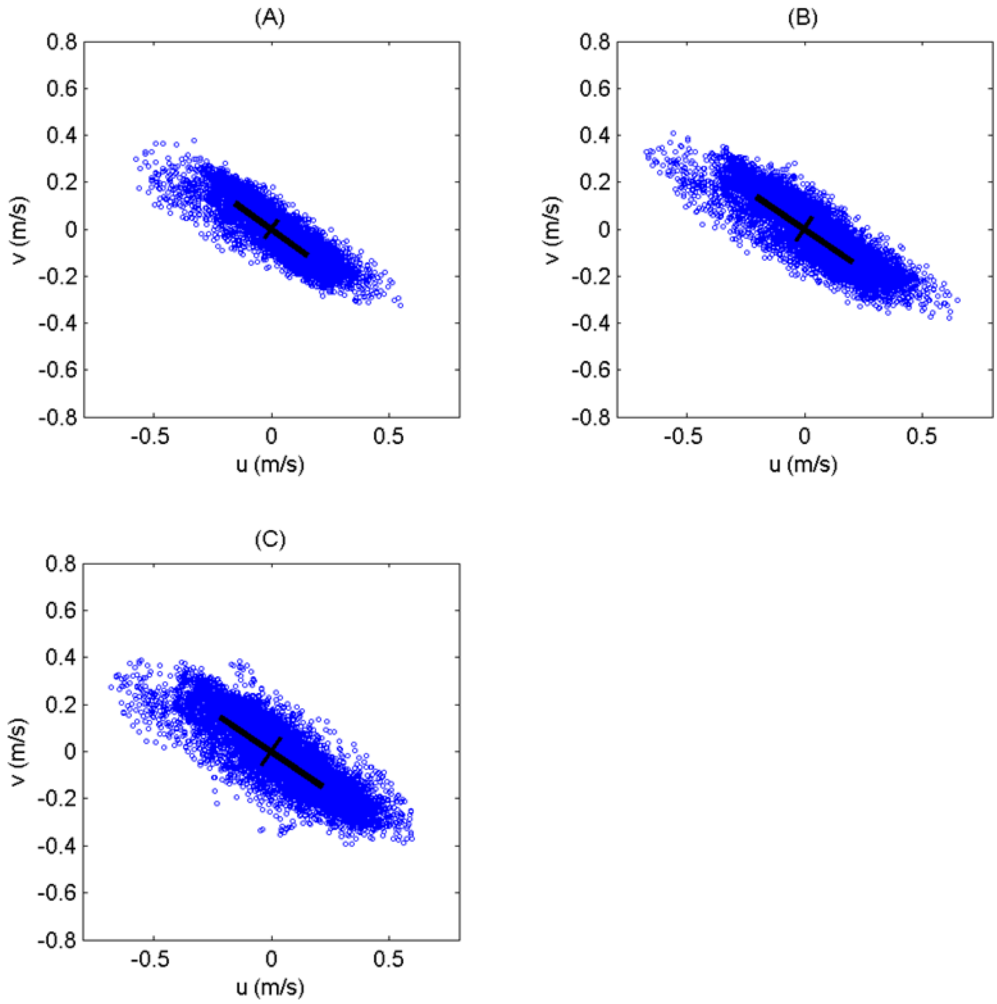

Figure 4-4: Scatter plots of current vector components at three elevations above the bed from deployment S6/D1. Panels: (A) data from 2.1 mab, (B) data from 9.6 mab, and (C) data from 16.6 mab (mab = metres above seabed). Note: the *u* and *v* velocity components relate to the east–west and north–south directions, respectively. The thick line is the major axis and the thin line is the minor axis (both lines span ±1 standard deviation).

Figure 4-5 shows the progressive vector drift for S6/D1 at three elevations above the bed. These plots show the potential drift of water over a period of time (86 days) based on the records from the instrument site. At all three elevations, aside from the occasional circular meanders, there was a consistent drift in the E – ESE direction. Reflecting the increase in current velocities with distance above the bed, drift distances also increased with elevation above the bed. The finer saw-tooth pattern reflects the regular tidal-cycle pattern. The larger deviations from the NW to SE trend are due to weather events.

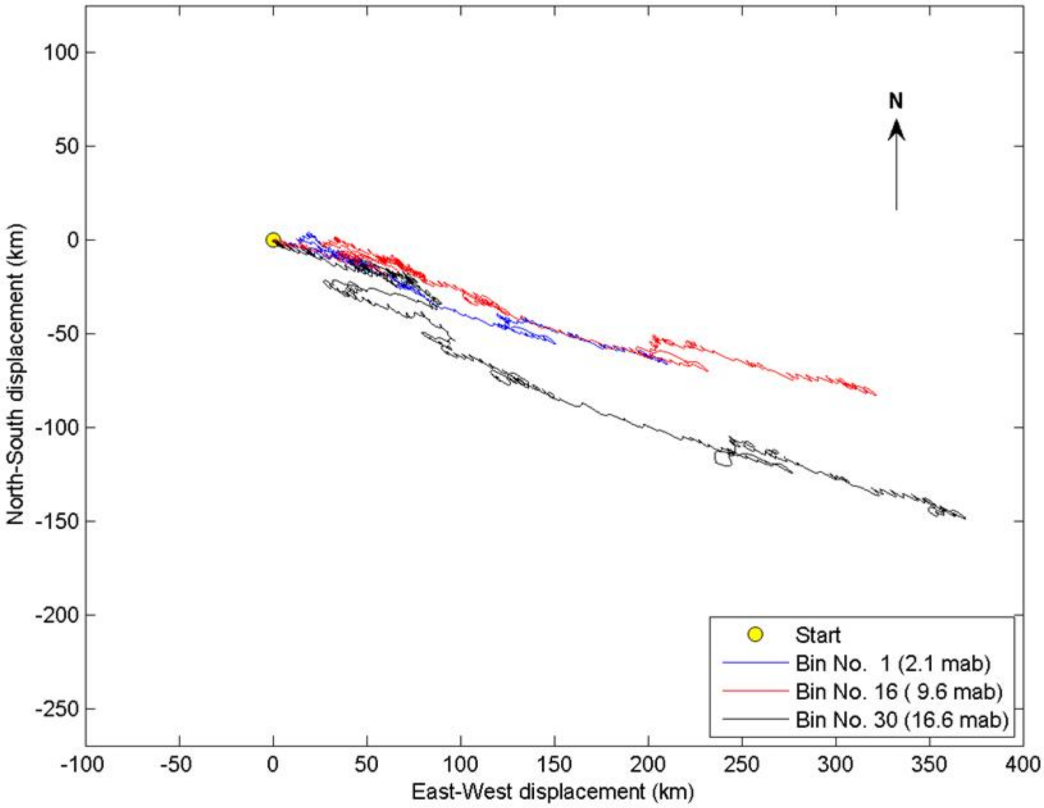

Figure 4-5: Progressive current drift at three elevations above the sea bed for deployment S6/D1 starting 06/09/2011 16:30 (yellow dot) through to 01/12/2011 13:15 (~86 days)..

The net drift speeds and directions are listed in Table 4-1.

Table 4-1: Summary of the overall current drift during deployment S6/D1 (~86 days).

Bin No.	Elevation above bed (m)	Net drift speed (m/s)	Net drift speed (km/day)	Net drift direction (deg. true north)
1	2.1	0.028	2.44	107
16	9.6	0.043	3.70	104
30	16.6	0.052	4.46	112

Tidal currents account for a significant proportion of the measured currents at all sites, with the proportion explained by the tidal constituents ranging from 40% to 78%. The peak ebb or flood current speed of the main twice-daily lunar (M2) tide, which is an average tide, ranged between 0.13 m/s and 0.25 m/s. Somewhat higher and lower tidal speeds occur on spring and neap tides respectively. At all sites the M2 tide was oriented in the SE – NW direction (parallel with the coastline). The presence of such tidal current speeds well offshore in the South Taranaki Bight arises from the alternate flow of water over the extensive, relatively-shallow, shoals off Hawera and Patea.

The modelling and field measurements show that current flows are strongly orientated parallel to the shore and the bathymetry. At most sites during periods of light winds the prevailing or net current drift was towards the SE, which is consistent with the influence of the D'Urville Current, which sweeps past Farewell Spit and turns around in the South Taranaki Bight to head south. However, current drift directions were significantly altered by moderate to strong SE winds which reversed the drift towards the NW. During times of moderate to strong W to NW winds, the prevailing SE drift was considerably enhanced.

4.3 Modelled time-averaged currents

Models setup to model sediment plume behaviour provide a picture of the time-averaged (net) currents and the potential for sediment transport in the region. The modelling system comprised a set of nested domains. The outer domain covered Greater Cook Strait area at 2 km grid resolution and used the HYCOM ocean model. Inner domains covering the South Taranaki Bight at 1 km grid resolution and the smaller area over the Patea Shoals at 500 m grid resolution used the ROMS model which has embedded suspended-sediment and sediment-bed processes driven by currents and waves. There is a full description of model setup and verification in Hadfield (2012 and 2013).

Currents were simulated for a 1000-day period and the statistical quantities and plots presented below are based on the last 730 days of the simulation (21 March 2011 to 20 March 2013).

Figure 4-6 shows that the flow is represented as a stream entering the region from near Cape Farewell at the northern tip of the South Island, then following eastwards along the 50 to 100 m depth band to the South Taranaki coast, skirting south of the Patea Shoals. From there it follows the coast south past Manawatu, Horowhenua and Kapiti, through the Cook Strait Narrows and then northward along the Wairarapa coast.

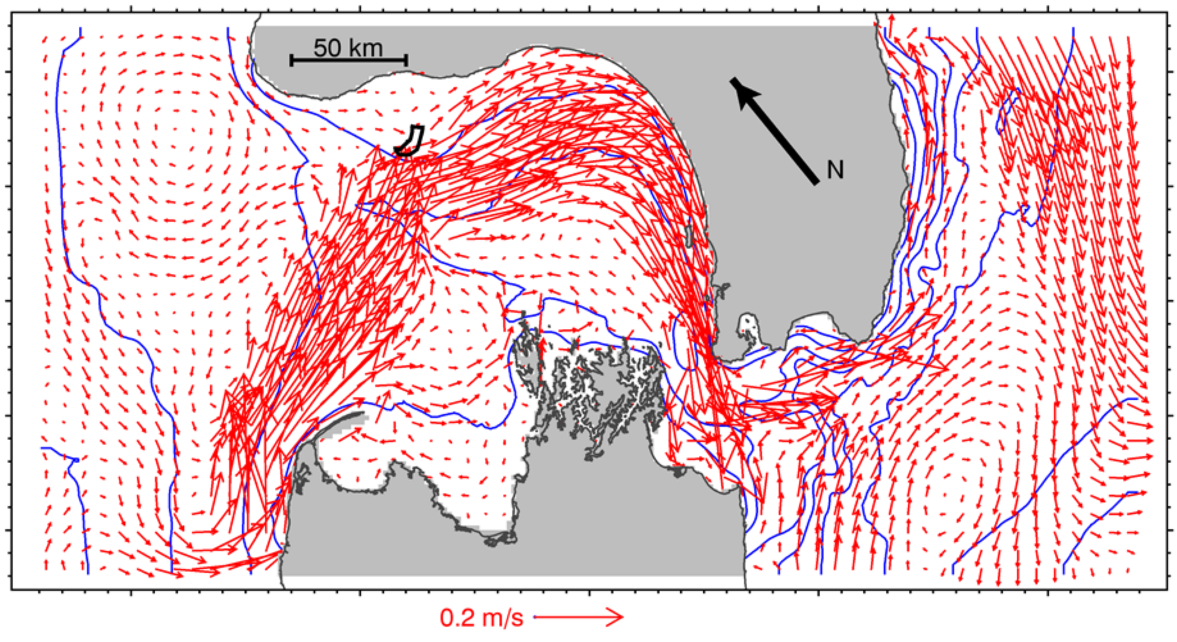

Figure 4-6: Time-averaged, depth-averaged velocity from the Greater Cook Strait model. Velocity vectors are averaged over 730 days and shown at every third grid point. The depth contours are at 50, 100, 250, 500, 1000 and 2000 m. The sand extraction project area is shown as the black polygon. (Source Hadfield 2013).

This current system is called the D'Urville Current. It shows that the project area lies on the northern border of the main flow of the D'Urville Current where the current is much weaker than in the main stream of the D'Urville Current. Off Hawera the mean current flow is weak and is towards the coast but splits to send water North around Cape Egmont and south towards the Patea shoals. The mean velocity of the water in the D'Urville Current stream is of the order of 0.1 – 0.2 m/s.

A finer scale view of water movements is provided by the inner model in Figure 4-7. It shows the depth-averaged velocity vectors averaged over the last 730 days. The circulation patterns are largely driven by the large-scale circulation. The time-averaged current in the extraction area is very weak and of the order of 1 – 2 cm/s and is directed primarily SE. Between the extraction area and the shore the time-averaged current deviates locally from that path as currents are steered about large ridges on the seabed in the relatively shallow waters off Hawera and Patea. Here and landward of the 25 m contour the current is directed weakly (1 cm/s) shoreward, but south of this point it parallels the shore and runs to the SE. Offshore from about Patea and Waiinu the mean current is still weak (2 – 4 cm/s) inside the 40 m depth contour. These weak net currents suggest that net sediment transport will be weak and directed principally to the SE between the extraction site and the shore. The net flow tends to be stronger and of the order of 10 – 20 cm/s in deeper water seawards of the 50 m contour. Its runs to the SE and parallel to the shore and aligns with large ridges on the seabed.

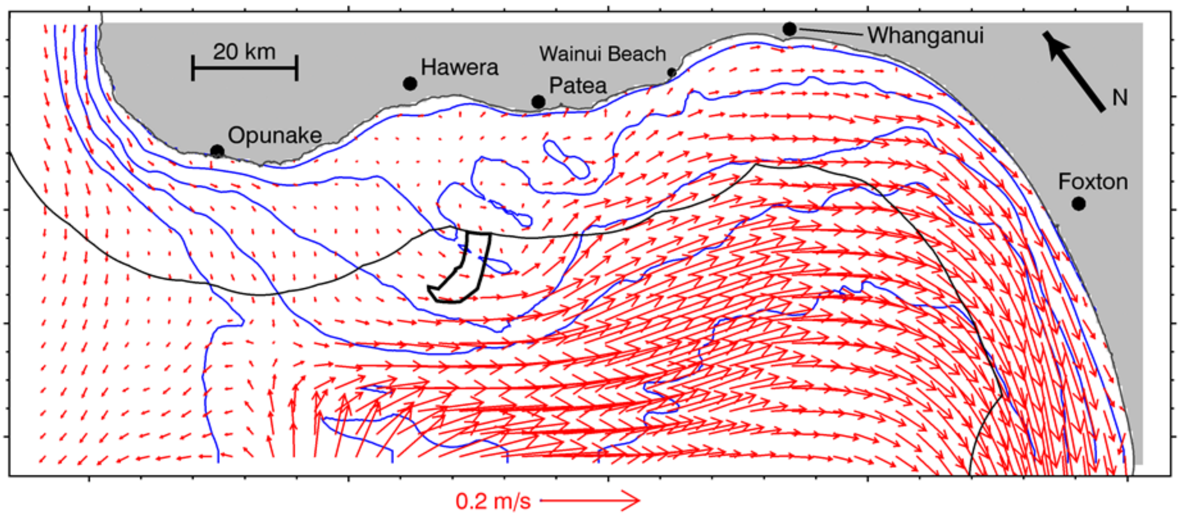

Figure 4-7: Time-averaged near-bottom mean velocity from the inner model. Velocity vectors are averaged over 730 days and shown at every third grid point. The depth contours are at 10, 25, 50, 75, 100 m. The sand extraction project area is shown as the black polygon and the 22.2 km territorial limit with the thin black line. (Source Hadfield 2013).

4.4 Sediment transport potential at the extraction site

As part of studies of sediment plume generation and advection the fate of de-ored sand returned to the seabed was investigated by using the models described above (Hadfield 2013). Some of the results from this modelling are described here to evaluate the potential for seabed sands to be transported away from the extraction area by waves and currents and therefore the connection between seabed sands at the site and sand on the shore.

The fate of de ored sand at the extraction site was investigated using the model by replacing a 3 x 2 km rectangular patch of seabed sand in the extraction area with sand representing one years' worth of ironsand extraction. The patch was represented by 4 classes of sediment, namely: coarse sand (500 – 1000 µm, 14.3%), medium-fine sand (125 – 500 µm, 80.7%), very fine sand (90 – 125 µm, 4.2%) and very coarse silt/very fine sand (38 – 90 µm, 0.8%). By way of model verification a comparison of the modelled near-bottom sand concentrations was made with Acoustic Back Scatter (ABS) data from instrument sites on the Patea shoals. This showed the formulation of resuspension in the model overestimated the resuspension in some places and underestimated it in others, although provided general agreement overall (Hadfield 2013, section 4.3). The model simulation (of bedload and suspended load) was run for 3000 days of currents and waves. The patch is put in place at 2200 days and the simulation continued for another 800 days. The plots produced by the model show these seabed thickness at the end of the simulation and the time-averaged SSC at the seabed over the last 730 days (2-years) of the simulation.

Time-lapse imagery from the model simulations shows that sand in the lower 1 m of the water column at the extraction site gets lifted into suspension reasonably often by the combined action of waves and currents, but doesn't travel far before it is deposited again. After 730 days, patch material is found to be thinly spread on the surrounding seabed at thicknesses of 0.2 – 0.3 mm up to 5 km from the patch boundary and > 0.1 mm up to 7 km from the patch boundary (Figure 4-8). The maximum thickness (immediately outside the patch boundary) is 21 mm. The patch material has been transported in all directions away from the patch but with a strong bias to the southeast and in the direction of the prevailing current (cf. Figure 4-7).

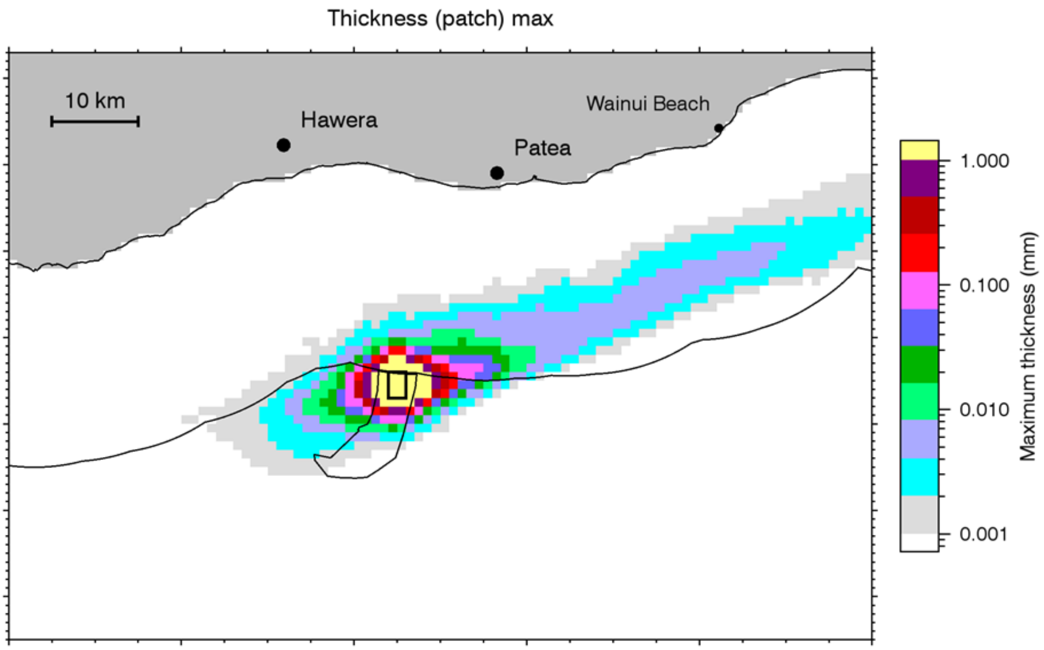

Figure 4-8: Simulated net accumulation of sediment around the seabed patch in the extraction area. Figure shows result at end of model simulation of 700 days of wave and current forcings. The patch was represented by 4 classes of sediment. The yellow area bounded by a black rectangle is the patch sediment. (Source Hadfield 2013).

A closer examination of the distribution of the net sediment accumulation by grain size on the seabed around the patch reveals that the different size fractions are being transported away from the patch in very different ways (Figure 4-9, Figure 4-10, Figure 4-11, Figure 4-12). Figure 4-12 shows that the long tail of sediment distribution to the southeast is made up of the fine component (very coarse silt/very fine sand, 38 – 90 µm). The coarser fractions, and notably the coarse sand (500 – 1000 µm and medium-fine sand (125 – 500 µm) which could potentially contribute to beach sediment, are deposited in small amounts and relatively close to the patch (Figure 4-9 and Figure 4-10).

In summary, the patterns of deposition indicate that sediment of particle size similar to that on the beaches is not distributed far from the extraction site, and that the transport of sand to the shore from the extraction site (or a deficit therein) will take a lot more than 2 years. That is to say the model results suggest there is no evidence for a significant connection between seabed sand at the extraction site and sand at the shore.

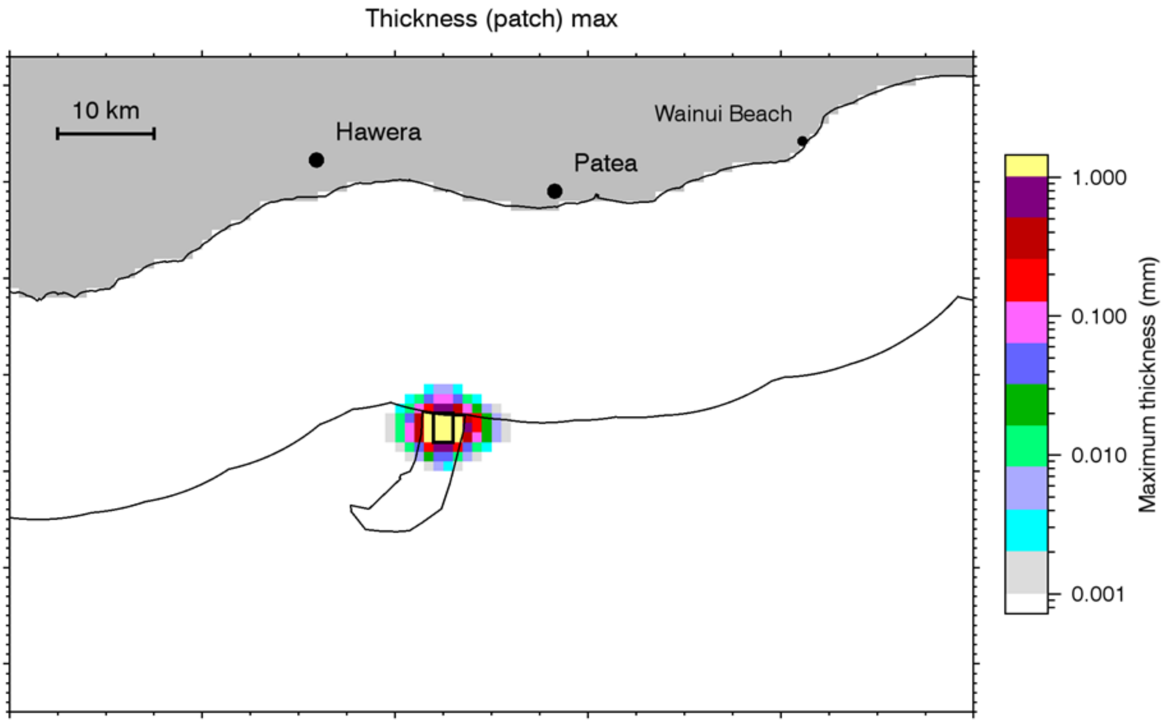

Figure 4-9: Simulated net accumulation of coarse sand (500 – 1000 µm) around the seabed patch in the extraction area.

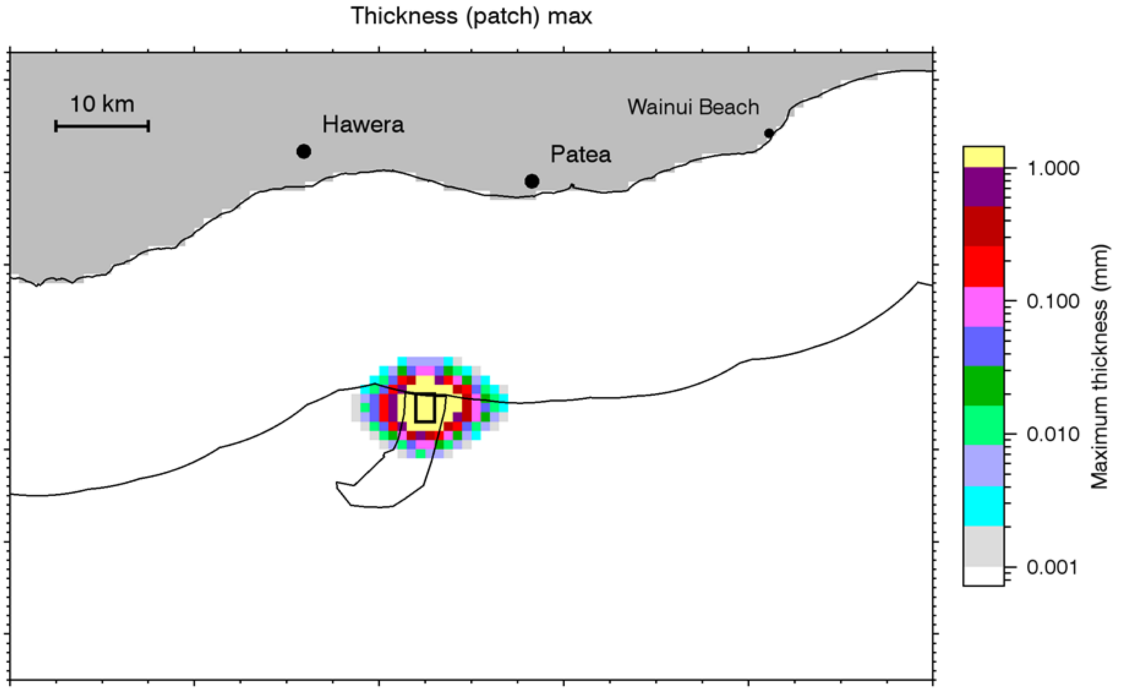

Figure 4-10: Simulated net accumulation of medium-fine sand (125 – 500 µm) around the seabed patch in the extraction area.

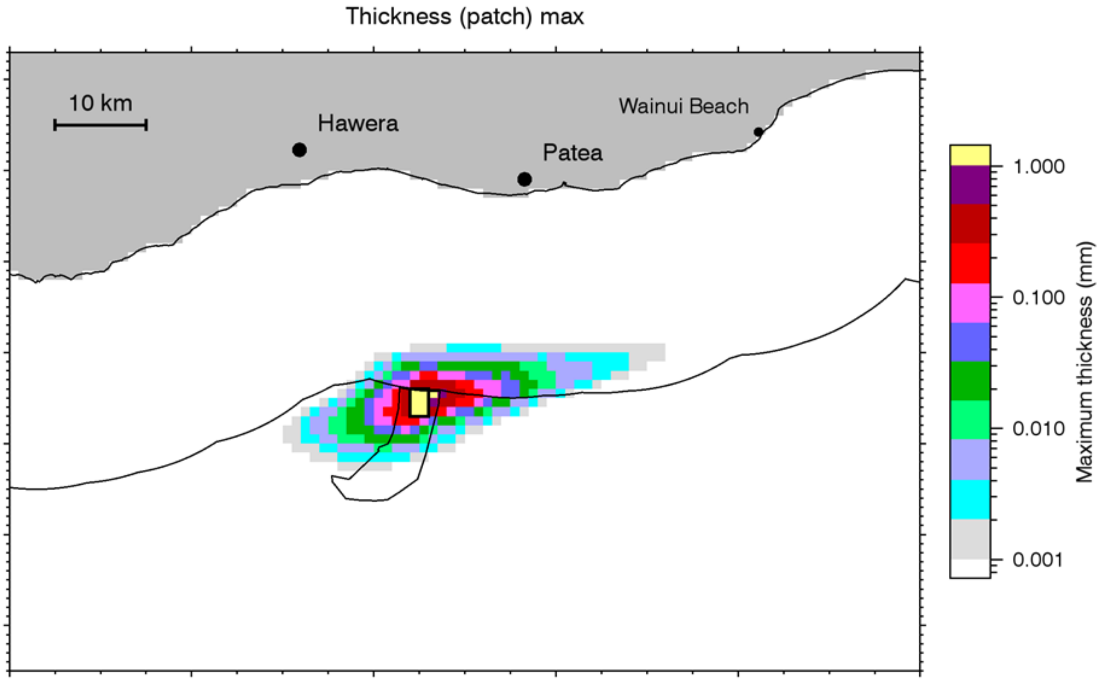

Figure 4-11: Simulated net accumulation of very fine sand (90 – 125 µm) around the seabed patch in the extraction area.

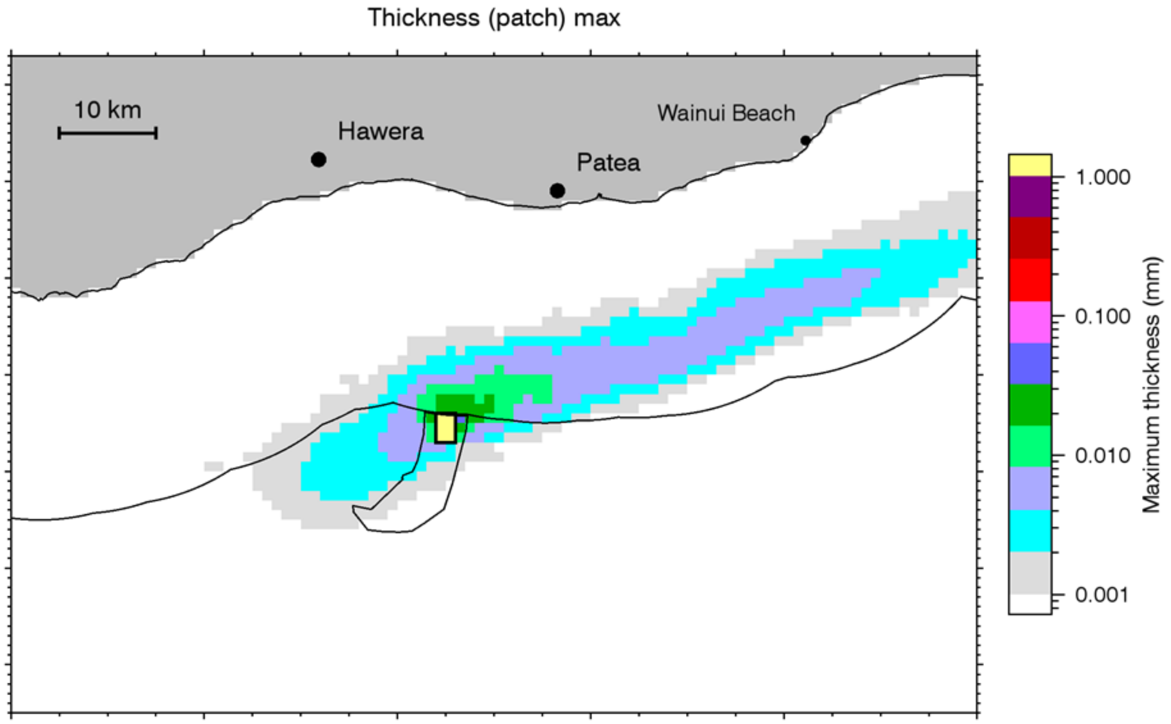

Figure 4-12: Simulated net accumulation of very coarse silt/very fine sand (38 – 90 µm) around the seabed patch in the extraction area.

5 Wave climate and effects on extraction on waves

Waves are a major driver of sediment transport, particularly in the nearshore and surfzone. Most wave energy in the South Taranaki Bight comes from large southwest swells from the Southern Ocean and locally generated wind waves from the Tasman Sea that vary in size and direction with season. On the shelf and in the extraction area seabed stirring by waves entrains seabed sediments that can then be advected by currents. In the nearshore and surf zone sand transport along and across the shore is driven primarily by the waves arriving at an angle to the shore. In this section we describe wave conditions in the South Taranaki Bight and how sand extraction might affect waves as they pass through the extraction site and travel toward the shore.

5.1 Wave climate in the South Taranaki Bight

A numerical model, verified against records from wave buoys and satellite altimeters, provided a 20-year hindcast of wave conditions for the South Taranaki Bight (MacDiarmid et al. 2010). The model simulations provide records of wave statistics along the 50 m isobath at 43 output locations (Figure 5-1), including significant wave height, mean and peak wave period, mean and peak wave direction, wave energy flux, as well as the associated wind speed and direction.

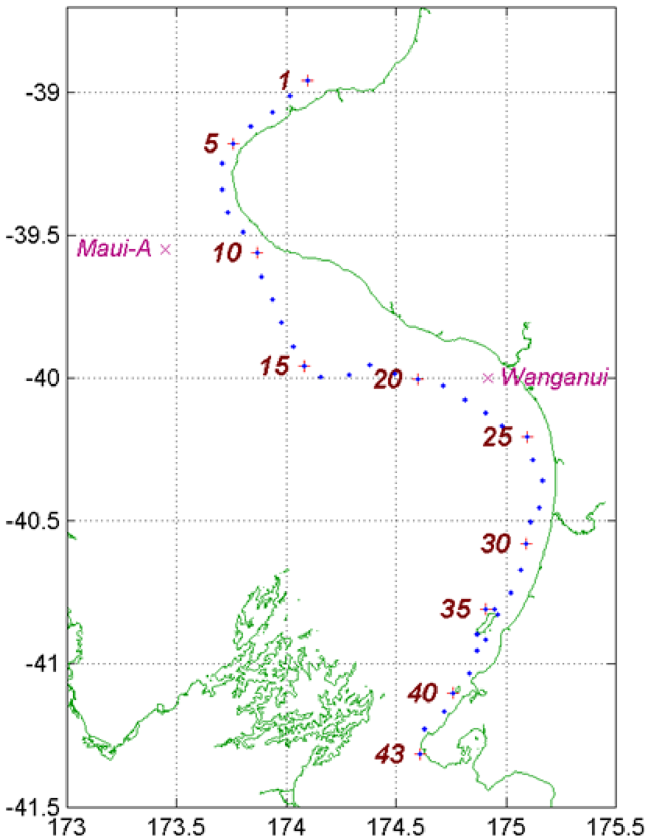

Figure 5-1: Wave hindcast output locations on the 50 m isobath, with every 5th location numbered. The locations of wave buoys (Maui-A, Wanganui) used for model verification are also marked. Site 10 lies off Opunaki. Sites 15 and 20 lie off Patea and Waitotara respectively and are just seaward of the project area. Source (MacDiarmid et al. 2010).

The 20-year average significant wave height for all output locations is plotted in Figure 5-2. This shows that the largest wave heights are found off the western end of the Taranaki Peninsula, decreasing further south with increasing shelter from prevailing SW swell.

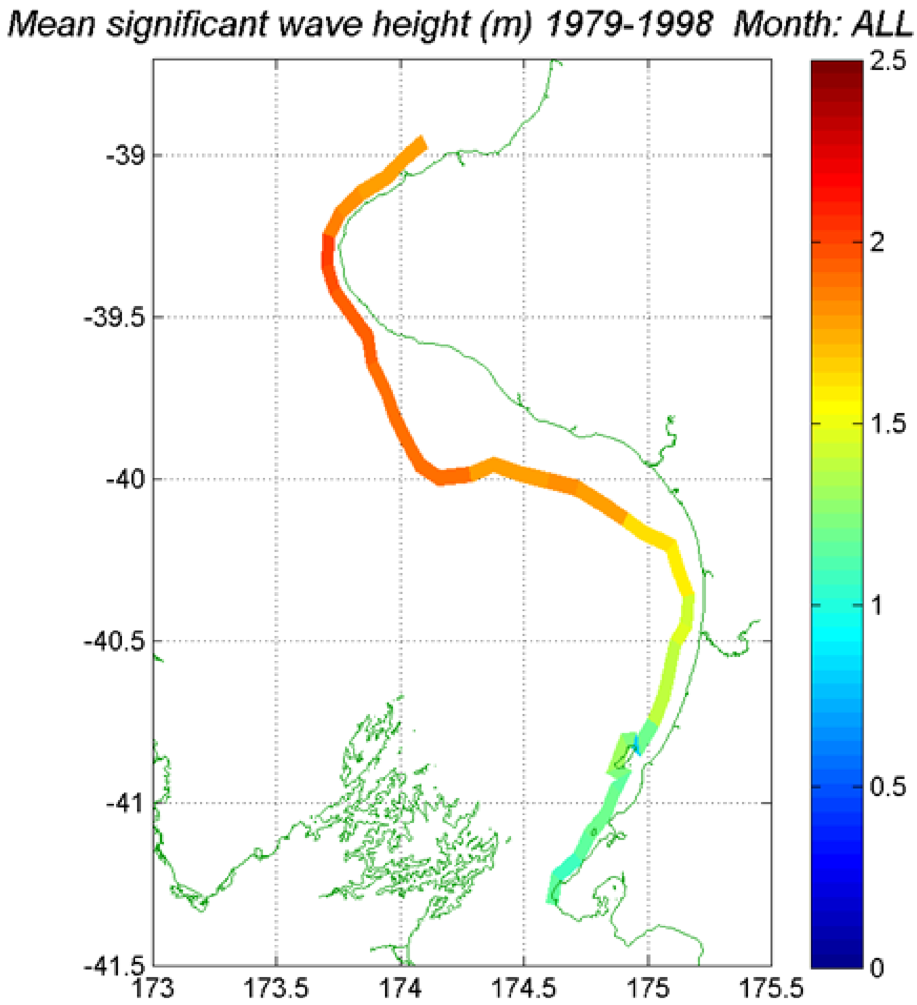

Figure 5-2: Spatial distribution along the 50 m isobath of mean significant wave height, averaged over the full 20-year hindcast record. Source MacDiarmid et al. 2010.

This pattern is also seen in the corresponding average of wave energy flux (Figure 5-3), which is a vector quantity reflecting the magnitude and direction of energy transfer by the waves. This shows relatively strong energy transfer, principally from the WSW, at the northern end of the South Taranaki Bight, while further south, the more southerly energy components become blocked. Note that the magnitude of the vector mean energy flux will always be somewhat less than the mean of the magnitude of the energy flux vector. The orientation of energy flux relative to the coast is also significant, as wave energy reaching the coast at an oblique angle (i.e., not perpendicular to the coast) will drive longshore sediment transport.

Inshore of the 50 m isobath the incident wave direction is affected by quite complex bathymetry. In the nearshore, wave and breaking angle (relative to the shore) are further affected by shore platforms and rock reefs. These effects, and the resulting detailed patterns of longshore sediment transport, are addressed by nearshore wave modelling as described later in this report.

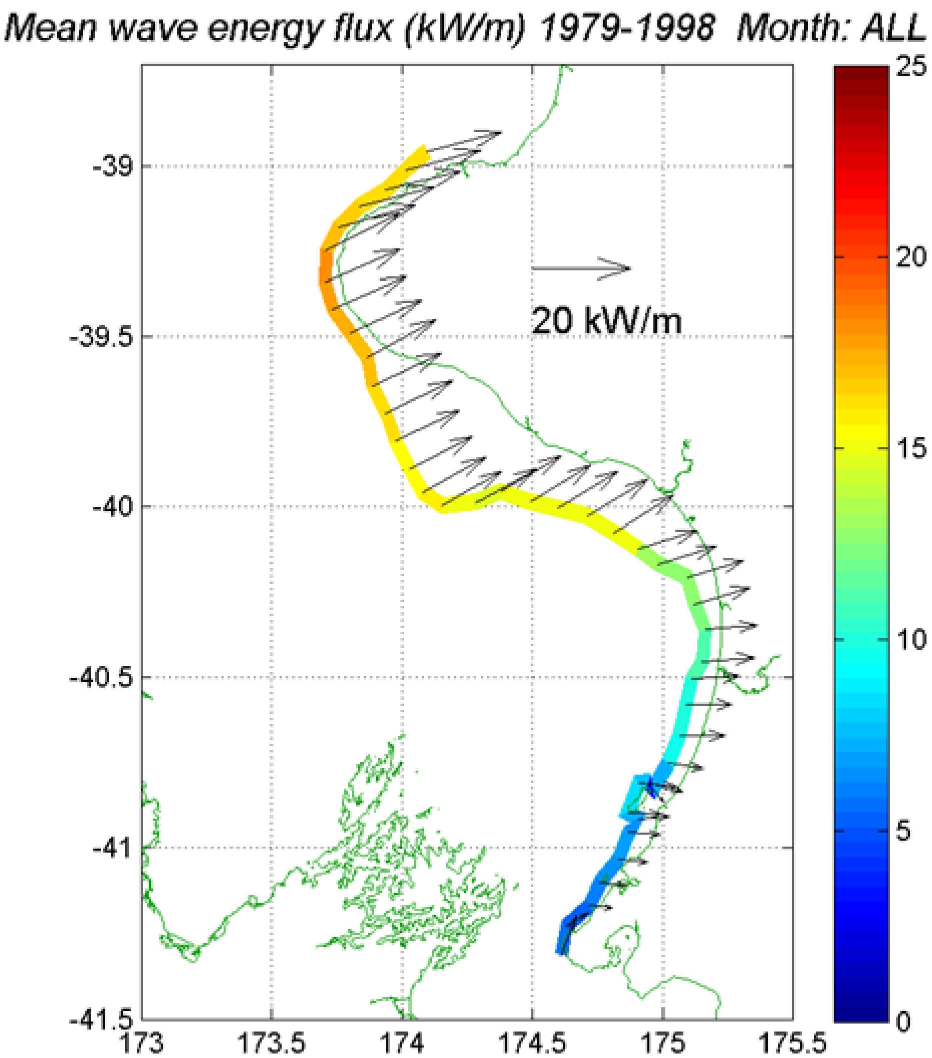

Figure 5-3: Spatial distribution along the 50 m isobath of mean wave energy flux, averaged over the full 20-year hindcast record. The colour scale shows the mean of the magnitude of the energy flux, while the arrows show the vector averaged flux.

The model predictions show a seasonal cycle with mean wave heights reaching a maximum in late winter and a minimum in late summer. At site 15 (off Patea), for example, the 20-year mean significant wave height is 1.9 m, but with monthly means varying between 1.5 m in February and 2.2 m in August. In comparison the wave period varies little, the 20-year mean of the peak wave period is 11.2 sec, but with monthly means varying between 10.3 sec in January and 11.9 sec in August. At site 20 (off Waitotara), the 20-year mean significant wave height is 1.8 m, with monthly means varying between 1.4 m in February and 2.1 m in August. Here as well the wave period shows little seasonal variation: the 20-year mean of the peak wave period is 11.4 sec, but with monthly means varying between 10.4 sec in January and 12.0 sec in August.

Occurrence distributions for the various wave statistics at sites 15 (off Patea) and 20 (off Waitotara) which lie close outside the project area, are plotted in Figure 5-4 and Figure 5-5 respectively. These are accumulated over the full 20-year record. Single variable occurrence distributions (as percentage of time that the quantities are in specified ranges) are shown for significant wave height, peak period and mean period. We also show a wave rose, representing the joint occurrence of significant wave height and mean wave direction, the exceedance distribution for significant wave height, and a plot of “downtime”, i.e., the percentage of time in each calendar month that specified thresholds of significant wave height are exceeded.

We see in Figure 5-5 for example, that at site 15 (off Patea), the most frequently occurring significant wave height is approximately 1.5 m (somewhat below the mean value of 1.9 m) (Figure a), but that the distribution has quite a long tail, up to a maximum of 8.0 m. Peak wave period (usually reflecting the swell component of the spectrum is typically around 12 seconds (Figure b), while the second moment mean period (more influenced by short wind sea) is spread through the range 5 – 10 seconds (Figure c), with values around 7 seconds predominating. The wave rose (Figure d) shows the predominance of waves from the southwest through westerly sectors. The “downtime” plot shows a strong seasonality in the likelihood of energetic wave conditions: for example, significant wave heights over 3 m occur 8% of the time on a year-round basis (shown by the horizontal red line), but this varies from less than 3% in the summer months to over 15% in winter.

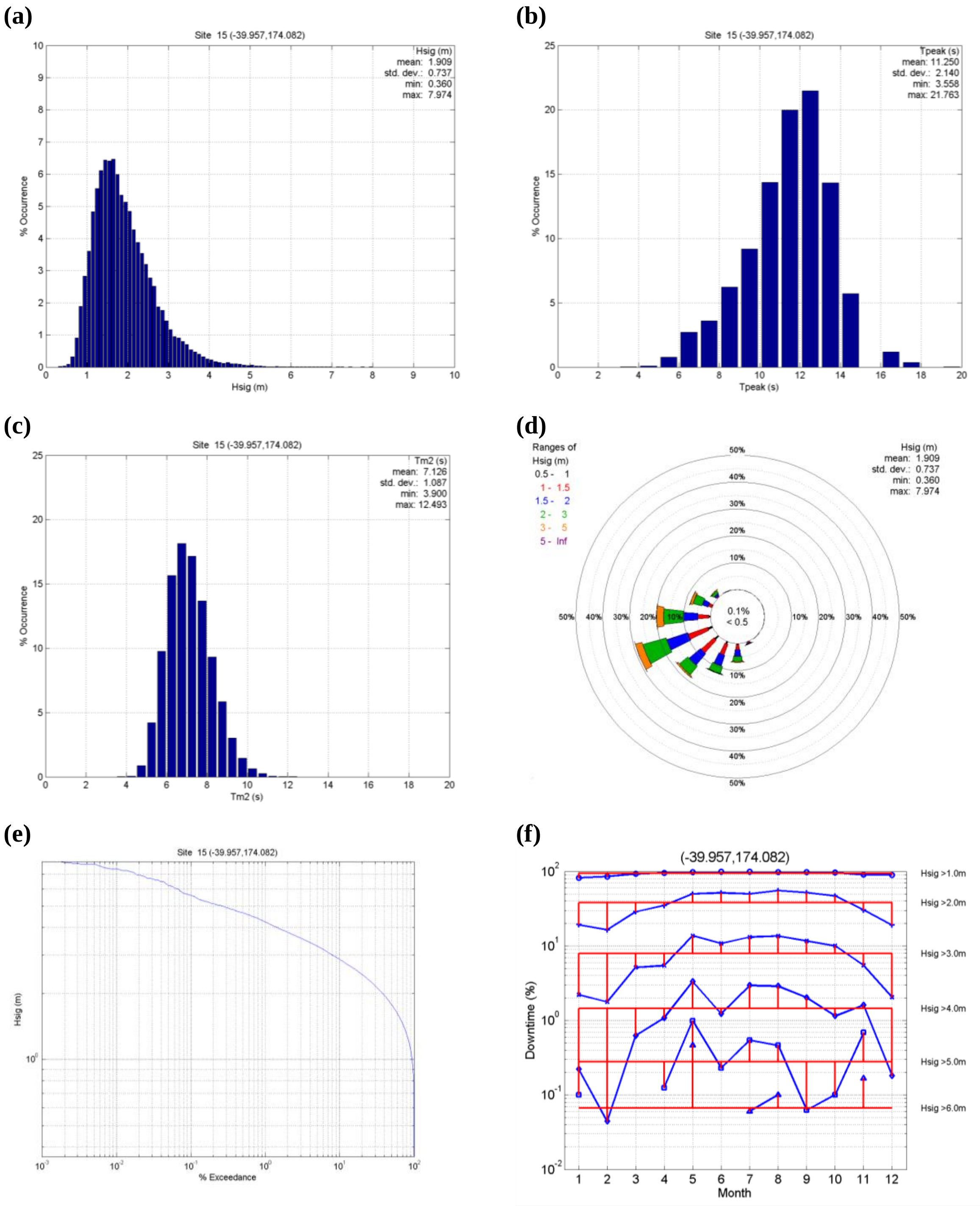

Figure 5-4: Occurrence statistics for site 15 at (39.957°S, 174.082°E) from the full 1979-1998 hindcast. The first three plots show percentage occurrence for: (a) significant wave height, (b) peak wave period, and (c) mean wave period (second moment). Also shown are: (d) the wave rose, (e) the

wave height exceedance distribution and (f) “downtime”, i.e., the percentage of time that given

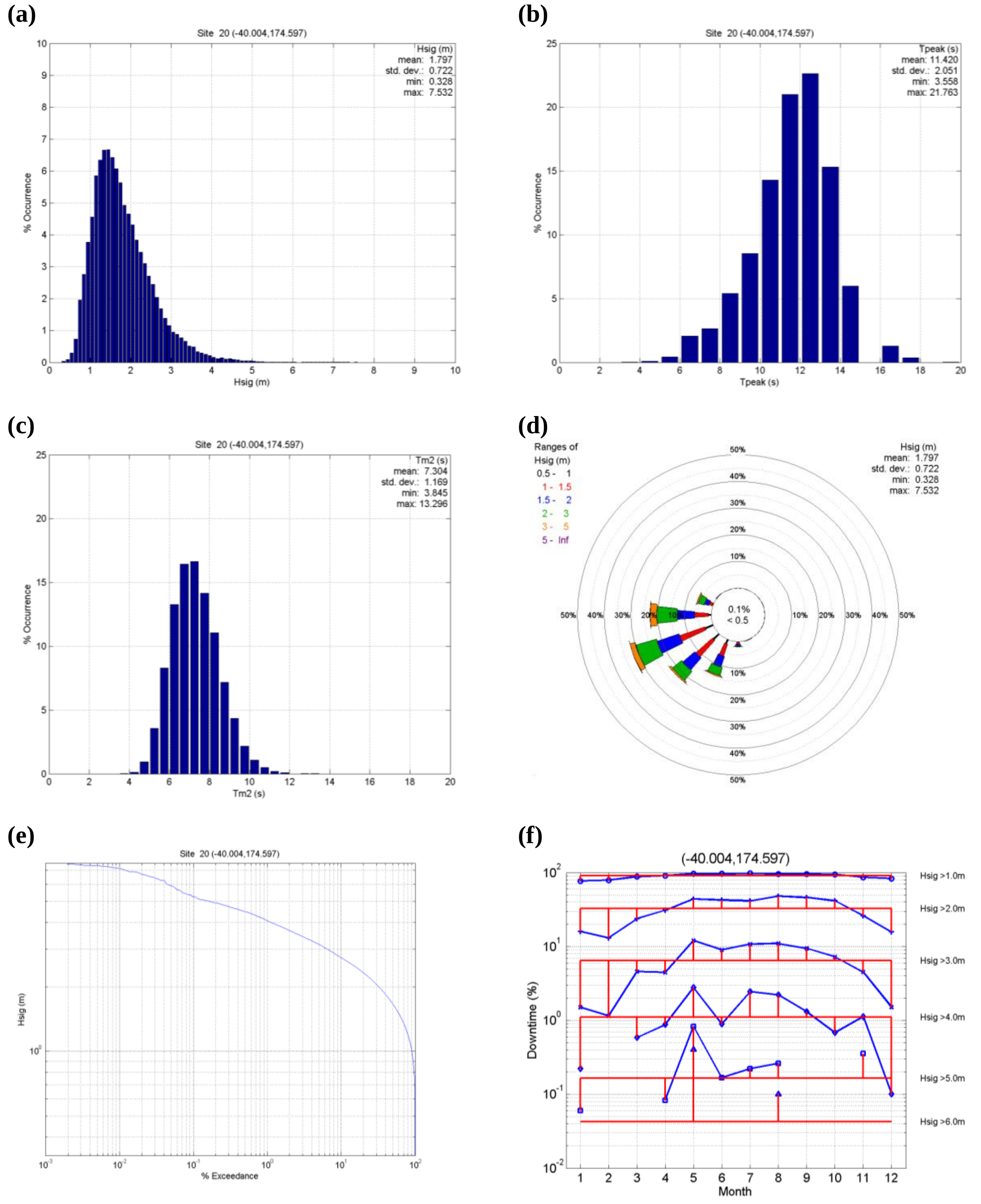

significant wave height thresholds are exceeded for each month.

Figure 5-5: Occurrence statistics for site 20 at (40.004°S, 174.597°E) from the full 1979-1998 hindcast. The first three plots show percentage occurrence for: (a) significant wave height, (b) peak wave period, and (c) mean wave period (second moment). Also shown are: (d) the wave rose, (e) the wave height exceedance distribution and (f) “downtime” , i.e., the percentage of time that given significant wave height thresholds are exceeded for each month.

5.2 Effect of climate change on wave conditions

In the next 50 years climate change is predicted to cause a rise in sea level (by 25 cm) and changes to the wave climate. In this study, the wave modelling undertaken to predict the effect of modifications in seabed bathymetry (pits and mounds) due to sand extraction has been carried out using present day wave climate statistics. If the wave climate was to change significantly with future climate change then those predictions would be less accurate. The time frame under consideration is at least 20 years (the possible duration of a mining permit) or longer if the pits and mounds formed on the seabed were to remain unaltered by natural processes of infilling and scour. To address this issue we use information from a recent study by NIWA which produces ‘futurecasts’ of the effects of climate change on sea conditions and wave climate.

5.2.1 Methodology

The effect of projected climate change over the next 100 years on wave conditions in New Zealand waters has been investigated by NIWA in the “Waves and Storm surge Projections” research programme. This used numerical models to carry out a set of long-term simulations of both waves and storm surge in a nationally consistent manner.

Firstly “hindcasts” of historical conditions were run, which were verified against available measurements from wave buoys and sea level recorders. These used inputs of surface winds and air pressure from the ERA-40 Reanalysis dataset (Uppala et al. 2005) from the European Centre for Medium Range Weather Forecasts (ECMWF). This dataset covers the period October 1957 - September 2002 on a global domain at 1.125° x 1.125° resolution in longitude and latitude (approximately 125 km resolution at the equator).

To provide wave hindcasts, the Wavewatch III™ model (Tolman 1991, Tolman 2007) was first run on a global grid ('era40gw_125') matching the input ERA40 grid except for being reduced to the latitude range -81° to +81°. To provide more detailed outputs at a New Zealand regional scale, two different nested hindcasts were then run. The first of these ('waspnzw_10'), run on a nested subdomain covering waters around New Zealand at 0.125° x 0.09375° resolution (approximately 10 km), used the same (low resolution) wind inputs as the global wave model, so the finer resolution served only to interpolate wave conditions into nearshore locations. A second regional hindcast ('rcm_9_era') was run for the years 1970 – 2000, nested in the same global wave simulation. For this, ERA40 winds had been downscaled by a Regional Climate Model (RCM) operating on a rotated pole latitude/longitude grid at 0.27° resolution. These wind fields were interpolated to a regular latitude/longitude regional grid ('rcm_9') at approximately 9 km resolution for wave model simulations. No air-sea temperature difference fields were available, so no stability corrections were made to the wind input term for this simulation.

Both of these hindcasts simulate historic wave conditions, and have been checked against measured records available from wave buoys, both in New Zealand waters and further afield.

The next step was to run "futurecasts" to project conditions 100 years into the future, simulating the years 2070-2100. For this, inputs were taken from climate models, both on global and regional scales. Two emissions scenarios ('A2' and 'B2') were chosen from the Special Report on Emissions Scenarios used in the 4th Assessment Report (AR4) of the Intergovernmental Panel on Climate Change (IPCC) (IPCC AR4 WG1, 2007). The A2 scenario represents a more divided world with population continuing to increase and a focus on regional economic development. This scenario is on the high side for continuing increase in CO_2 emissions. The B2 scenario is also a divided world but with a stronger focus on environmental rather than economic issues. While CO_2 emissions still increase under the B2 scenario they do so at a much slower rate than in the A2 scenario and thus represent one of the lower scenarios in the AR4 SRES suite. The futurecast scenarios had all been run on a Global Climate Model (GCM) and then dynamically down-scaled using a New Zealand Regional Climate Model (RCM). Four future scenarios were run in total, three of which were variants of the A2 scenario (A21, A22 and A23) and the fourth was a B2 scenario. In all these scenarios the variability of the sea surface temperatures (SST) is exactly the same over the thirty year period, however, the SST trend and the atmospheric CO_2 concentration were determined according to the scenario. The three A2 scenarios differed only due to their initial conditions.

To provide a benchmark for the futurecasts, corresponding GCM and RCM simulations of the period 1970 – 2000 were run, using the same model settings apart from those directly related to the various CO_2 scenarios. Note in particular that the benchmark simulation is not constrained to follow actual weather events, unlike the hindcasts based on ERA-40 data.

The Wavewatch model was again used to simulate wave conditions under these inputs, providing outputs of wave parameters (including significant wave height, peak and mean wave period, peak and mean wave direction), at hourly intervals over the thirty year period 2070-2100 from scenarios A21, A22, A23 and B2, for comparison with corresponding results from the baseline 1970-2000 benchmark simulation.

5.2.2 The results

For this study, outputs at a location (174.19°E, 39.96°S) off Patea in the South Taranaki Bight were selected. As noted above, the actual simulated sequences of weather events are not of significance – rather we focus on comparing statistical properties of the outputs.

In Figure 5-6 occurrence distributions for significant wave height are compared. In the benchmark climate, the occurrence distribution peaks close to 1 m, with an extended tail out to 7 – 8 m. Under all the climate change scenarios there is a small reduction in occurrence of wave heights below that 1 m peak value, balanced by a small increase in events with heights above 2 m.

For mean wave direction (Figure 5-7), the benchmark climate shows a predominance of waves from the west and WSW, peaking at around 260°, and a secondary peak near 160°. All of the climate change scenarios produce a modest strengthening of the main peak, i.e., an increased occurrence of waves from the west and WSW, at the expense of a decreased occurrence of waves from directions in the west through NW range.

The projected changes in wave climate are not seasonally uniform, as we see in Figure 5-8, which shows percentile values of significant wave height on a monthly basis. The existing wave climate shows the most energetic wave conditions occurring in either September or October (for median values), or in May (for the higher percentiles), with the lowest wave heights occurring in February and March. The climate change scenarios tend to increase that seasonal variability, while shifting the annual minima to December and January.

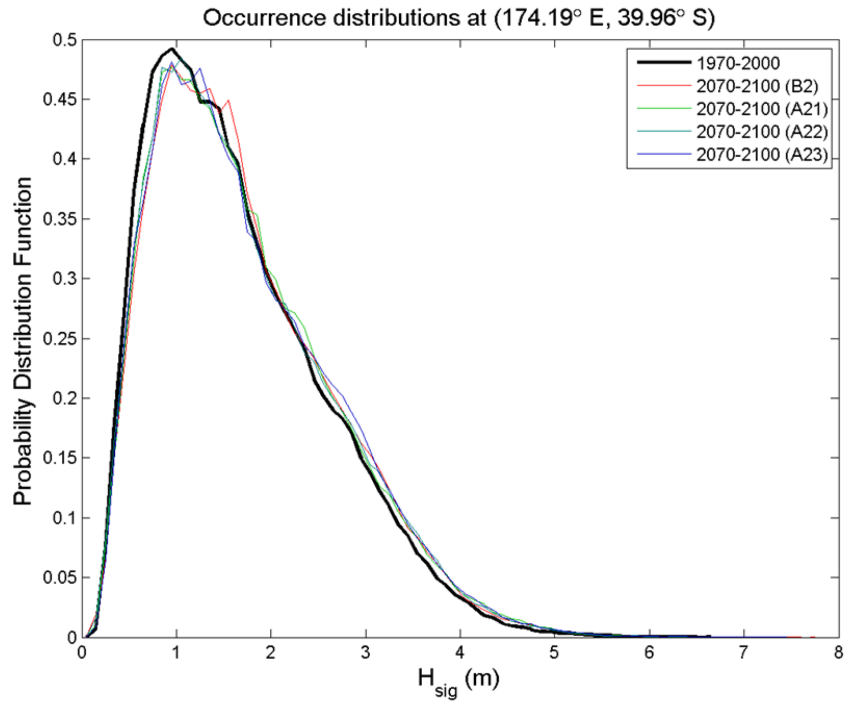

Figure 5-6: Probability distribution functions for significant wave height at (174.19°E, 39.96°S), in the benchmark 1970-2000 simulation (solid black line) and in the four futurecasts (coloured lines).

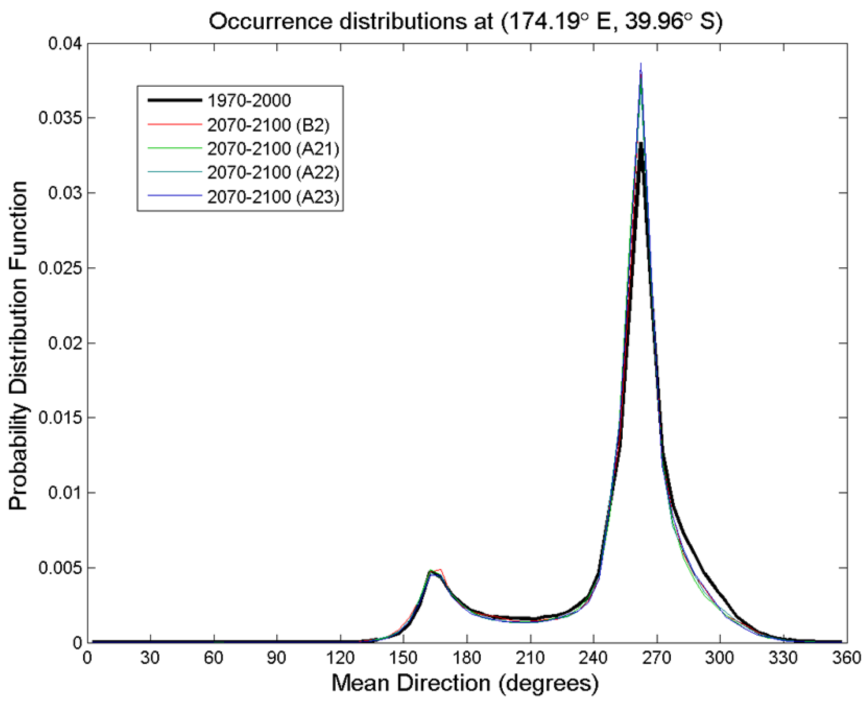

Figure 5-7: Probability distribution functions for mean wave direction at (174.19°E, 39.96°S), in the benchmark 1970-2000 simulation (solid black line) and in the four futurecasts (coloured lines).

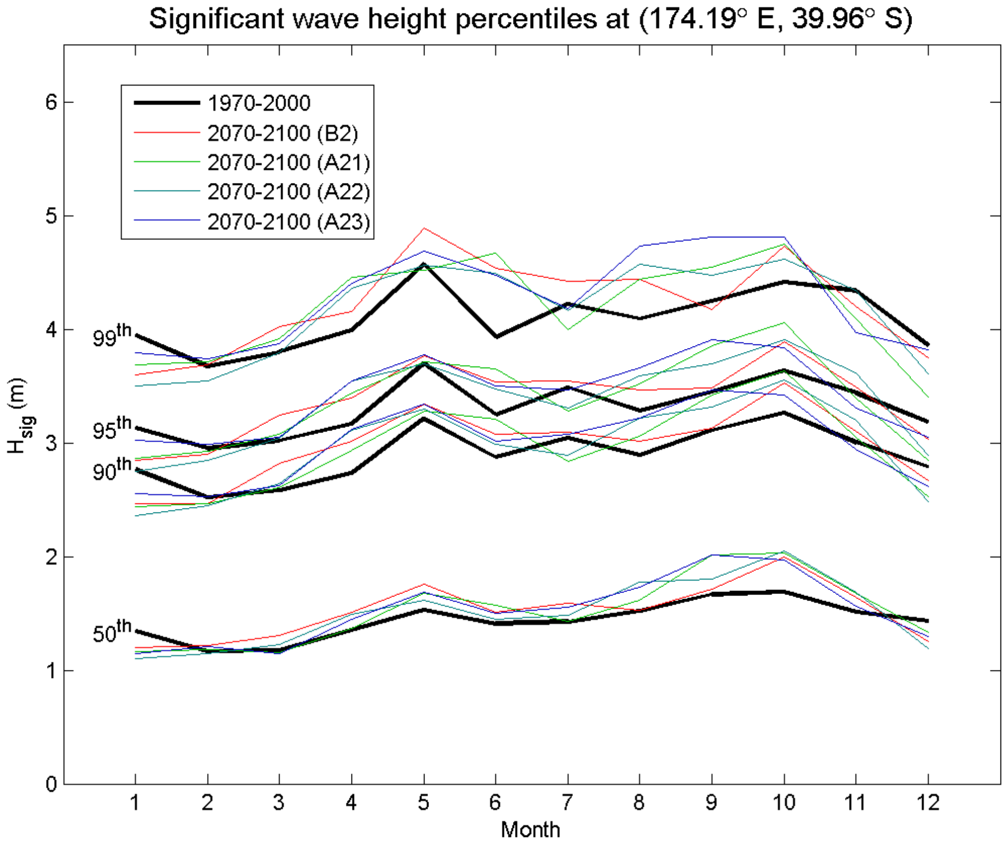

Figure 5-8: Monthly percentile values for significant wave height at (174.19°E, 39.96°S), in the benchmark 1970-2000 simulation (solid black lines) and in the four futurecasts (coloured lines). The lowest set of lines shows the monthly median (50^{th} percentile) values, with 90^{th}, 95^{th} and 99^{th} percentiles plotted in succession above that.

In summary, futurecasts, demonstrate that the changes in wave climate due to climate change are very small and will not alter the natural wave processes significantly in the next 20 years. Therefore, these changes will not alter our predictions of the impacts of extraction on coastal stability presented in following sections of this report.

5.3 Effects of sand extraction operations on wave conditions

The proposed sand extraction operations will result in pits, elongate depressions (lanes) and mounds in the seabed that can potentially affect waves by refraction (bending the wave path) and diffraction (lateral dispersion of wave energy) and locally by shoaling (changing the wave height) them as they pass over the modified seabed. Such changes in the wave field introduced at the extraction site may be propagated shoreward, leading to potential changes in wave conditions nearshore with consequent changes in shoreline processes (longshore transport and erosion and accretion). The magnitude of any such changes will depend on a number of factors, including the natural wave climate of the region, the water depth at the extraction site, the configuration of the modified seabed and the distance offshore. Note that, as reported earlier, climate change will have little effect on the wave climate so that the predictions made here will not change with climate change.

5.3.1 Approach and selection of seabed modifications (pits and mounds) to model

Numerical modelling was undertaken to quantify the location and magnitude of such potential impacts of proposed sand extraction operations on coastal wave and conditions and associated sediment transport. This was undertaken using the SWAN nearshore wave model and set of rectangular nested model grids (Figure 5-9) described in Gorman (2012 and 2013), calibrated against field measurements reported in MacDonald et al. (2012).

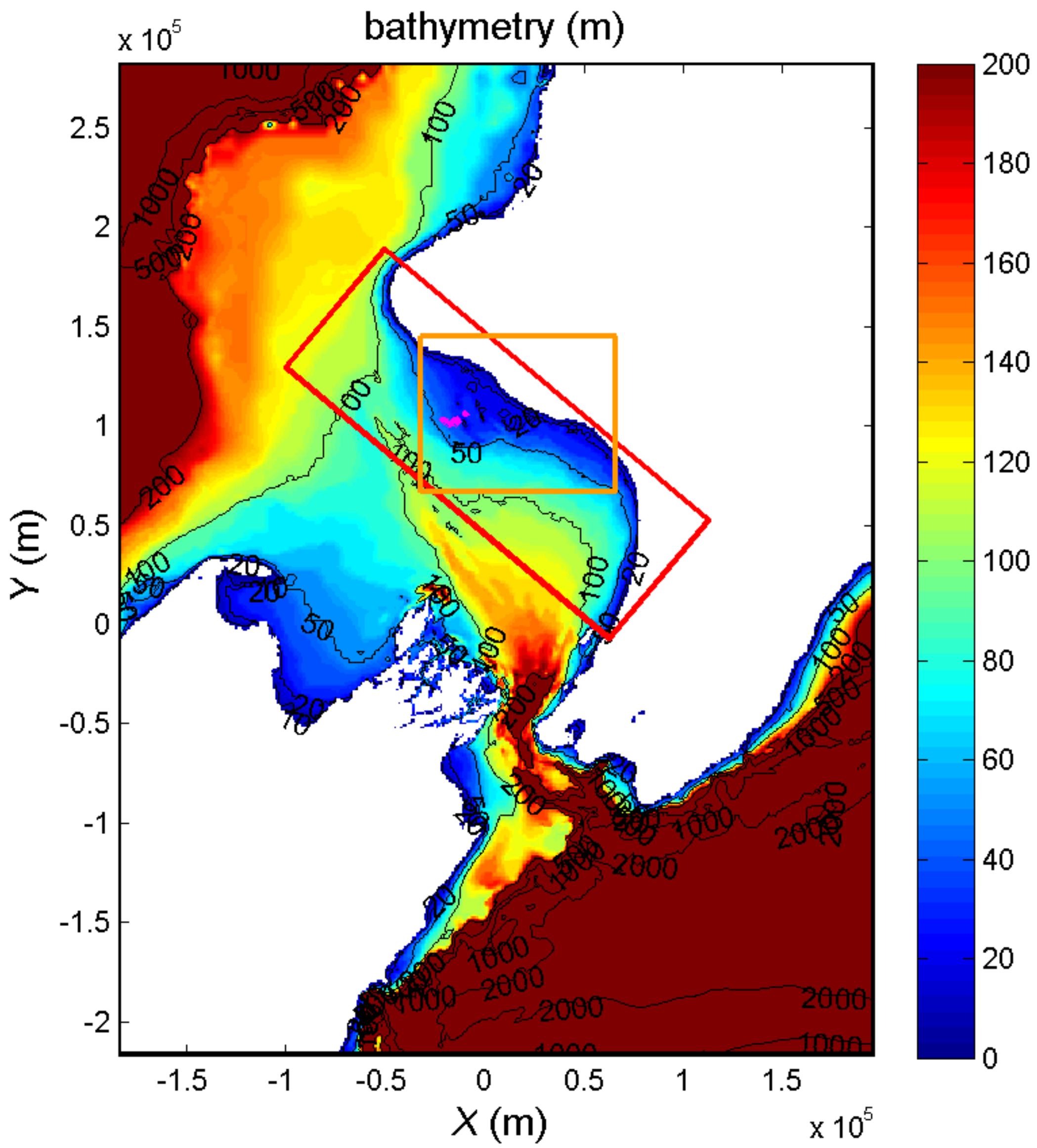

Figure 5-9: Map showing bathymetry in the Greater Cook Strait region, with the extent of grid domains for SWAN simulations. The red box marks the 500 m resolution grid used to provide

wave inputs for sediment modelling, while the orange box shows the 100 m resolution grid used for wave sensitivity studies. The extraction areas are outlined in magenta.

The modelling results were produced as a result of specified wind conditions acting over a region with specified bathymetry (spatially-varying water depth), also taking into account swell entering from outside the study region. In particular, the model is first used to simulate regional wave conditions with the existing (naturally occurring/unmodified) bathymetry under several environmental conditions, then rerunning the innermost (100 m resolution) nest of the model (orange box in Figure 5-9) for the same conditions with modified bathymetry, and quantifying any resulting differences in wave properties (e.g., height, period, direction, longshore wave energy flux), with particular attention to any changes near the coast. The SWAN model of the South Taranaki Bight at 100 m resolution provides a satisfactory representation of wave conditions into 10 m water depth (approximately the outer limit of the surf zone on this high energy coast), as demonstrated by the verification against instrument deployments at similar depths.

A full description of the wave model setup, input wave, wind, sea level and current fields, and validation and testing of range of likely seabed mound and pit configurations is given in Gorman (2012 and 2013).

For the purposes of the modelling, eight cases of modified bathymetry (representing different paths of operation) were chosen to perform the sensitivity studies (Figure 1-2). Case 1 is a worst case scenario in terms of potential effects on wave characteristics, as it has 9 – 10 m deep pits and 8 – 9 m tall mounds at either end of every lane, a scenario possible at the end of 10 years extraction and also assuming no mound deflation or slumping or pit infilling takes place by natural processes or engineering means during that 10-year-long period. Note that only small amounts of mound deflation or pit infilling in the 10-year period is likely. In section 6 of this report we undertake an analysis that shows that pit infilling and mound deflation will continue for time-scales of decades to centuries. Case 02 represents a best case situation where extraction operations result only in a 9 m tall mound at the SW start and 10 m deep pit at the end NE of an entire extraction block. The other cases consider various options for extraction.

Model simulation methodology

Two approaches were used to investigate the effects of possible seabed modifications:

1) Firstly the scenario-based simulations (sensitivity testing) tested all hypothetical bathymetry modifications using a limited set of environmental conditions, allowing an efficient evaluation and inter-comparison of the relative effects of different extraction options.

2) The second approach was to carry out a long-term (12-month) climate simulation to ensure that a more complete range of environmental conditions have been sampled, and to enable robust nearshore wave-climate statistics to be established, and effects of bathymetry modifications on those statistics to be quantified. This approach also

addresses potential changes in wave-driven sediment transport processes at the shoreline.

5.3.2 Scenario-based simulations - Wave transformations on the inner shelf

Selection of wave conditions to model

A limited set of offshore wave and wind conditions was selected from November 2011 in order to perform the sensitivity studies.

Swell from the south through southwest predominates at both boundaries of the model. Hence at most times wave conditions in the South Taranaki Bight will include the influence of a south-westerly swell component entering from the Tasman Sea, which will produce waves incident on the South Taranaki coast from directions somewhat west of shore-normal. We also need to include conditions incident more from the northwest, and from the south, in order to characterise wave conditions most favourable to wave-driven longshore transport.

We selected scenarios based on input wave conditions at (40.00°S, 174.0°E) near the southwest corner of the 100 m grid with the intention of covering a range of input directions, and representing storm conditions as well as moderate conditions.

The six scenarios were selected by first choosing three subsets of the record:

- records with north-westerly waves (peak direction greater than 290°)
- records with south-westerly waves (peak direction between 225° and 255°)
- records with southerly waves (peak direction less than 225°)

then choosing from each subset the record with: 1) the highest significant height and 2) the record with significant height closest to a target value of 2 m. These correspond to the events listed in Table 5-1 . Each of the six environmental scenarios described above were applied in testing each variation of bathymetry.

Table 5-1: Wave parameters at (40.00°S, 174.0°E) for the six scenarios used in the wave sensitivity studies.

Scenario No.	Date & time	Subset of record	Height H_{m0} (m)	Direction θ_{peak} (°)
1	03Z 11/09/2011	NW	2.12	321
2	01Z 12/09/2011	NW	4.76	295
3	15Z 17/09/2011	SW	2.00	254
4	10Z 19/09/2011	S	1.87	173
5	14Z 19/09/2011	S	2.42	162
6	08Z 25/09/2011	SW	2.43	254

Simulations with unmodified (baseline) bathymetry

The first step in the modelling exercise was to run baseline simulations with unmodified bathymetry (no pits or mounds). The results of the model simulations are presented as maps showing how wave height changes throughout the model domain.

A model run with, for example, scenario 6 (an event with offshore waves of 2.43 m significant height from the WSW, which is about the direction the prevailing waves come from) shows that wave characteristics change quite markedly as the waves travel toward the shore under natural (no pits or mounds) conditions. Wave heights in this scenario (Figure 5-10) reduce in height shoreward to 1.5 m or less due to bed friction and, particularly in depths of less than 10 m, depth-limited breaking. As they travel towards the shore the waves refract and change direction as they pass over the banks and shoals and ridges on the seafloor. Close to shore, refraction turns the wave directions closer to shore-normal.

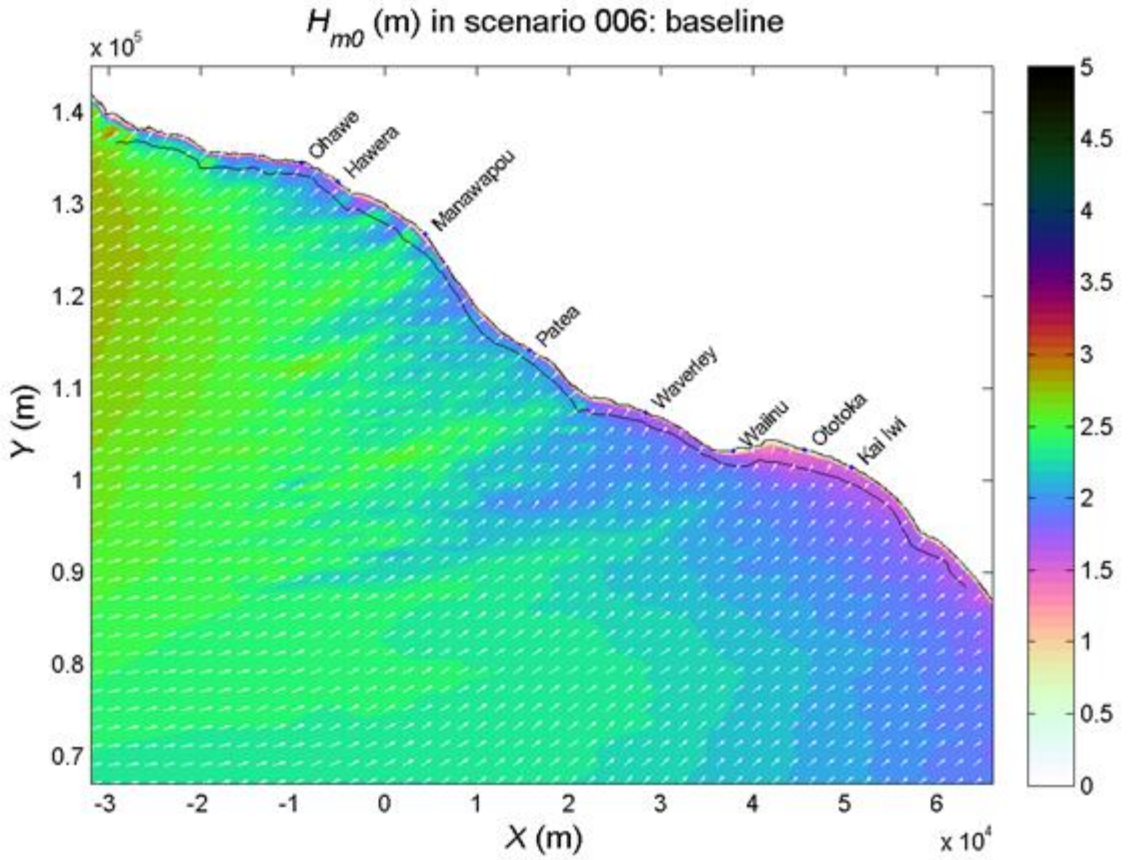

Figure 5-10: Wave conditions in environmental scenario 6, with existing bathymetry. Significant wave height is shown by the colour scale, and mean wave direction by arrows. Beaches surveyed in related studies are named, and the 10 m isobath (depth contour) is marked by a black line. The place names on the map are the 8 beaches where beach profiling was undertaken.

Simulations with modified bathymetry

The next step was to rerun the simulation with the same environmental conditions (incident waves, winds), but with bathymetry modified for each of the hypothetical test cases, and look at the change in difference in wave parameters between the two simulations.

For example, Figure 5-11 shows the difference (test case minus baseline) in significant wave height under environmental scenario 6 for bathymetry case 1 (Figure 1-2, top left panel). Case 1 represents a worst case scenario in terms of potential effects on waves as it has pits and mounds at either end of every lane over the entire project area. The figure shows that seabed modifications due to sand extraction produce increases in wave height (red colours) north of Patea of the order of 10 cm, while the blue colours indicate wave heights decreased by the order of 10 cm focussing on Patea. In this case, the majority of the extraction blocks consist of a 1 m deep depression, with a deeper pit at the NE end and a mound at the SW end, but on average the extraction areas have increased depth. The net result is a pattern of reduced heights (by some 10 cm) for waves in the down-wave shadow of the extraction areas, while heights are increased (by around 10 cm) on the northwest and southeast sides of this shadow area. We see a more amplified version of this refraction effect in the vicinity of the deeper pits at the NE end of the lanes and some focussing effects over the mounds at the SW ends. Those wave components refracted away from the initial direction continue to propagate in a wide range of north-eastward and south-eastward directions. The large spatial extent of the affected extraction area in this particular bathymetry case means that the effects on wave conditions are also quite widely spread. In other cases with more localised seabed modifications, the wide directional spread of the refracted waves acts to reduce the energy of this refracted component as it travels shoreward, so it makes a relatively minor contribution to the sea state further shoreward, on top of the incident waves travelling generally north-eastward that bypass the extraction area.

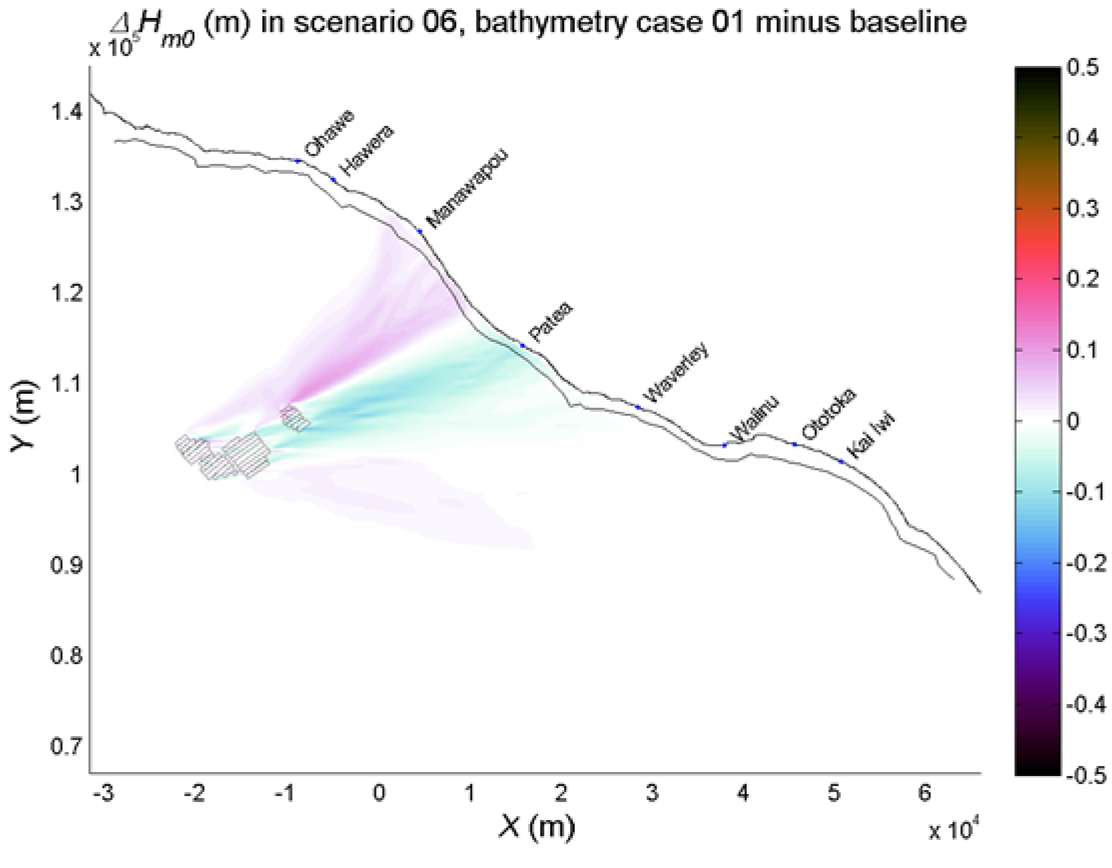

Figure 5-11: Difference between significant wave height for case 1 and existing bathymetry, over the model domain, for environmental scenario 6 (2.4 m high waves from the SW). The locations of the extraction areas are marked in grey. Beaches surveyed in related studies are named. The 10 m isobath (depth contour) is marked by a black line.

In this manner, modelling was undertaken on all the six environmental scenarios, providing a spread of baseline conditions including a range of southerly through westerly incident directions, and the patterns of disturbance in waves as they travel over the modified bathymetry in the sand extraction areas and toward the shore.

Figure 5-12 for example, shows how waves representing all the 6 wave scenarios change as they pass through the extraction site and over the **case 1 bathymetry modifications** and focus at different places along the shore, resulting in changes in wave height along the shore. Importantly these changes are generally small and less than ± 10 cm.

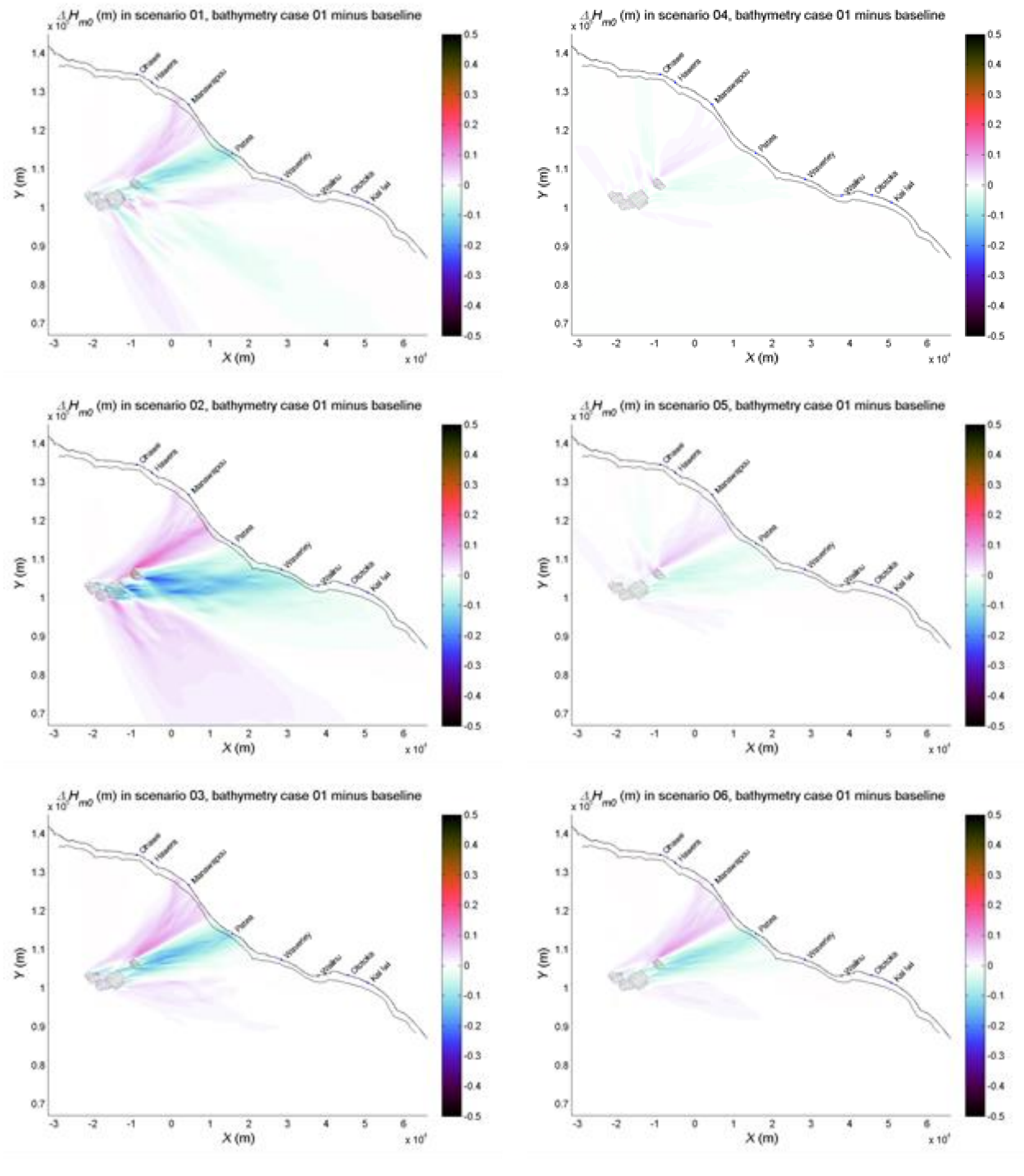

Figure 5-12: Difference between significant wave height for case 1 and existing bathymetry, over the model domain, for each of the six environmental scenarios.

By way of contrast, Figure 5-13 shows the effect on waves of the **case 3 bathymetry modifications**. While the distribution pattern for case 3 is similar to case 1, the magnitude of change is less because although the extraction area is closer to shore, it covers a smaller area and there are less pits and mounds for case 3.

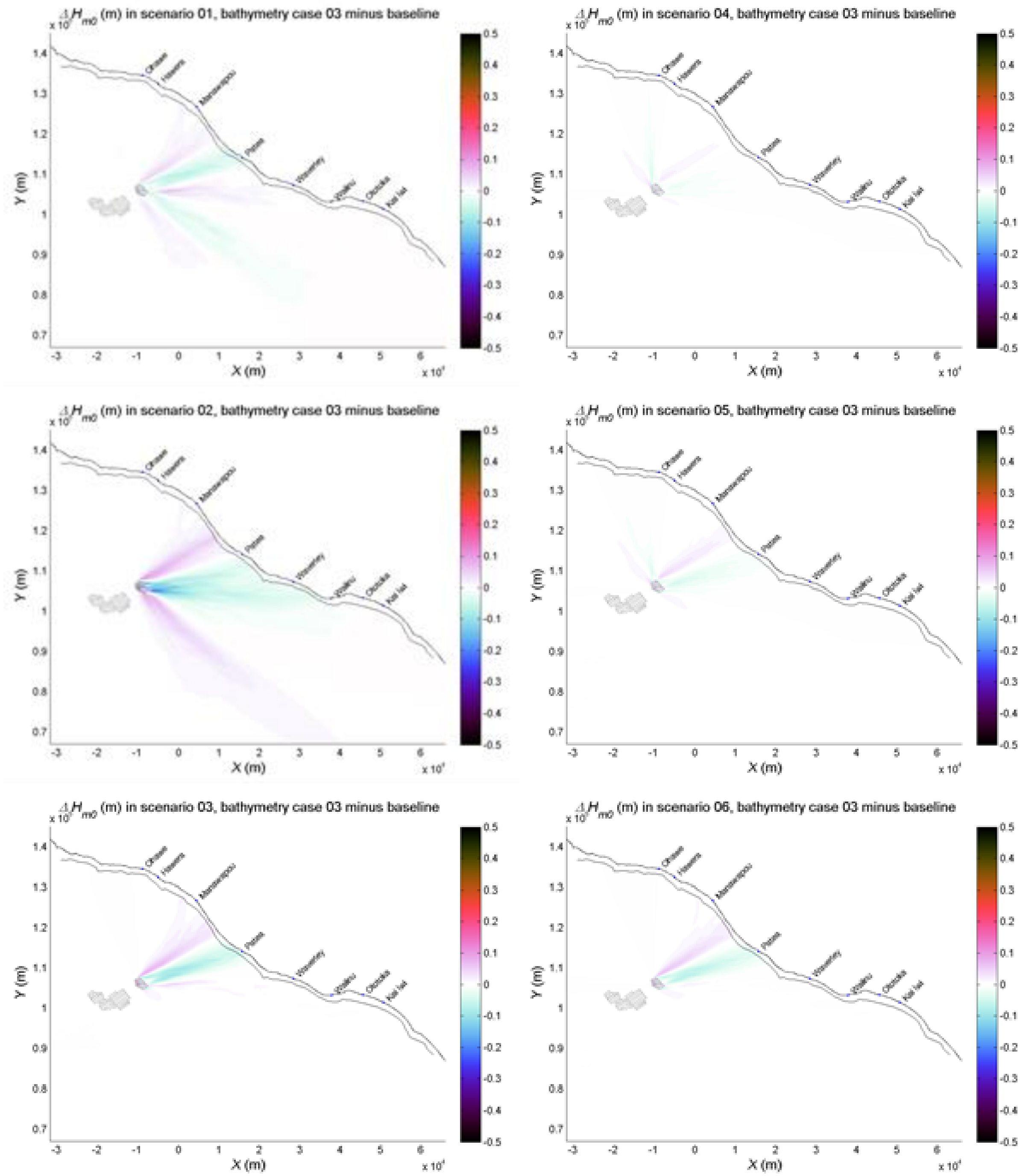

Figure 5-13: Difference between significant wave height for case 3 and existing bathymetry, over the model domain, for each of the six environmental scenarios. The locations of the pit and mound used in the simulations are marked in red.

A full description of the effects associated with all the 8 modified bathymetry scenarios is provided in Gorman (2013).

5.3.3 Scenario-based simulations – Wave transformations in the nearshore

In considering coastal stability, we are most interested in nearshore wave conditions as waves drive currents and sand transport in the nearshore zone and therefore the patterns of erosion and accretion along the shore. Therefore the results of the model simulations are next presented as values of wave statistics (significant wave height, mean wave direction, mean wave period and root-mean-square bed orbital velocity) along the 10 m isobath which is approximately the outer edge of the surf zone. Wave simulations are shown for:

1) Baseline bathymetry conditions - for all 6 environmental scenarios listed in Table 5-1.

2) The modified (with extraction) versus unmodified (no extraction = baseline) bathymetry conditions for all 6 environmental scenarios listed in Table 5-1.

Existing (baseline) bathymetry

Figure 5-14 shows the wave parameters at the 10 m isobath with existing bathymetry.

In these plots the horizontal scale is distance along the section of the 10 m isobath marked in Figure 5-10 moving from northwest (near Hawera) to southeast (near Wanganui). We note that all 6 environmental scenarios (Figure 5-14) show a broadly similar variation along the shore, although the mean values vary between scenarios. This is a result of refraction and diffraction over bathymetric features on the seabed imposing a consistent finer scale structure on wave fields that are more homogeneous further offshore where the seabed is more regular in shape and the water deeper. Importantly it shows that wave characteristics change quite markedly along the shore under natural (no pits or mounds) conditions. For instance, for scenario 1 (the blue line), a 2.12 m wave entering the model domain from the NW varies in height to from 2.0 – 0.6 m along the 10 m contour.

Bathymetry modifications

The **case 1 bathymetry modifications** (Figure 1-2, top left panel) represent a worst case situation as it contains the greatest number of pits and mounds and represents extraction over a long period of time (10 years) with no pit infilling or mound deflation or slumping by natural processes (waves and currents). In Figure 5-15 we observe a pattern of increases in wave height by up to 5 – 9 cm between Hawea and Patea, a decrease of up to 11 cm near Patea, smaller decreases (< 7 cm) to the south and with little change south of about Waitotara. The changes in mean period show a similar pattern, because changes associated with refraction by bathymetric features will have a greater influence on long period wave components, so in places where some energy has been removed, this will tend to reduce the mean period as well as the significant wave height (and vice versa). Changes in mean wave direction are generally less that 1°, either positive (i.e., clockwise) or negative, but with larger changes, around -2° (i.e., an anticlockwise shift) in a localised area west of Manawapou.

By way of contrast with case 1, the **case 3 bathymetry modifications** (Figure 5-16) show a similar pattern of distribution in changes in wave characteristics along the shore, but the magnitude of changes is far less. Wave height increases by 1 – 5 cm east of Manawapou, and decreases by 1 – 5 cm west of Patea. Changes in wave direction are and less than 1° and mostly negative (a slight anticlockwise shift). Changes in wave period are less than 0.2 sec. The magnitude of change is less for case 3 (cf. case 1) because although the extraction area is closer to shore, it is over a smaller area and there are fewer pits and mounds for case 3.

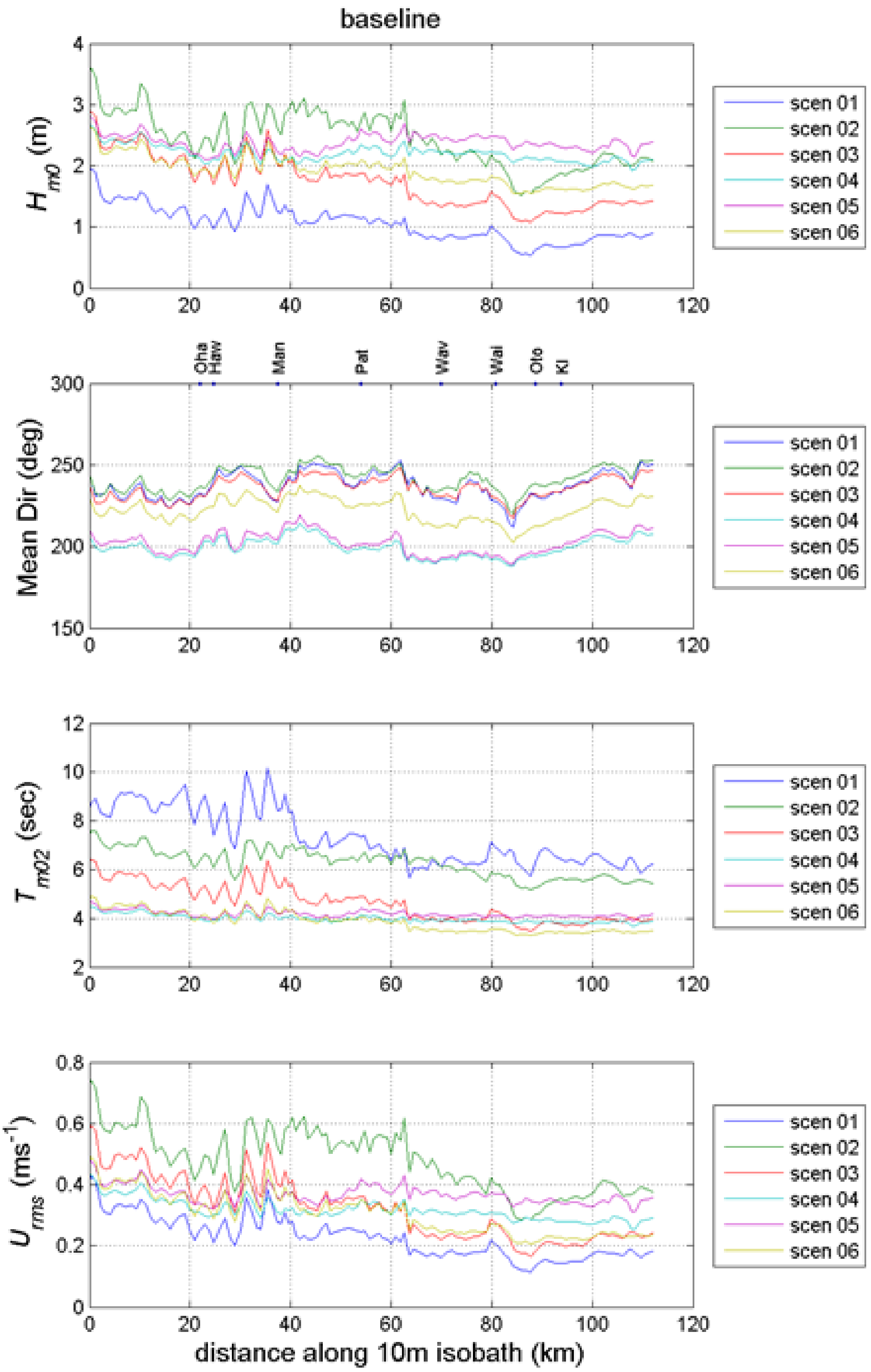

Figure 5-14: Wave parameters at the 10 m isobath with existing (baseline) bathymetry, in all 6 environmental scenarios. From top to bottom: significant wave height, mean wave direction, mean wave period, and root-mean-square bed orbital velocity. Locations of the beaches surveyed are shown above the 2nd panel. Place names on the 2nd panel map are beaches where profiling was undertaken.

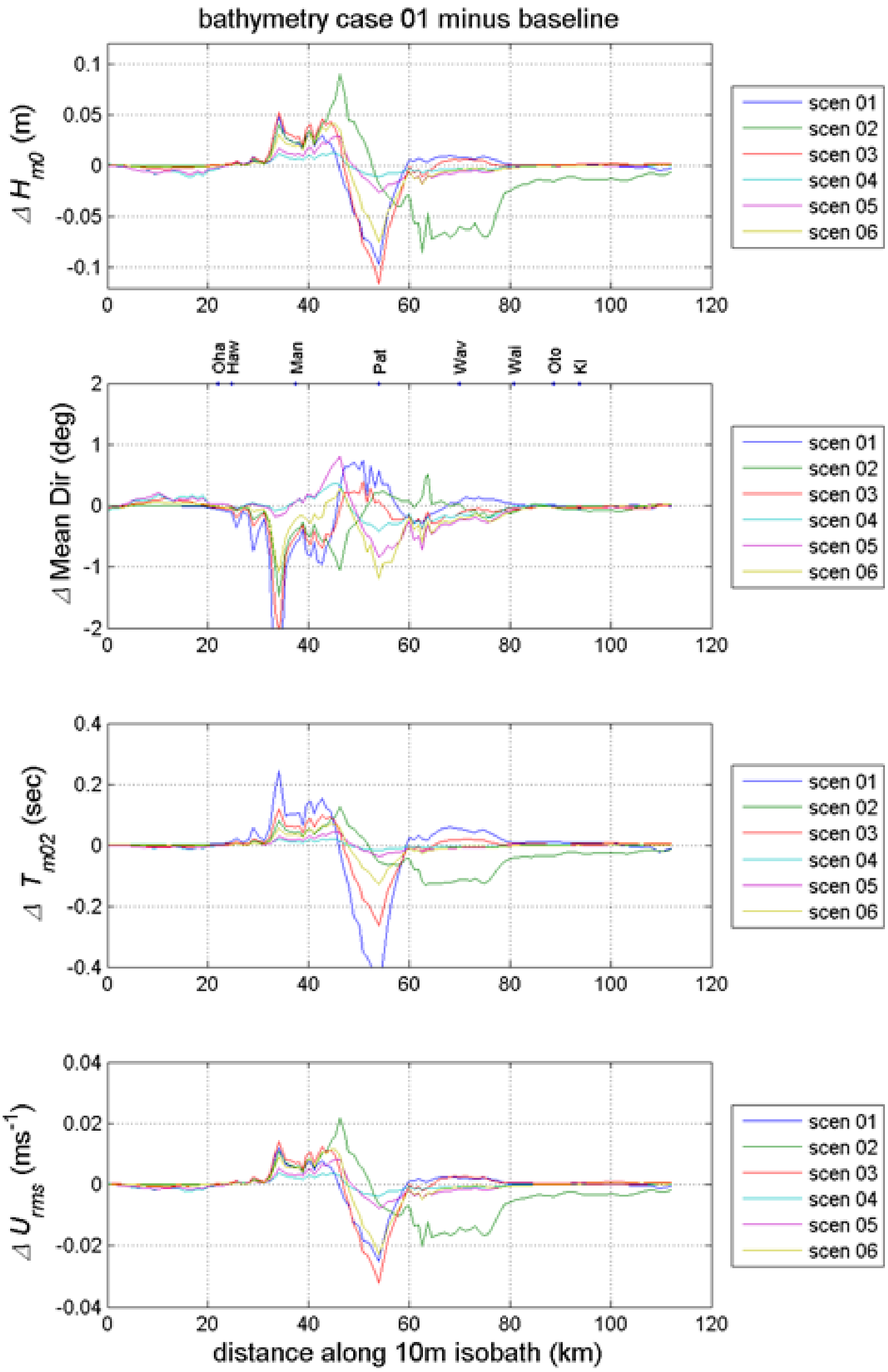

Figure 5-15: Difference between wave parameters at the 10 m isobath for case 1 and existing bathymetry, in all 6 environmental scenarios. From top to bottom: significant wave height, mean wave direction, mean wave period and root-mean-square bed orbital velocity are plotted as a function of distance along the 10 m isobath. Locations of the beaches surveyed are shown above the 2nd panel.

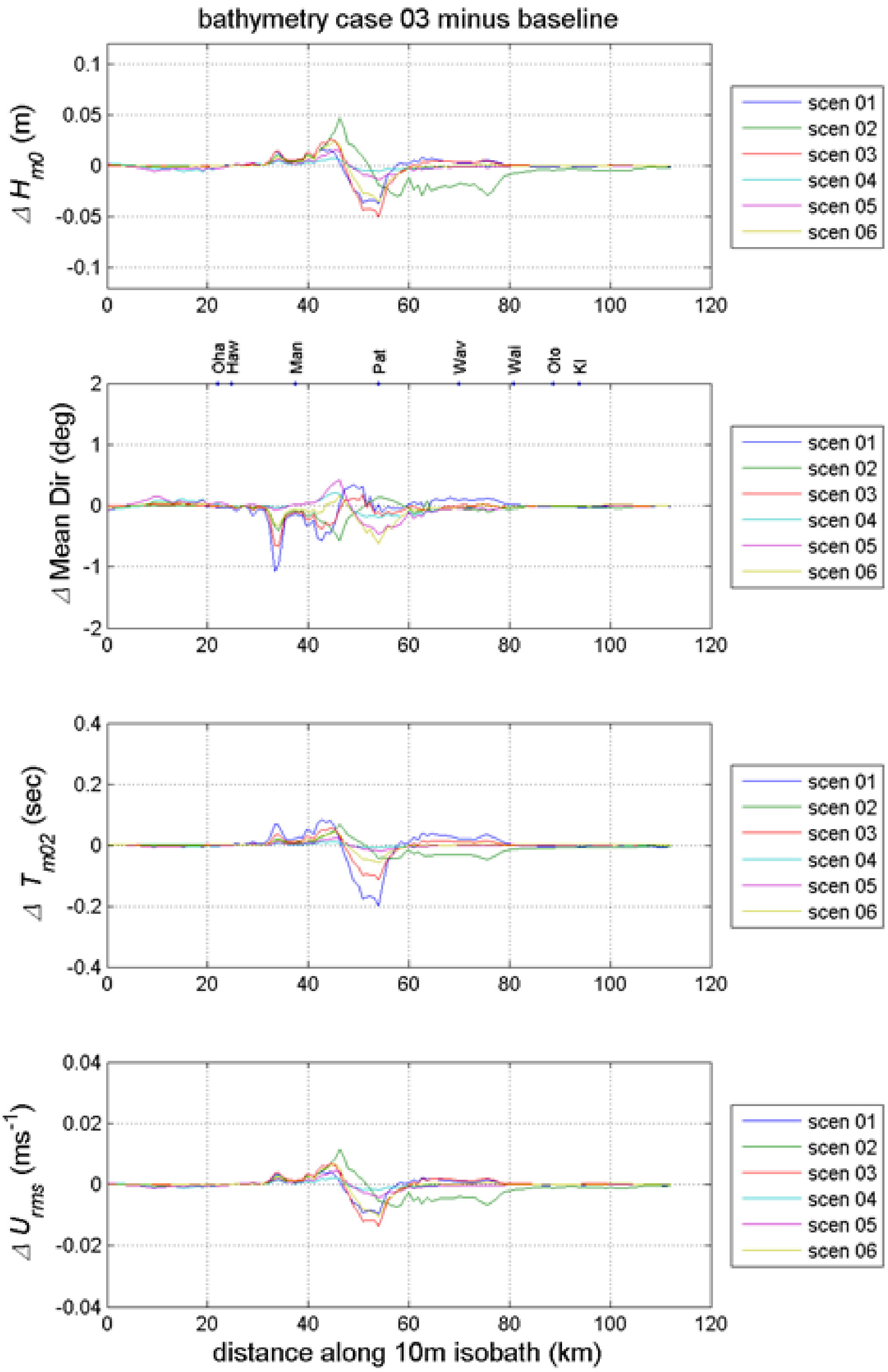

Figure 5-16: Difference between wave parameters at the 10 m isobath for case 3 and existing bathymetry, in all 6 environmental scenarios. From top to bottom: significant wave height, mean wave direction, mean wave period, and root-mean-square bed orbital velocity.

For **case 1 bathymetry modifications** we can summarise these results by looking at the maximum and mean (across all environmental scenarios) value in magnitude changes of wave parameters at the 10 m isobath, shown in Figure 5-17 and Figure 5-18, respectively, for all bathymetry cases. Changes in significant wave height are all less than 12 cm for case 1, and less than 5 cm for other cases. These are closely correlated with changes in mean period, all less than 0.5 seconds for case 1, and half that for other cases. The largest impacts (from case 1) occur as a decrease in heights and periods near Patea.

We can also look at this in relative terms, i.e., the magnitude of change as a percentage of the baseline value, plotted as maximum and mean values in Figure 5-19 and Figure 5-20, respectively. These show changes in significant wave height and mean period remain less than 8.6% for the maxima in case 1, 4.5% for the other seven cases, while average changes are less than 3.5% for case 1, or less than 1.5% for other cases. Changes in bed-orbital velocity, which tend to compound coincident changes in height and period, are slightly higher in percentage terms.

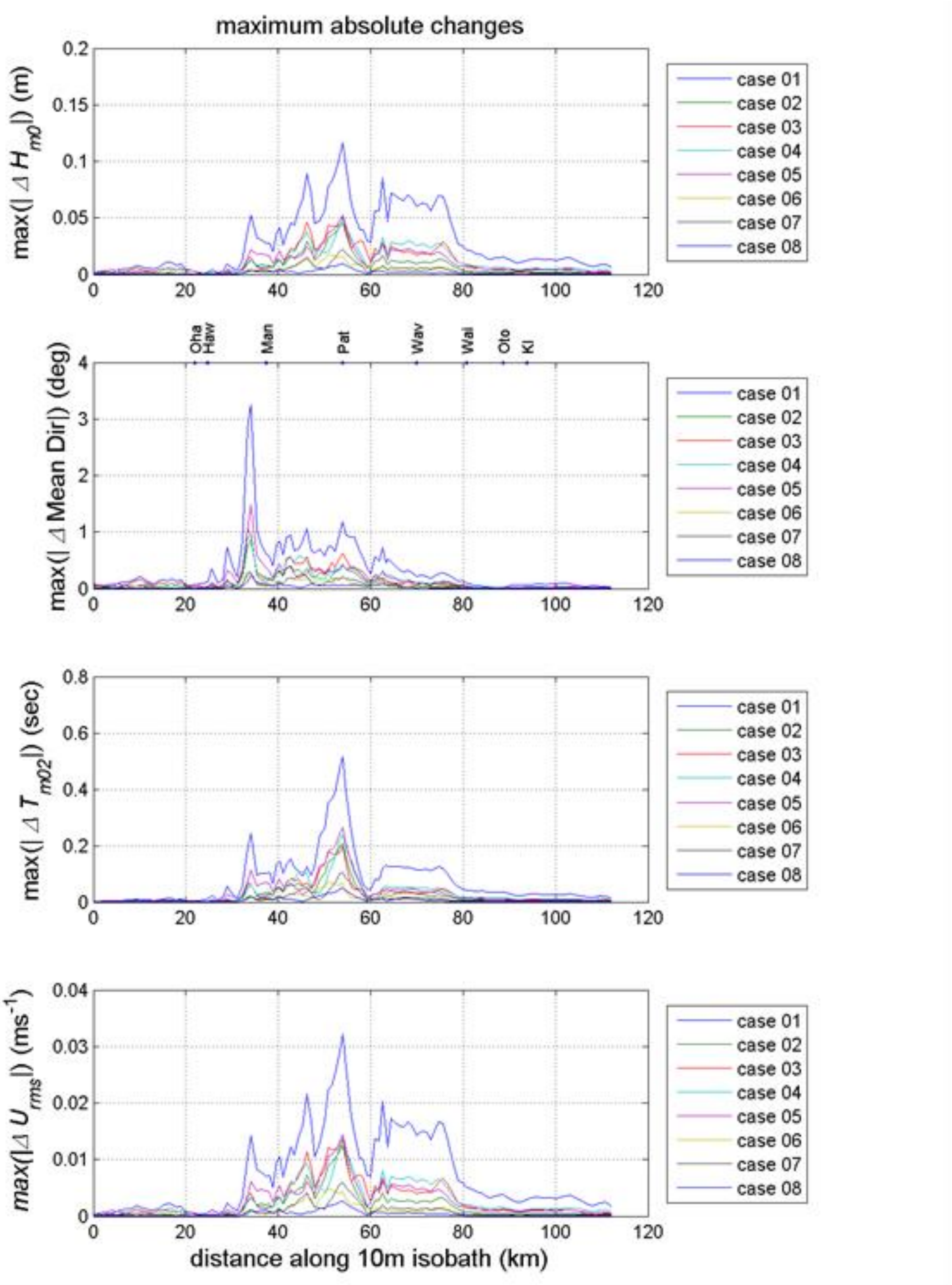

Figure 5-17: Maximum (over six environmental scenarios) of the absolute change in wave parameters at the 10m isobath. Values are plotted for all bathymetry cases, as a function of distance along the 10 m isobath.

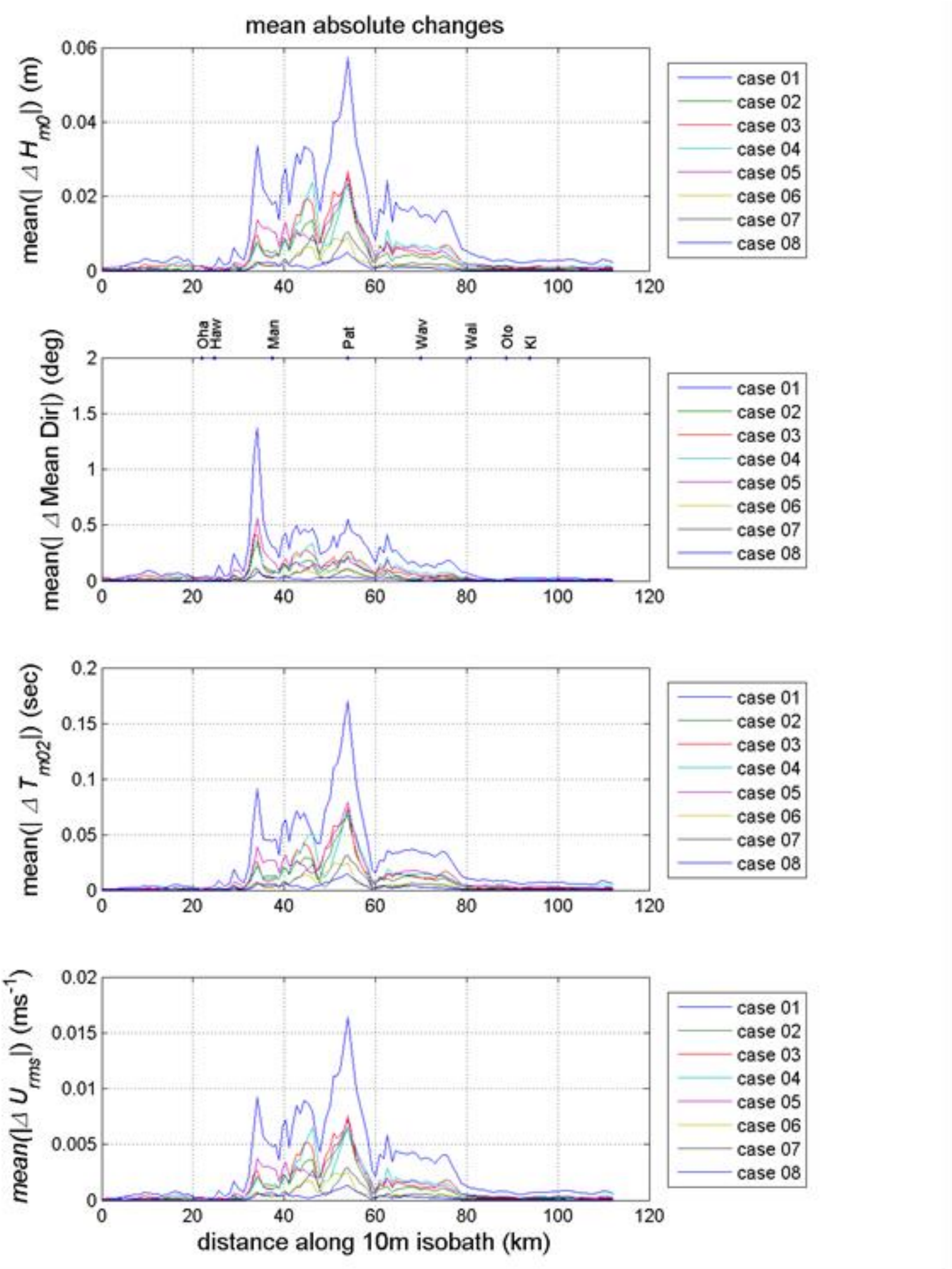

Figure 5-18: Mean (over six environmental scenarios) of the absolute change in wave parameters (in metres) at the 10m isobath. Values are plotted for all bathymetry cases, as a function of distance along the 10 m isobath.

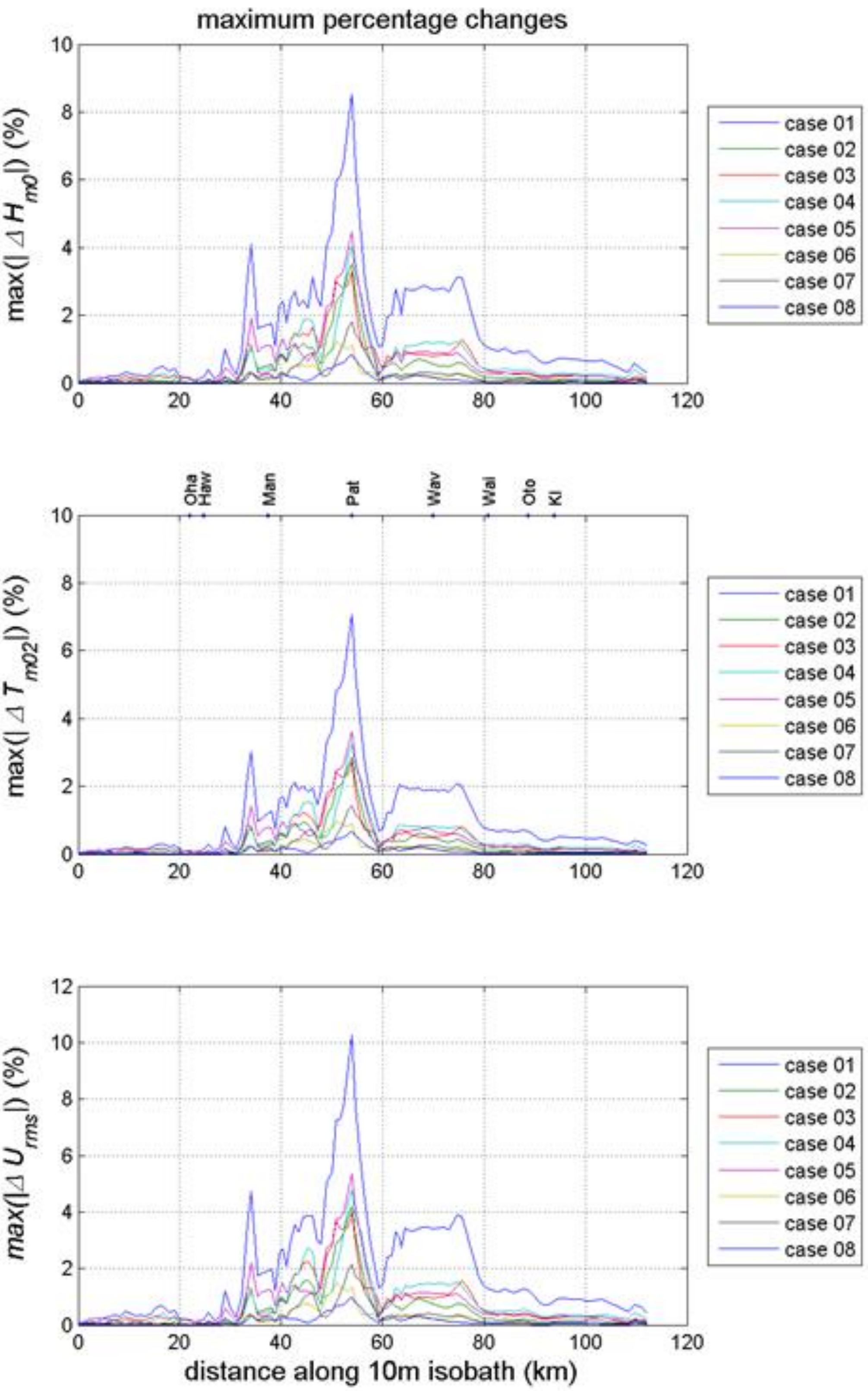

Figure 5-19: Maximum (over six environmental scenarios) of the relative change in wave parameters (as a fraction of the baseline values) at the 10m isobath. Values are plotted for all bathymetry cases, as a function of distance along the 10 m isobath.

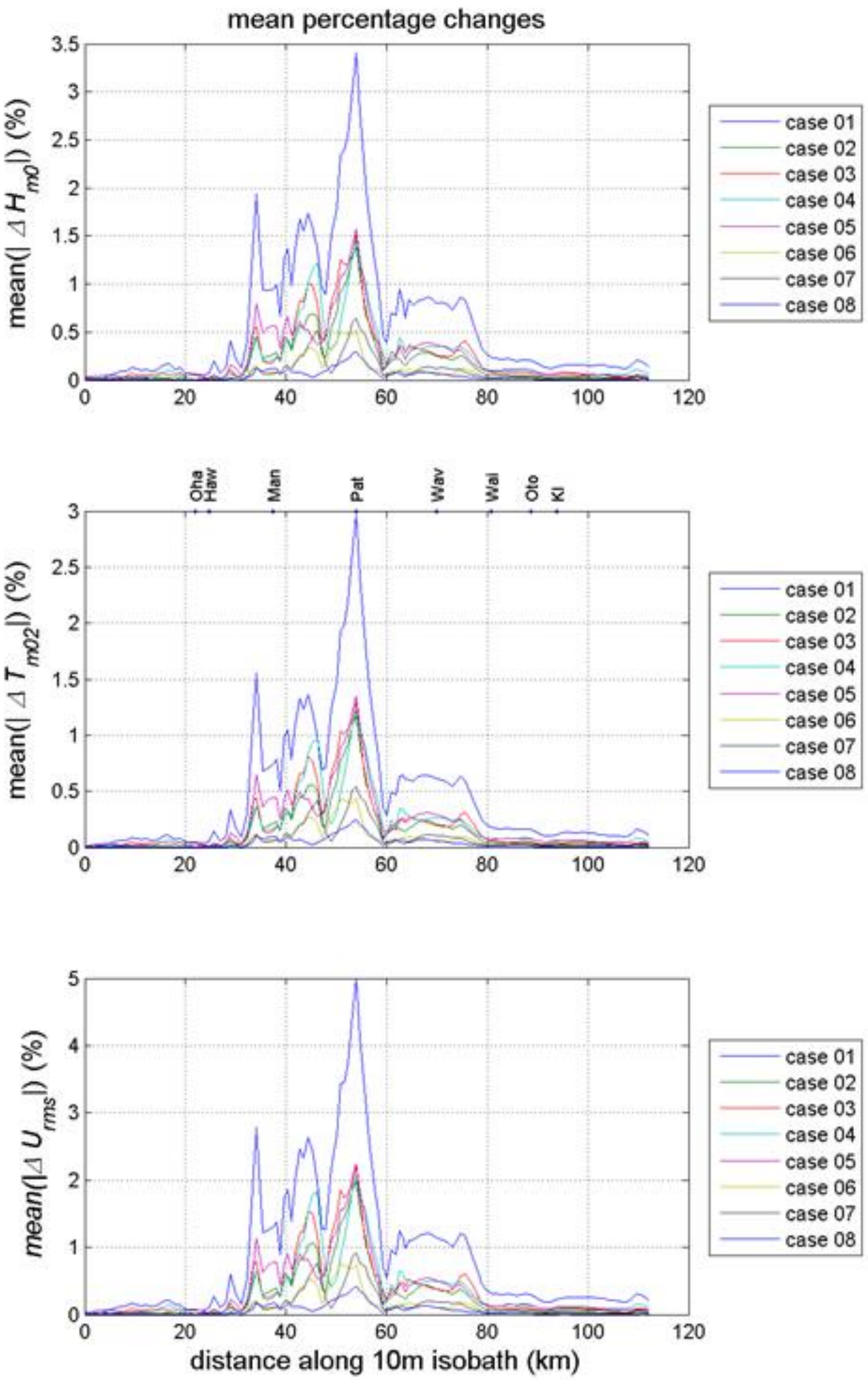

Figure 5-20: Mean (over six environmental scenarios) of the relative change in wave parameters (as a fraction of the baseline values) at the 10m isobath. Values are plotted for all bathymetry cases, as a function of distance along the 10 m isobath.

Summary of effects of sand extraction on waves

The maximum changes in significant wave height predicted for the eight bathymetry modification cases and reported as the difference in wave height between the baseline and modified bathymetry are summarised in Table 5-2. The table shows maximum changes in wave height over all six environmental scenarios, and either over the whole modelling domain or along the 10 m isobath.

In the full model domain the maximum changes are 0.44 m in wave height or up to 13%.

Table 5-2: Maximum changes in significant wave height predicted for the eight bathymetry modification cases. Changes are expressed in absolute terms (metres) and relative terms (%), either over the full model domain or along the 10 m isobath.

Extraction case	Full domain H max (m)	Full domain H max (%)	10 m isobath H max (m)	10 m isobaths H max (%)
1	0.436	12.6	0.116	9.2
2	0.232	9.0	0.045	3.8
3	0.348	10.9	0.050	3.5
4	0.245	10.0	0.050	4.3
5	0.228	9.1	0.052	4.8
6	0.239	7.9	0.018	1.4
7	0.177	6.6	0.022	1.9
8	0.096	4.6	0.010	0.9

At the 10 m isobath, which is about the seaward edge of the surf zone, the changes in wave characteristics due to extraction are much smaller than the changes further offshore. The magnitude of change as a percentage of the baseline value show changes in significant wave height remain less than 9.2% for the maximal case 1 bathymetry modifications, and less than 4.8% for other cases. Case 1 is a worst case situation where large pits and mounds occur at the start of every lane. This assumes that the pits will not infill and the mounds will not slump or be eroded by waves and currents to any degree over the time that it takes to extract from the whole area (perhaps 10 years). Changes in wave direction are generally less than 1 degree, increasing locally to 3 degrees west of Manawapou. This is insignificant when compared to the variability in wave approach throughout the year (refer to Figure 5-4 and Figure 5-5).

The overall conclusion from the scenario-based modelling is that the proposed sand extraction operations will have only minor effects on wave conditions by refraction (bending the wave path) and diffraction (lateral dispersion of wave energy) and locally by shoaling (changing the wave height) them as they pass over the modified seabed.

5.3.4 Long-term wave climate simulation

Effect on waves at the 10 m isobath

To complement the scenario-based approach, a second approach was to run direct simulations of sufficiently long duration to characterise the nearshore wave climate, with both existing and modified bathymetry. This allows for the effects of the bathymetry modifications on the wave characteristics to be tested over a wide sampling of the local wave climate. However, because of the high computing resource required for this 12-month long simulation, it was only practical to test one representative bathymetry case in this way[7]. Case 1, representing the most extensive possible bathymetry modifications, was selected for this test. Details of this modelling are reported in Gorman (2013) and summarised below.

The long-term simulations used the SWAN wave model to simulate wave conditions over a 12-month period (January 2011 through December 2011) after a “spinup” period from 21 December 2010 to initialise the model. These simulations provided full time series outputs of wave statistics on the 10 m isobaths at a time step of 1 hour.

Gorman (2013) undertook an analysis to check that the 2011 was a suitably representative year, by comparing the statistical occurrence of wave statistics at 40.00°S, 174.0°E (near the southwest corner of the 100 m grid – see section 5.3.2) for five years for which NZWAVE-12 outputs are available. The analysis showed that the deviations of the 2011 occurrence distributions from the five-year average significant wave height, mean wave period and mean wave direction are of similar magnitude to those of other years in the record, although the mean direction is somewhat more concentrated into the two main peaks than for other four years.

In the following plots we show various outputs from the model for baseline and the bathymetry modified case. In these plots the mean is calculated as an average of the hourly values over the year. Nearshore statistics were computed at 122 points over a 112 km length of contour. Standard deviation (SDh) was calculated in the same manner from the hourly data.

This was done first for the existing bathymetry, to provide a baseline. Figure 5-21 shows the time averages, and standard deviations (SDh), of output wave parameters on the 10 m isobath for the baseline simulation. Comparison with Figure 5-14 shows that the nearshore outputs of individual scenario runs are consistent with the longer term statistics, with the spatial variation of significant wave height, mean period and bed orbital velocity lying around or above one standard deviation (SDh) over the yearly mean. This is as we would expect for conditions selected from the more energetic parts of a one-month record. Also, the envelope of nearshore wave directions overlaps closely with a one standard deviation range about the mean.

The simulations (Figure 5-21) show that under baseline (no extraction) conditions there is considerable variation throughout a year in wave conditions at the shore. In Figure 5-21 the mean values are plotted along with one standard deviation (SDh). One standard deviation (SDh) incorporates approximately 68% of the variability of a random variable, thus there is a 32% chance that any value will fall outside the envelope about the mean. The graphs show

[7] The scenario-based approach reported earlier requires much shorter computing times, making it suitable for the efficient inter-comparison of a relatively large number of bathymetry modifications

that for 68% of the 1-year model simulation mean significant wave height varies by ±0.7 m, mean wave direction varies by ±25 degrees, the mean wave period by about ±1 second and the bed orbital velocity by about ±0.15 m/s, as waves of varying size approach the shore from varying angles. Overall wave height, period and orbital velocity decrease alongshore to the SE as the environment becomes more sheltered. Mean direction does not show a similar trend, being affected by the complex bathymetry in the nearshore and local coastal alignment and a weakening of the influence of westerly swell in the south (relative to southerly swell).

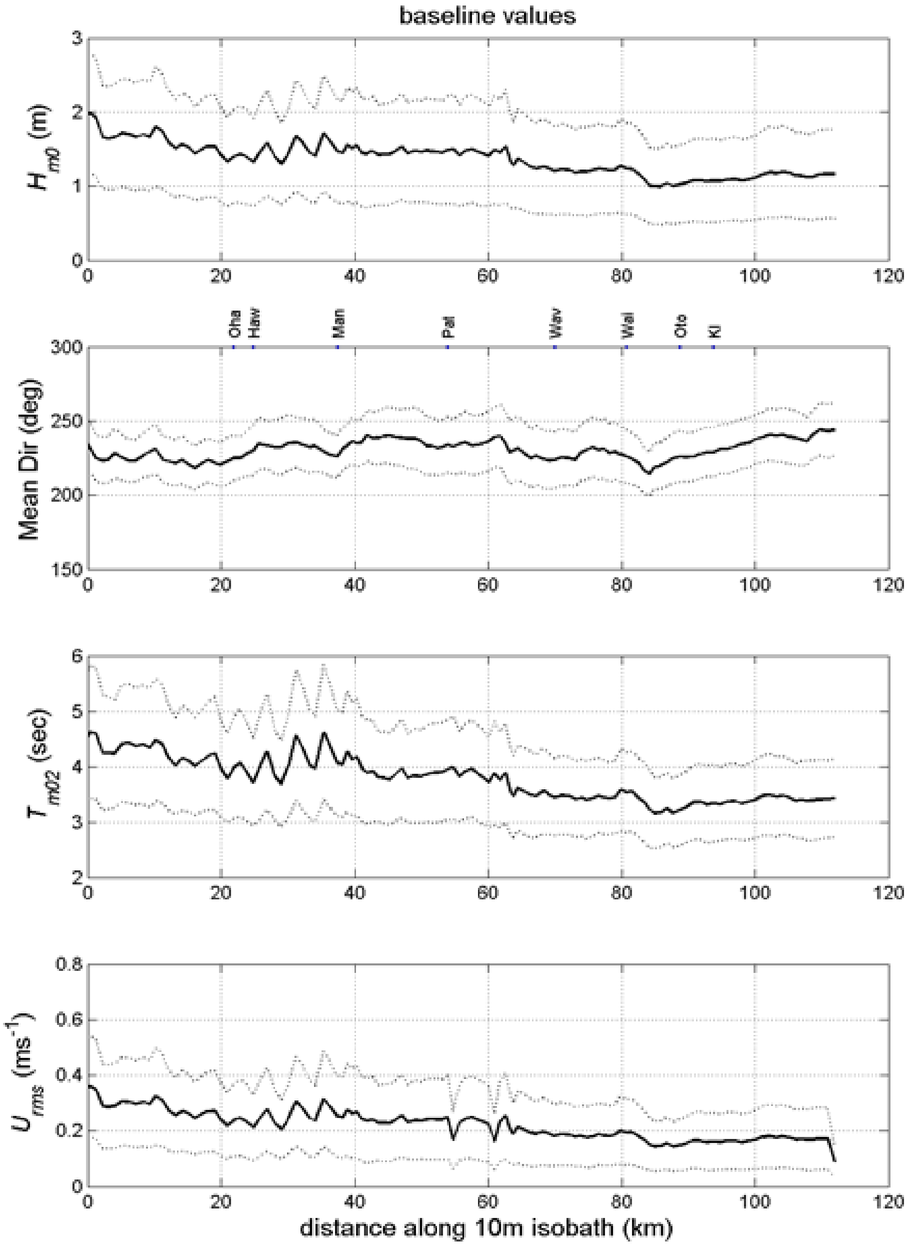

Figure 5-21: Mean values and standard deviation of wave statistics at the 10 m isobath, from the baseline long-term simulation. Mean values (over a 12 month period) from the baseline simulation are shown by solid black lines, plus and minus one standard deviation (dashed lines). Statistics shown are, from the top, significant wave height, mean wave direction, second-moment mean wave period and root-mean square bed orbital velocity.

The next step was to take account of the case 1 bathymetry modifications. Figure 5-22 shows the mean difference, or bias, between wave statistics from the case 1 test and baseline simulations. We see that the bathymetry modifications introduce a mean decrease (by < 5 cm) in significant wave height on the coast near Patea, with smaller increases (of < 2.5 cm) further west in the vicinity of Manawapou. Along the remainder of the 120 km length of shoreline there is zero change. Comparison with Figure 5-15 shows that the behaviour of the individual scenarios are consistent with the yearly averages, which generally correspond to the lower end of the range of variability covered by the scenarios. The standard deviation in the differences illustrates that the mean differences in significant wave height associated with the bathymetry change generally differ from zero by around one standard deviation, which corresponds to a 68% confidence level. Similar results apply to mean wave direction and bed orbital velocity, while the bias in mean period differs from zero by somewhat less than one standard deviation. Mean wave period decreases (by < 0.1 seconds) in the vicinity of Patea, and increases (by < 0.06 seconds) to the west. Mean wave direction is slightly decreased (i.e., changes in an anticlockwise sense) on average along the majority of the coast, as far east as Waverley, beyond which there is zero change. For all four variables, this range of variability in the differences associated with the bathymetry changes is considerably less than the corresponding natural range of variability in baseline values illustrated in Figure 5-21.

Various other statistical measures of the effects of bathymetry modification can be calculated. Figure 5-23 shows the root-mean-square difference (RMSD), between test and baseline statistics. RMSD is a useful statistic because, compared to calculating the bias (mean difference) where positive and negative changes will cancel out, the RMSD detects a difference in either sign. The RMSD shows the typical wave height differences of < 2.0 cm for much of the coast, up to a maximum of 5.5 cm near Patea.

The mean relative magnitude difference (Figure 5-24) can be compared directly with Figure 5-20 which again shows consistency. By this measure the effects between Hawera and Waiinu of the bathymetry changes are generally < 1.5% for significant wave height and mean period (peaking at 2.7 and 2.5 % respectively at Patea). Along the remainder of the 120 km length of shoreline there is zero change.

The root-mean-square difference can also be divided by either the standard deviation or the mean of the baseline value to give a normalised measure (Figure 5-25). Note that for mean wave direction it only makes sense to normalise by the standard deviation. Dividing by the standard deviation we see that the effects of this particular bathymetry modification remain < 8% of one standard deviation for significant wave height, < 15% of one standard deviation for mean period, and < 10% of one standard deviation for bed-orbital velocity.

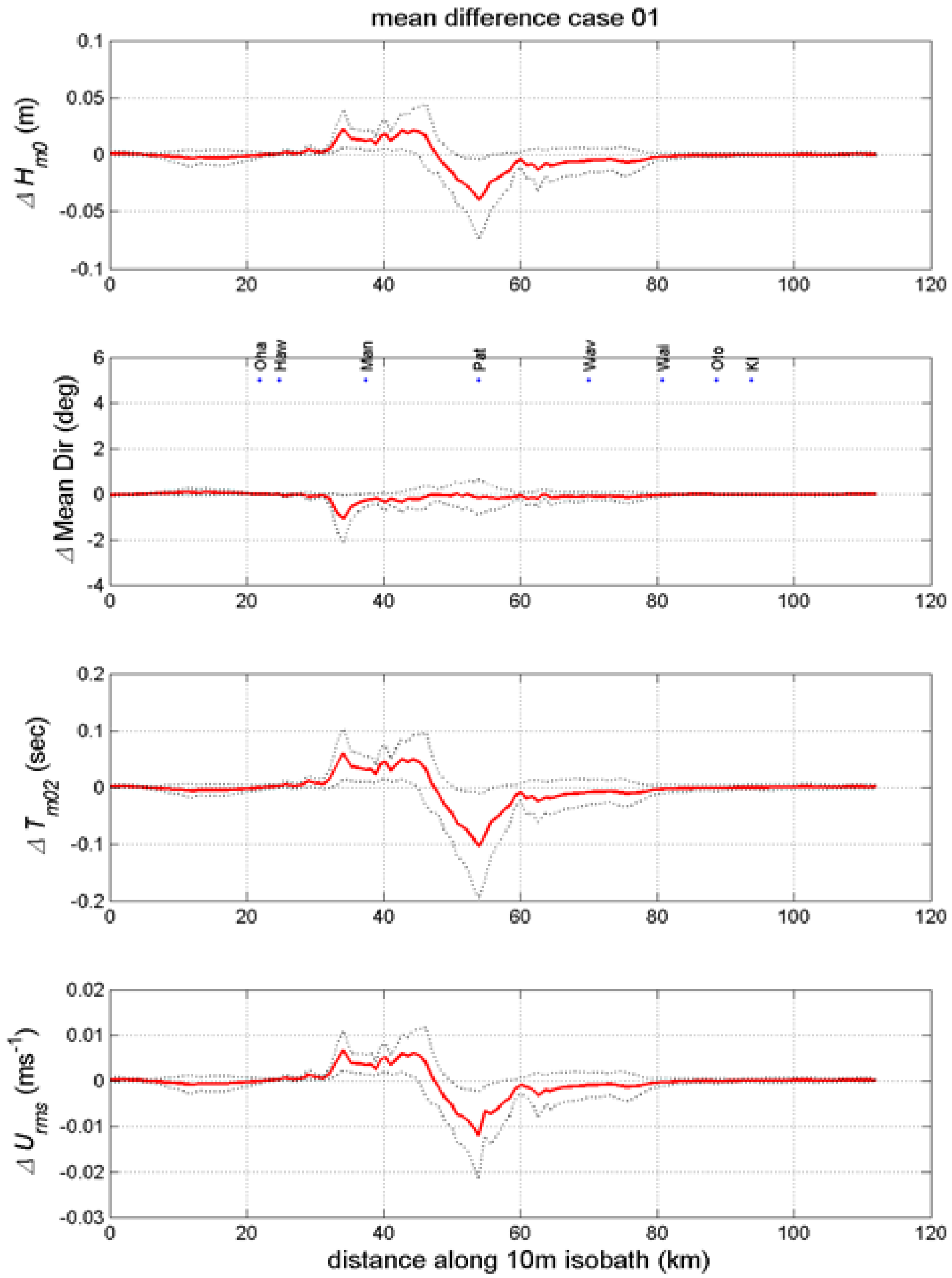

Figure 5-22: Mean difference (bias) and standard deviation of the difference between the case 1 and baseline long-term simulations of wave statistics at the 10 m isobath. Statistics shown are, from the top, significant wave height, mean wave direction, second-moment mean wave period and root- mean square bed orbital velocity. The dashed lines show one standard deviation either side of the mean (solid red lines).

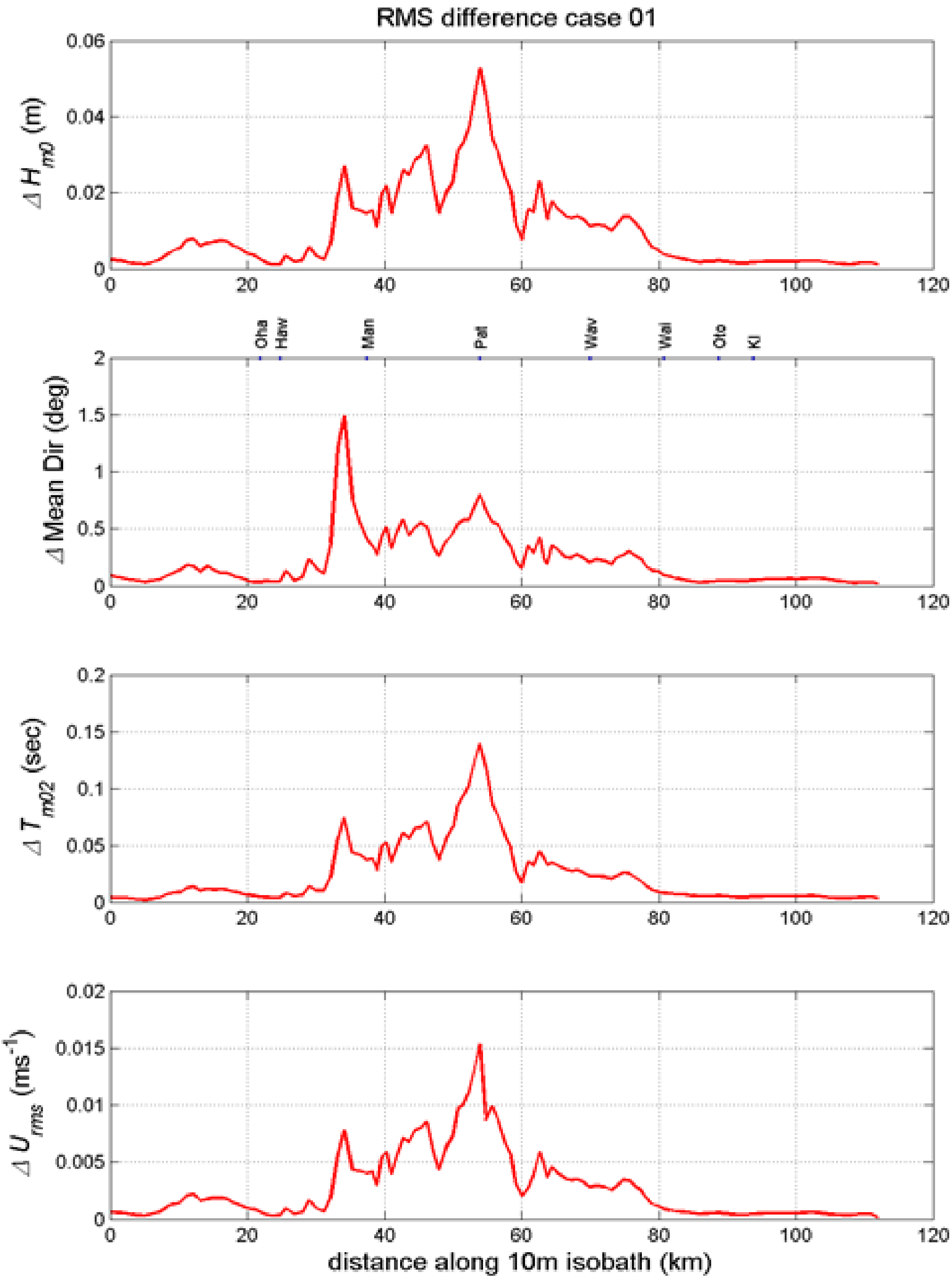

Figure 5-23: Root-mean-square difference in wave statistics at the 10 m isobath, between the case 1 and baseline long-term simulations. Statistics shown are, from the top, significant wave height, mean wave direction, second-moment mean wave period and root-mean square bed orbital velocity.

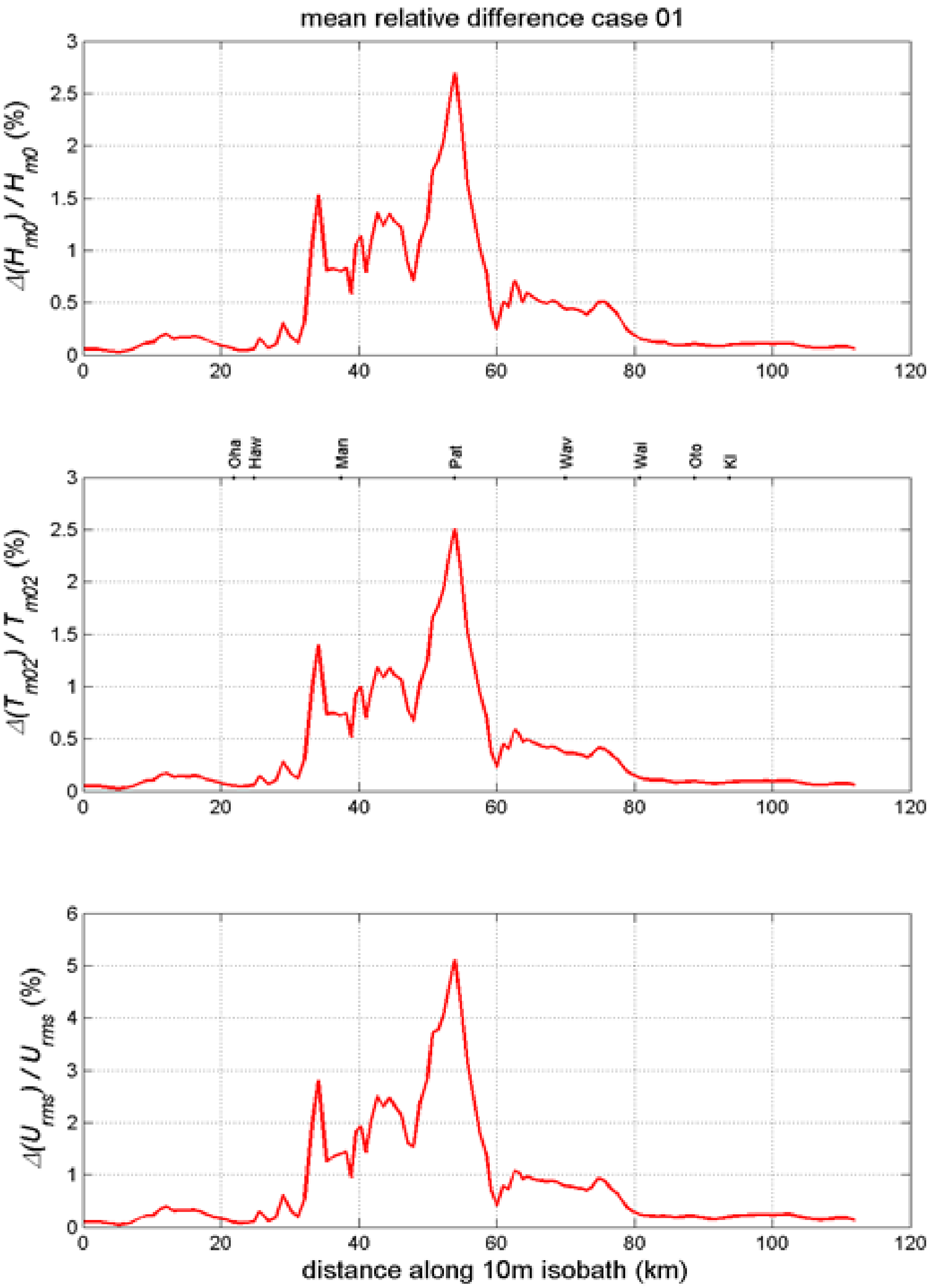

Figure 5-24: Mean fractional difference in values of wave statistics at the 10 m isobath, between the case 1 and baseline long-term simulations. Statistics shown are, from the top, significant wave height, second-moment mean wave period and root-mean square bed orbital velocity.

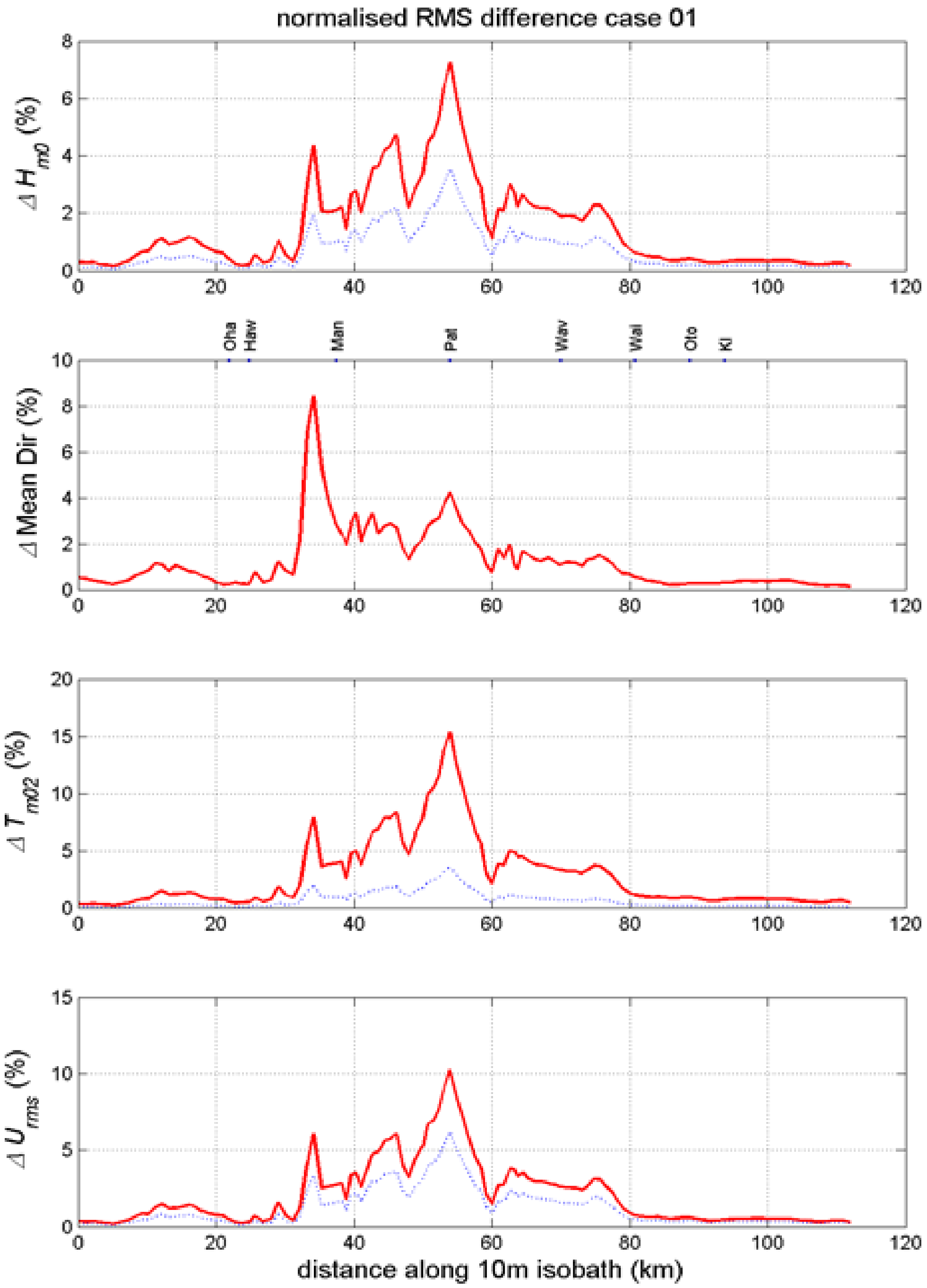

Figure 5-25: Normalised root-mean-square difference in wave statistics at the 10 m isobath, between the case 1 and baseline long-term simulations. The solid red lines and the dashed blue lines show the RMS difference normalised by the standard deviation and the mean, respectively, of the baseline value. Statistics shown are, from the top, significant wave height, mean wave direction, second-moment mean wave period and root-mean square bed orbital velocity.

Nearshore wave and sediment transport statistics

Having used the SWAN model to obtain detailed synthetic records of wave statistics at 10 m water depth, we then rely on empirical methods, as detailed in Gorman (2013), to estimate behaviour through the nearshore and surf zone, where the numerical model cannot be relied upon, largely due to limited availability of accurate and highly-resolved bathymetric data. This produces time series of various quantities at the shoreline, including breaking wave height H_b, longshore wave energy flux factor P_{ls} , onshore wave energy flux factor P_{os}, and contributions to the longshore mean current speed from the processes of oblique wave incidence ($V_{ls,obl}$) and wave height gradient ($V_{ls,hgrad}$). The wave-driven longshore sediment flux potential Q is taken as directly proportional to P_{ls} using a factor (K) of 0.8 (Gorman 2013).

In the following plots we show the spatial variation of various statistics derived from these quantities, both as coloured ribbon plots for means of baseline values, and as line plots against distance along the shore. We also show line plots of statistics quantifying the effect of the bathymetry modifications, in the form of bias and root mean square difference, both as absolute quantities and normalised by either the standard deviation or mean of the corresponding baseline values.

In this case to characterise the differences we use a more appropriate statistic for the standard deviation (SDm) calculated by first computing monthly means for the one year record and then taking the standard deviation of the 12 values.

For baseline bathymetry, mean values of breaking wave height (H_b) vary between 1.2 m and 2.2 m along the South Taranaki coast (Figure 5-26), generally decreasing from northwest to southeast. The case 1 bathymetry modifications acts to reduce mean values in the vicinity of Patea by < 5 cm, and to increase values by up to 2.5 cm in parts of the coast further west. The root mean square difference in H_b is generally less than 20% of one standard deviation (SDm).

The onshore wave energy flux factor P_{os} (Figure 5-27) shows generally similar behaviour to the breaking wave height, apart from having values somewhat larger for the case 1 bathymetry modifications between Manawapou and Patea where the coast is aligned more normal to the prevailing wave direction. The case 1 bathymetry modification introduces RMS differences generally less than 20% of one standard deviation.

The longshore wave energy flux factor P_{ls} (Figure 5-28) is important as the driver of longshore sediment transport. We have assumed that the longshore sediment transport potential Q is directly proportional to P_{ls} and so have simply used double axis scales to show both quantities on the same plot. The longshore flux can, in general, act in either direction along the coast. Here, positive values are defined as acting along the coast towards the SE, and we note that the time-average values of P_{ls} and Q are directed SE everywhere along the South Taranaki coast, as a result of its alignment to the generally westerly wave climate. The mean longshore wave energy flux factor has its largest values at the western end, and generally decreases eastwards with decreasing incident wave height, but with some variation due to local coastal alignment. This quantity also has a relatively large temporal variability, with the mean value almost always less than one standard deviation (SDh) from zero (meaning the net drift is small compared to the gross drift). The case 1 bathymetry modifications would act to decrease the longshore wave energy flux factor in the vicinity of

Patea (i.e., slightly reduce the positive SE sediment flux) by up to 10% of a standard deviation (SDh), or 8% of the mean. There would be a much smaller net increase in longshore wave energy flux on a small part of the coast west of Manawapou. Overall the change in longshore wave energy flux lies well within half the baseline standard deviation (SDm) (3rd panel from top of Figure 5-28).

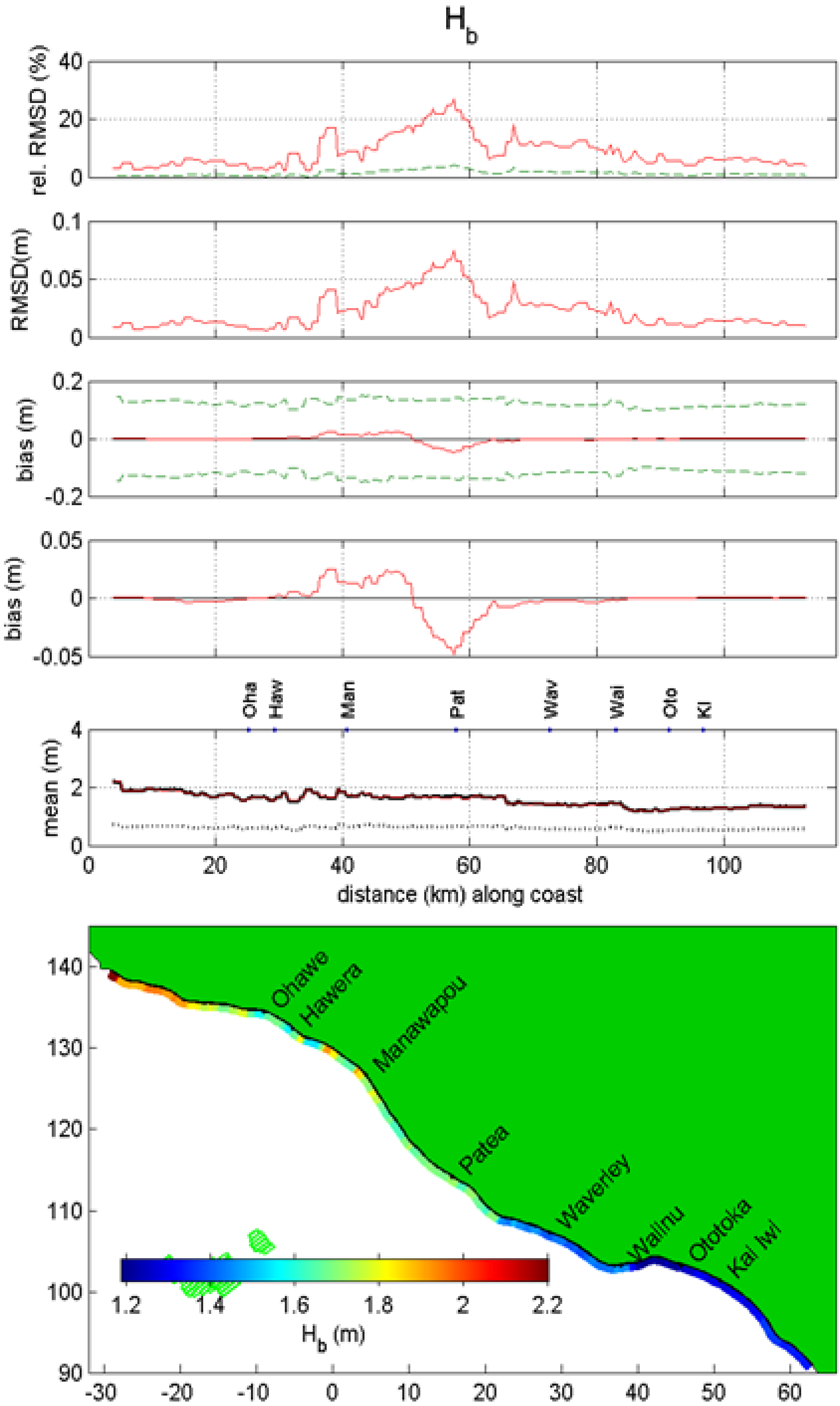

Figure 5-26: Breaking wave height H_b at the coast. The mean value (over a 12 month period) from the baseline simulation is shown by the colour-scaled ribbon in the bottom panel, and as a solid black line in the panel above, compared with the mean value from the case 1 simulation (red), and the standard deviation (SDh) from the baseline simulation (dashed black line). In the two panels above that, the mean difference (bias = case 1 - baseline) between the two simulations is shown, plotted on its own and also plotted along with green dashed lines showing plus and minus half the baseline standard deviation (SDm). The top two panels show the root-mean-square difference (RMSD) between the two simulations, in absolute value (metres) and as a fraction of the baseline standard deviation (SDm) (red line) and mean magnitude (dashed green line).

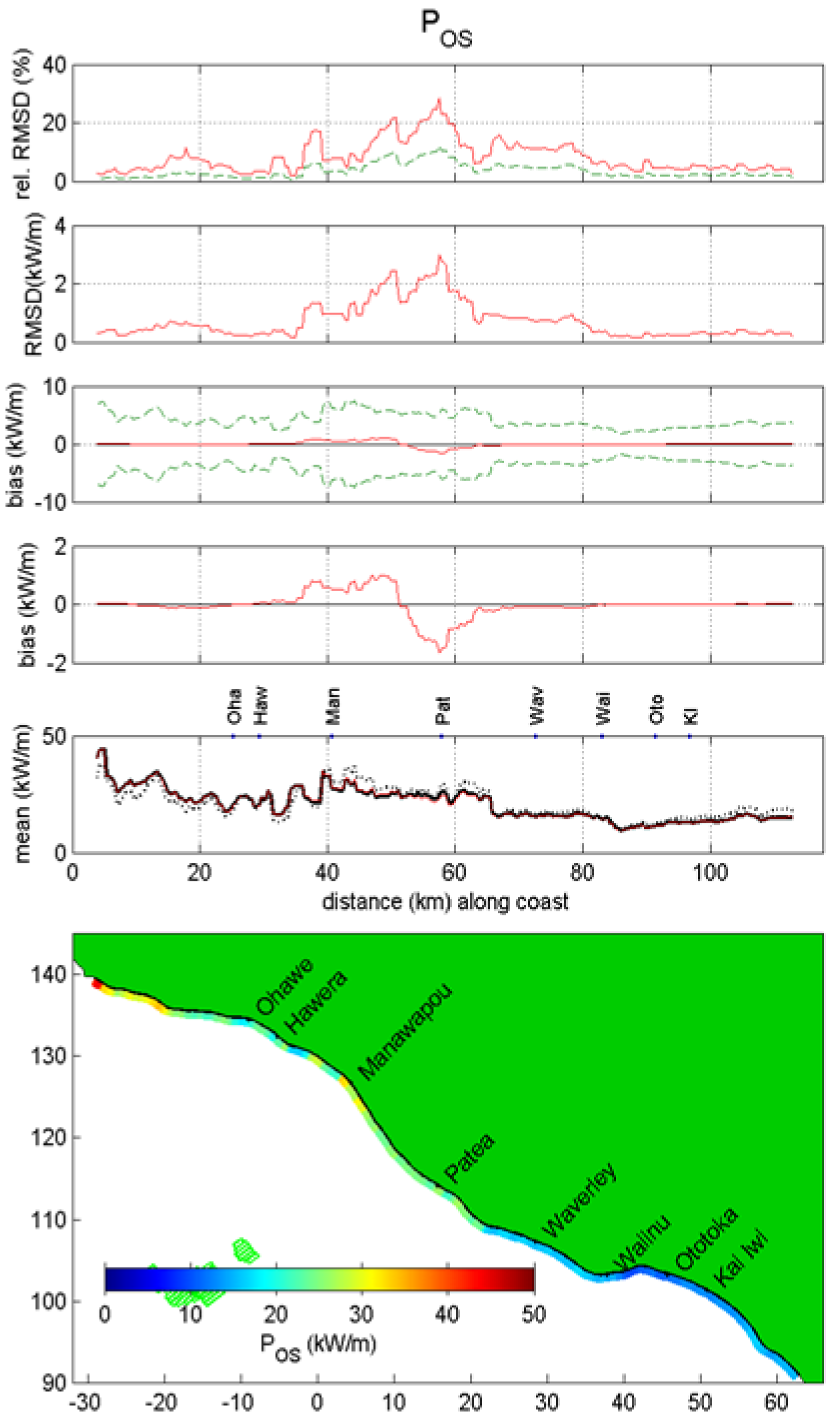

Figure 5-27: Net onshore flux factor P_{os} at the coast. The mean value (over a 12 month period) from the baseline simulation is shown by the colour-scaled ribbon in the bottom panel, and as a solid black line in the panel above, compared with the mean value from the case 1 simulation (red), and the standard deviation (SDh) from the baseline simulation (dashed black line). In the two panels above that, the mean difference (bias = case 1 - baseline) between the two simulations is shown, plotted on its own and also plotted along with green dashed lines showing plus and minus half the baseline standard deviation (SDm). The top two panels show the root-mean-square difference (RMSD) between the two simulations, in absolute value (kW/m) and as a fraction of the baseline standard deviation (SDm) (red line) and mean magnitude (dashed green line).

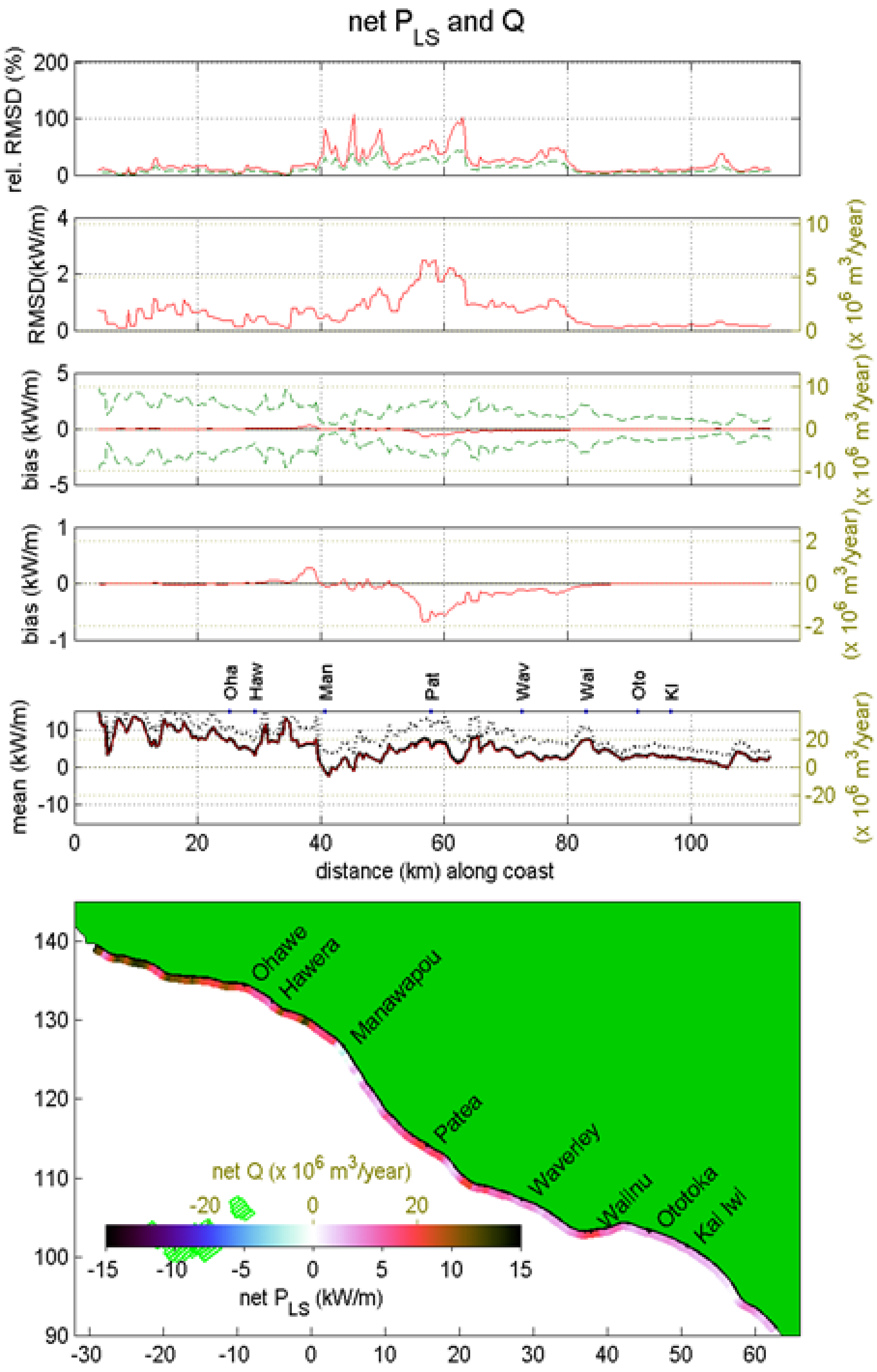

Figure 5-28: Net longshore flux factor P_{ls} (black scales) and sediment transport potential Q (gold scales) at the coast. The mean value (over a 12 month period) from the baseline simulation is shown by the colour-scaled ribbon in the bottom panel, and as a solid black line in the panel above, compared with the mean value from the case 1 simulation (red), and the standard deviation (SDh) from the baseline simulation (dashed black line). In the two panels above that, the mean difference (bias = case 1 - baseline) between the two simulations is shown, plotted on its own and also plotted along with green dashed lines showing plus and minus half the baseline standard deviation (SDh). The top two panels show the root-mean-square difference (RMSD) between the two simulations, in absolute value and as a fraction of the baseline standard deviation (SDm) (red line) and mean magnitude (dashed green line) of total P_{ls}.

As P_{ls} and Q can take either positive or negative values, it can in general be instructive to also examine time averages of their magnitudes $|P_{ls}|$ and $|Q|$ (Figure 5-29) and their values restricted to times when it is either positive (Figure 5-30) or negative (Figure 5-31). In this case, however, where P_{ls} is strongly weighted to positive values, the first two quantities have rather similar behaviour to the net statistic. Figure 5-31 does show that the bathymetry modifications would lead to a very small, localised, increase in the magnitude of the relatively rare negative (westward) sediment transport events near Manawapou.

The divergence of the longshore flux factor (P_{ls}) and hence Q (Figure 5-32) is a quantity that can contribute to either erosion or accretion of a beach where the divergence is positive or negative, respectively. The former would be the case, for example, on a section of beach with eastward transport that increases in magnitude with distance eastward along the beach, meaning more sediment is leaving the beach segment through its eastern end than is entering at its westward end. Positive divergence tends to occur around headlands, or other convex segments of coast. On the South Taranaki coast there is considerable spatial and temporal variability in this statistic in the baseline case. The bathymetry modification introduces some biases, at a level generally less than the standard deviation (SDh), which also has high spatial variability.

Waves at the coast can drive mean longshore currents either due to an oblique angle of incidence, or through longshore variability in wave height setting up sea level gradients. The corresponding components $V_{ls,obl}$ and $V_{ls,hgrad}$ of longshore current speed are plotted in Figure 5-33 and Figure 5-34, respectively. Due to the coast's alignment, we can expect oblique wave incidence to drive eastward currents throughout the region, with magnitudes of up to 1 – 2 m/s. Introducing the bathymetry changes could affect this quantity in a similar manner to P_{ls}, with decreases of order 5% of a standard deviation (SDh) in sections of the coast around Patea. The component due to height gradient has a high level of spatial and temporal variability, and could expect to show a highly variable (but relatively small in magnitude) pattern of bathymetry-related changes.

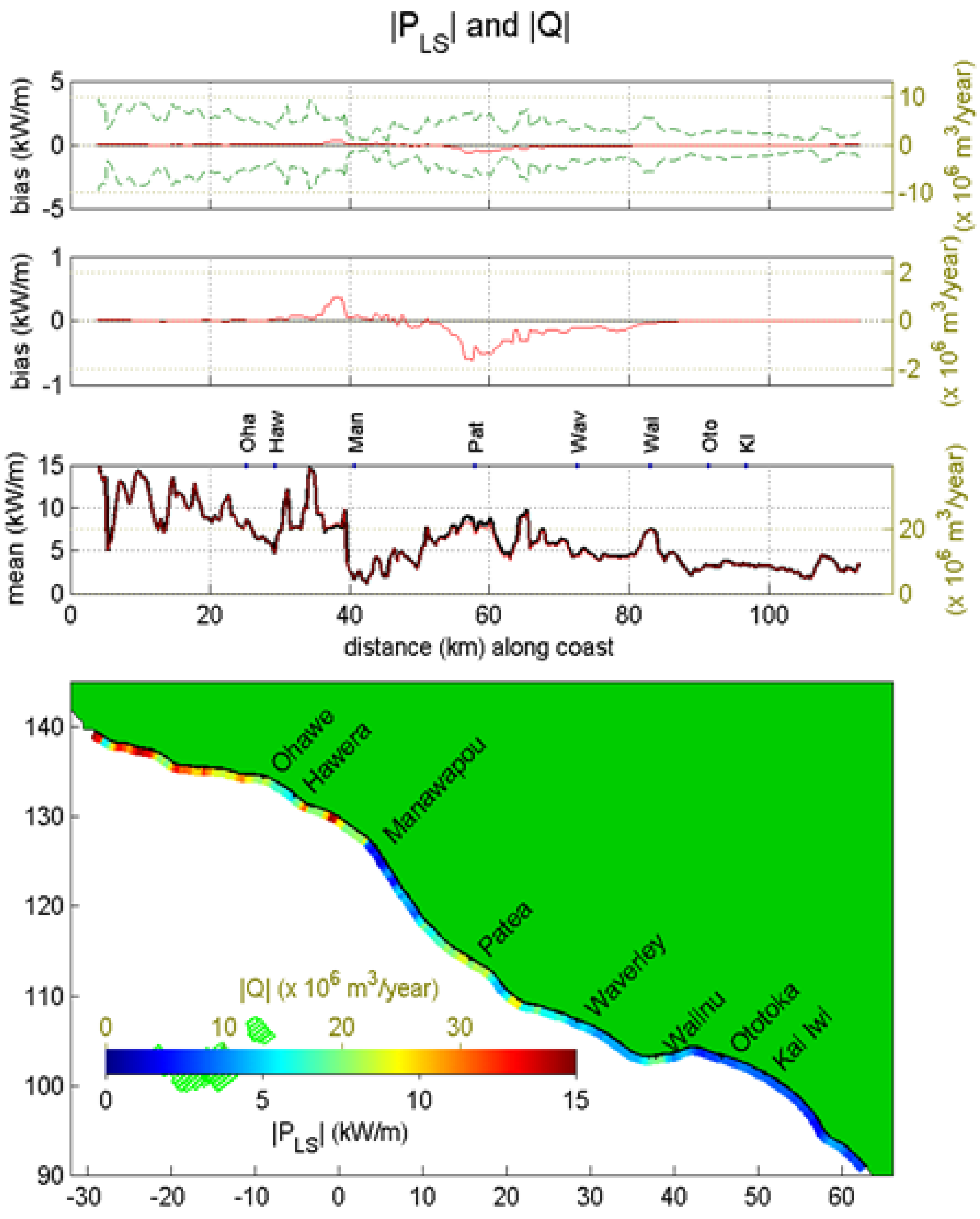

Figure 5-29: Magnitude of the longshore wave energy flux factor P_{ls} (black scales) and sediment transport potential Q (gold scales). The mean value (over a 12 month period) from the baseline simulation is shown by the colour-scaled ribbon in the bottom panel, and as a solid black line in the panel above, compared with the mean value from the case 5 simulation (red), and the standard deviation (SDh) from the baseline simulation (dashed black line). In the two panels above that, the mean difference (bias = case 1 - baseline) between the two simulations is shown, plotted on its own and also plotted along with green dashed lines showing plus and minus half the baseline standard deviation (SDm) of total P_{ls} (or Q).

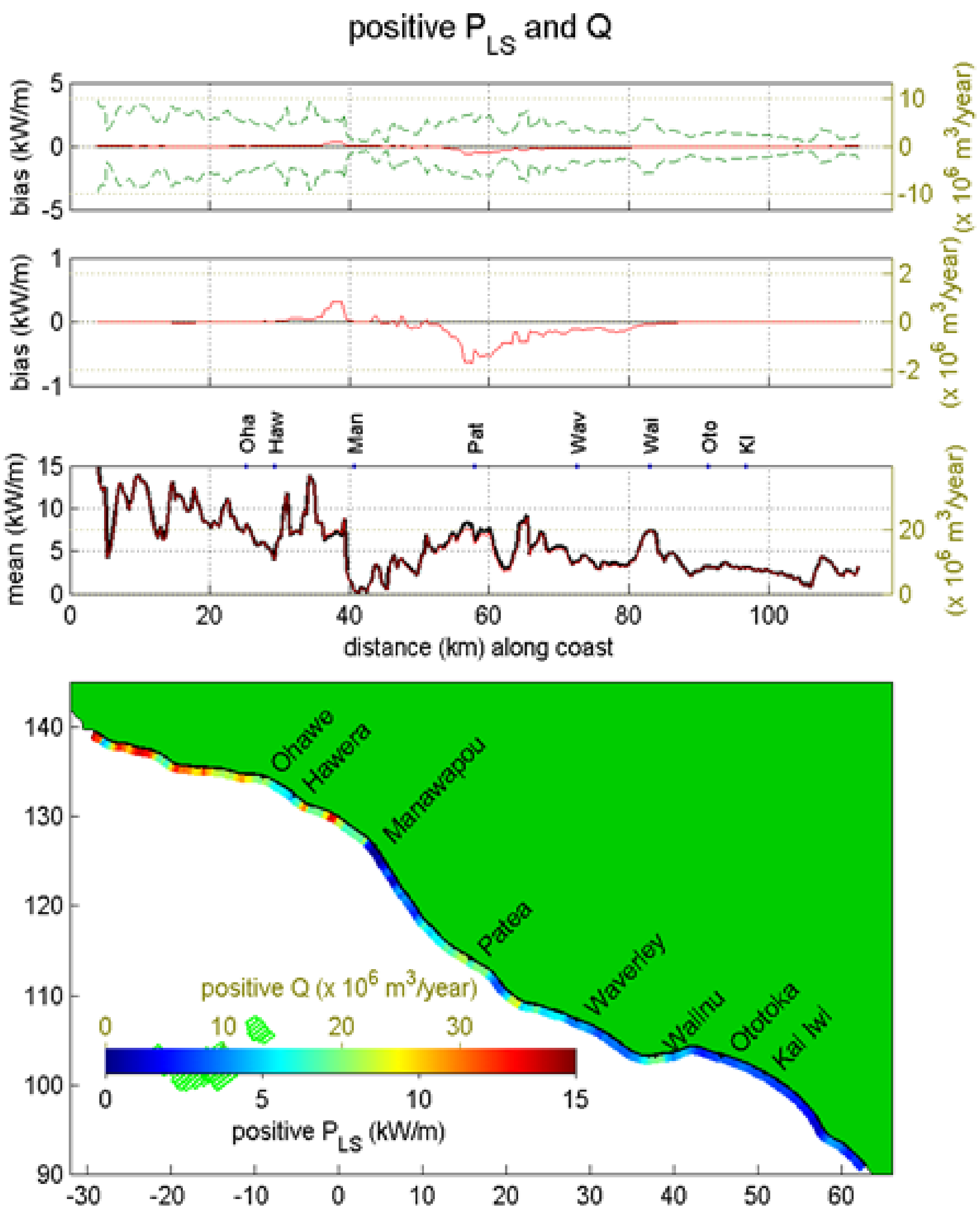

Figure 5-30: Magnitude of the longshore wave energy flux factor P_{ls} (black scales) and sediment transport potential Q (gold scales), averaged over times when they have positive values. The mean value (over a 12 month period) from the baseline simulation is shown by the colour-scaled ribbon in the bottom panel, and as a solid black line in the panel above, compared with the mean value from the case 1 simulation (red), and the standard deviation (SDh) from the baseline simulation (dashed black line). In the two panels above that, the mean difference (bias = case 1 - baseline) between the two simulations is shown, plotted on its own and also (top plot) plotted along with green dashed lines showing plus and minus half the baseline standard deviation (SDm) of total P_{ls} (or Q).

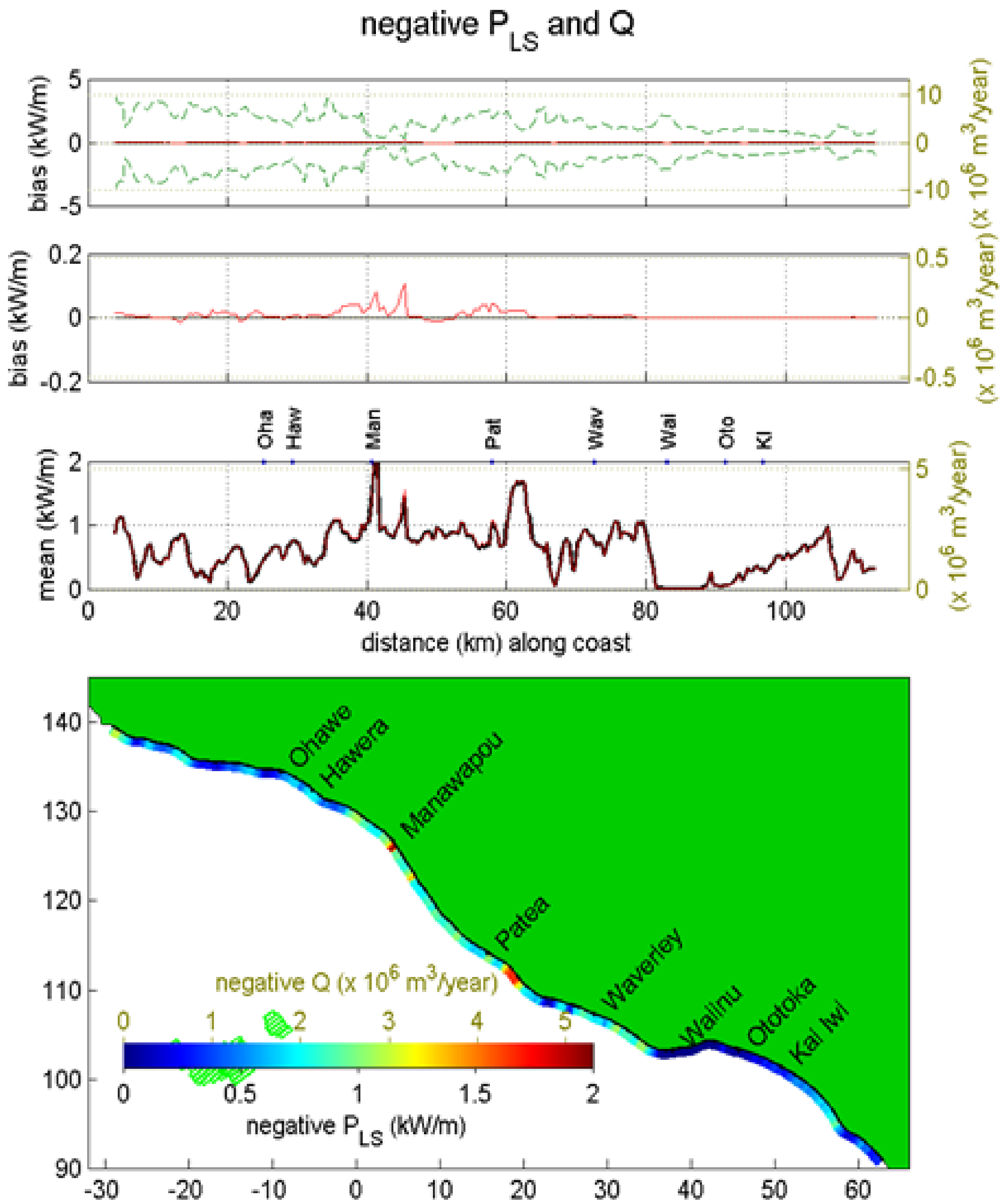

Figure 5-31: Magnitude of the longshore wave energy flux factor P_{ls} (black scales) and sediment transport potential *Q* (gold scales), averaged over times when they have negative values. The mean value (over a 12 month period) from the baseline simulation is shown by the colour-scaled ribbon in the bottom panel, and as a solid black line in the panel above, compared with the mean value from the case 1 simulation (red), and the standard deviation (SDh) from the baseline simulation (dashed black line). In the two panels above that, the mean difference (bias = case 1 - baseline) between the two simulations is shown, plotted on its own and also plotted along with green dashed lines showing plus and minus half the baseline standard deviation (SDm) of total P_{ls} (or *Q*).

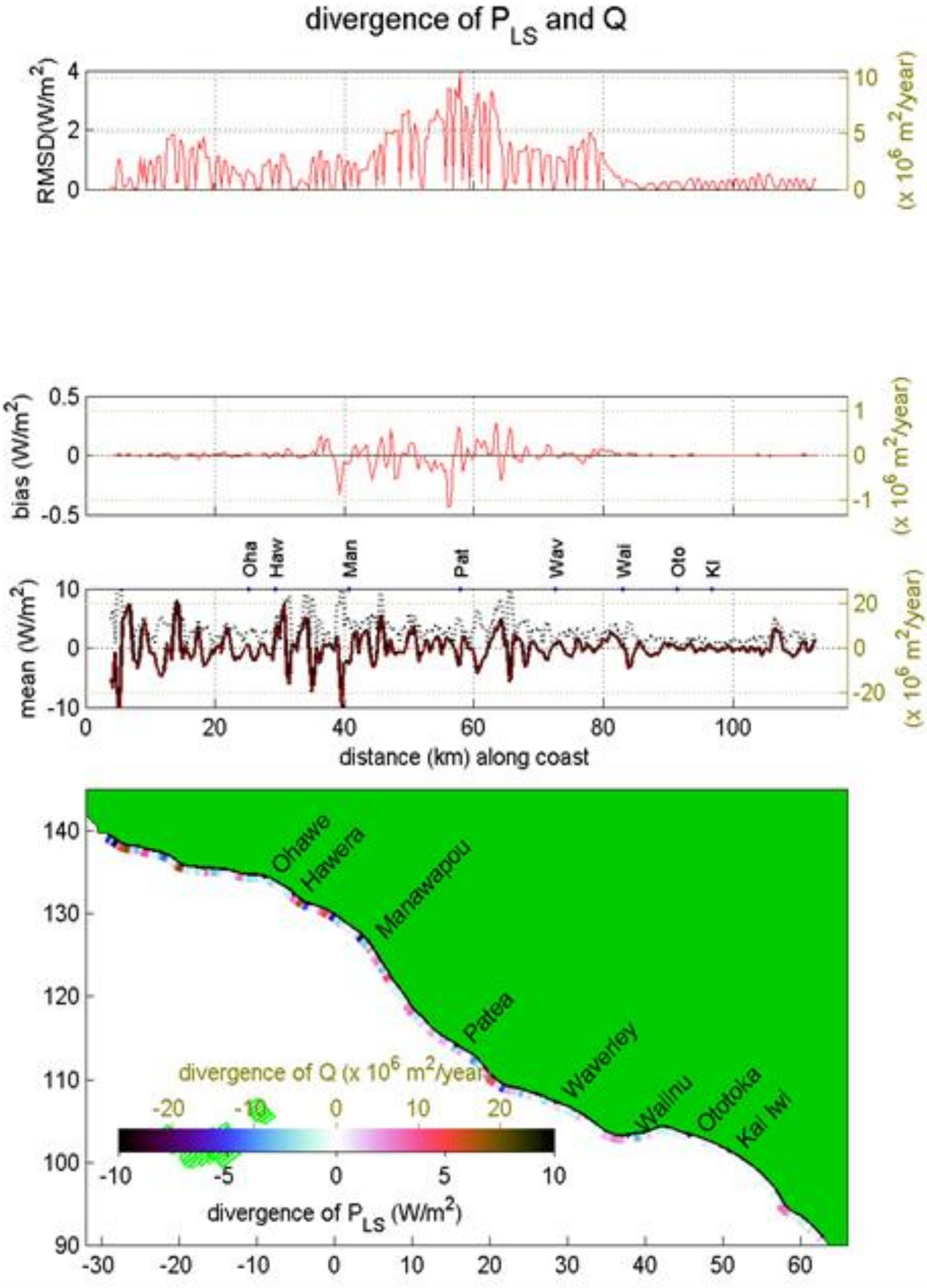

Figure 5-32: Divergence of the longshore wave energy flux factor P_{ls} (black scales) and sediment transport potential *Q* (gold scales). The mean value (over a 12 month period) from the baseline simulation is shown by the colour-scaled ribbon in the bottom panel, and as a solid black line in the panel above, compared with the mean value from the case 1 simulation (red), and the standard deviation (SDh) from the baseline simulation (dashed black line). In the panels above that, the mean difference (bias = case 1 - baseline) and the root-mean-square difference (RMSD) between the two simulations is shown.

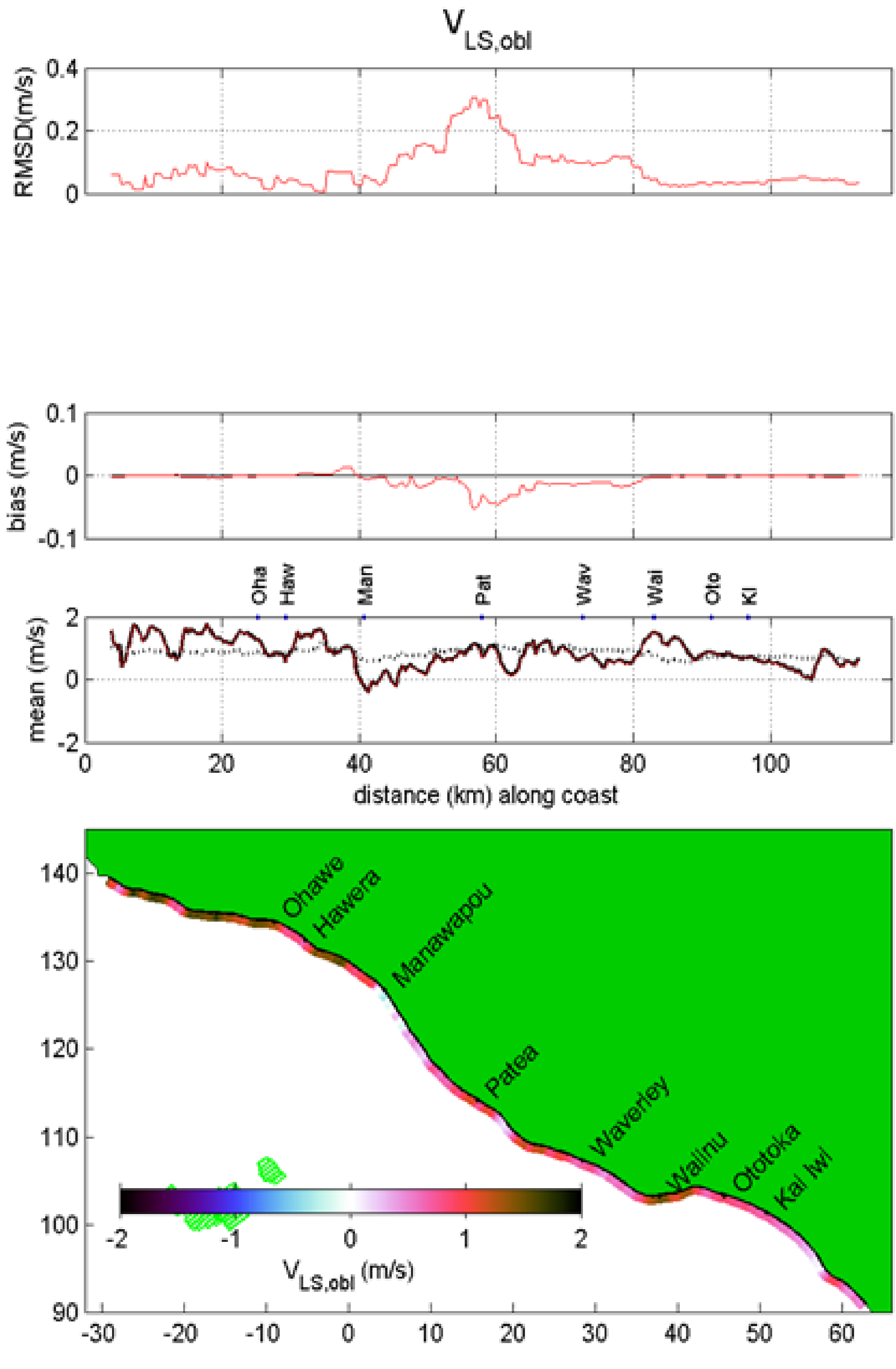

Figure 5-33: Component of longshore mean current associated with oblique wave incidence $V_{ls,obl}$. The mean value (over a 12 month period) from the baseline simulation is shown by the colour-scaled ribbon in the bottom panel, and as a solid black line in the panel above, compared with the mean value from the case 1 simulation (red), and the standard deviation (SDh) from the baseline simulation (dashed black line). In the panels above that, the mean difference (bias = case 1 - baseline) and the root-mean-square difference (RMSD) between the two simulations is shown, in absolute value (m/s).

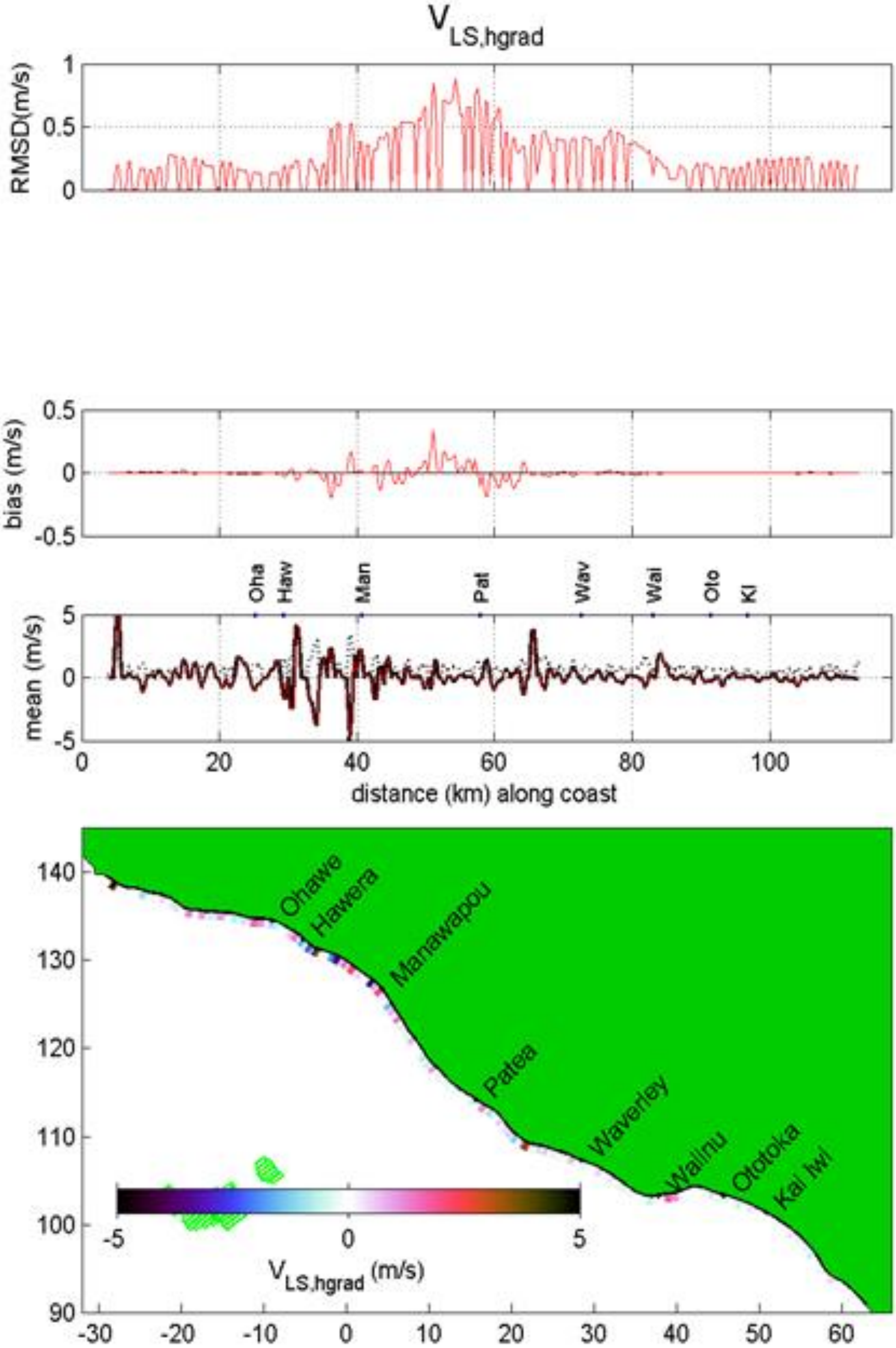

Figure 5-34: Component of longshore mean current associated with wave height gradient $V_{ls,hgrad}$. The mean value (over a 12 month period) from the baseline simulation is shown by the colour-scaled ribbon in the bottom panel, and as a solid black line in the panel above, compared with the mean value from the case 1 simulation (red), and the standard deviation (SDh) from the baseline simulation (dashed black line). In the panels above that, the mean difference (bias = case 1 - baseline) and the root-mean-square difference (RMSD) between the two simulations is shown, in absolute value (m/s).

6 The fate of sand extraction pits and mounds

The planned sand extraction operations in the South Taranaki Bight will result in changes in seabed morphology that will take the form of elongated "lanes" about 1 m deep, with mounds <9 m tall and pits to 10 m deep at different ends of the lanes. The exact configuration of the cut and fill will depend on the mining plan adopted.

The key question addressed in this section of the report is this: what will be the fate of the pits and mounds over time?

We address this question by firstly reviewing conceptual expectations and the behaviour of pits and mounds. We then briefly review various approaches used to predict mound and pit evolution. Finally, we describe the methods used in this study and give the results.

A list of symbols is provided in the Appendix.

6.1 The concept of stability

We can think of a seabed as being stable, or in equilibrium, over some long, but not too long, timescale. That timescale lies between the timescale associated with the tides and waves that disturb the seabed on regular and semi-regular occasions (days, weeks, months) and the timescale that is associated with fluctuations in large-scale external forcings such as sea-level rise or change in storminess (decades and longer). Seabeds are not typically flat; instead, they are usually moulded into rhythmic undulations of various length scales (ripples, megaripples, sand ridges and the like). "Equilibrium" and "stability" are not meant to imply that such features are static and unchanging – indeed, individual features may constantly accrete, erode and migrate. However, over the equilibrium timescale, the characteristics of the field of rhythmic undulations as a whole, as expressed by the average height, spacing and crest length, for instance, remain the same. This is what is meant by "stability" or "equilibrium". We can now think of a pit/mound as a perturbation to the equilibrium seabed, in that the pit/mound represents a feature with a depth/height, length, width and plan shape that is not normally a part of the suite of undulations or rhythmic features that compose the seabed. The question then becomes: what happens to that perturbation over time?

In general, there might be two divergent pathways. On the one hand, the perturbation might radiate downstream (or upstream for that matter) leading, over time, to the establishment of an entirely new equilibrium shape to the seafloor. For instance, if the pre-perturbation seafloor were perfectly flat, then a pit might result in bedforms radiating outwards until a new equilibrium seafloor covered in bedforms is established. This represents a change in state of the system. On the other hand, the perturbation might be damped, and the seafloor returns, over time, to its pre-perturbation configuration.

6.2 Pits

A complex suite of processes can be triggered by a pit dredged in the seabed, and these affect pit behaviour and ultimate fate in a variety of ways.

As currents encounter the leading edge of the pit they will decelerate because of the greater water depth, and the sediment-transporting capacity of the flow will decrease as a result. Particles moving as bedload or in saltation will largely be deposited in the pit, and a certain amount of the suspended-sediment load will also be captured. Deposition will occur mainly on the upstream pit slopes and in middle sections of the pit. If the pit is steep-sided, then the flow may separate at the leading edge of the pit under an adverse pressure gradient, causing turbulence that reduces sediment deposition on the upstream slope and/or displaces the deposition zone further into the middle of the pit. If separation is not so intense then deposition may be enhanced on the upstream pit slope under the more gentle backwater flow. At the trailing edge of the pit the flow will converge and accelerate up the downstream slope of the pit, causing erosion. With deposition at one end of the pit and erosion at the other, the pit may elongate or migrate downstream. Generally, the balance between, on the one hand, deposition on the upstream slope and in the middle reaches of the pit and, on the other hand, erosion of the downstream slope, will determine the rate of pit infilling, elongation and migration. Other factors come into play, too. For instance, when sediment particles on a slope are set into motion by waves and currents, the resulting movement will have a component in the downslope direction due to the action of gravity. This will cause the pit to fill with sediment and the side slopes to reduce.

Waves may have a variety of effects. For example, saltation is a common mode of transport in shelf water depths where the sediment has a settling speed that is commensurate with the magnitude of the vertical turbulent flow fluctuations. In this case, individual grains “hop” along the seabed (they are not in such continuous contact with the bed that it can be called bedload transport; and they are not supported enough by the flow turbulence that it can be called suspended transport). Upon encountering a hole in which the bottom-wave-orbital motions are much smaller than the bottom-wave-orbital motions that are causing saltation on the surrounding seabed, a saltating grain may be trapped inside the hole. Over time, capture of saltating grains in this way will cause the pit to fill. Waves more generally are thought of as adding to the bed shear stress exerted by currents and to the transport of sediments caused by currents. Hence, in a very general sense, waves will enhance and accelerate the infilling, deformation and migration of a pit that would otherwise occur if there were only currents present.

The particular processes that come into play in any given situation will depend on the pit dimensions, shape and orientation relative to the local currents and waves; the material that composes the seabed; the surrounding seabed topography; the local currents; and the wave climate. Where currents are dominant (over waves), the orientation of the pit relative to the principal axis of the current is an important factor. For instance, van Rijn et al. (2005) noted that when the pit is oriented parallel to the local current, currents in the pit may increase considerably due to the decrease of bottom friction, but when the pit is oriented perpendicular to the local current, currents in the pit are reduced due to the increased water depth.

6.2.1 Process-based models

Numerical process-based morphodynamic models have been used to investigate the response of the seabed to perturbations on the scale of dredged pits. The key characteristic of the morphodynamic model is that the flow is coupled to the morphology, which allows the two to interact over time in the simulation: in essence, as the morphology evolves it causes changes to the flow field, which in turn affect the evolution of the morphology. Idier et al. (2010) identified three morphodynamic modelling approaches for studying the effects of offshore aggregate extraction.

1. Full process-based models, with flows coupled to the bed. There are many different approaches within this class, with different assumptions and approximations used to simplify the governing equations; “morphologic factors” of some kind are typically used to extend the model timestep and reduce model run time.

2. Idealised process-based models, which do not fully resolve processes. An example is stability analysis, which seeks to identify whether perturbations in the seabed grow or decay and, if they do grow, what the preferred wavelengths and associated timescales will be.

3. Conceptual or “behaviour-oriented” models, which have not yet been commonly used.

Idier et al. concluded that “none of the models have been validated, to provide reliable predictions of the impact of large-scale mining, on the morphodynamic stability of the region. However, the different approaches complement each other, supplying the end-user with a range of ‘tools’ for investigating the impact. As validation over [long] periods of interest is not yet possible, the only way to obtain a reliable insight into the future impacts is to combine the different modelling approaches and, concurrently, deal with the uncertainty of the forecasts”.

Roos and Hulscher (2004) and Roos et al. (2008) used a morphodynamic model to study the evolution of pits that are wide (order kilometres) and shallow (ratio of pit depth to water depth small) in a tide-dominated setting. The model was based on the depth-averaged shallow-water momentum equations, and included wave-stirring and gravitational bed-slope terms. The seabed evolves as a result of the tidally-averaged divergence of the bedload transport. The model showed that the pits cause a flow contraction due to a reduced bottom friction inside the pit, and vorticity is generated over the pit edges. A morphodynamic instability is triggered, which is similar to that associated with the formation of tidal sandbanks. The result is a deepening and deformation of the pit itself and the appearance of adjacent humps, all of which happened over a timescale of centuries. Pit migration was found to depend on flow conditions and not pit geometry, and pit migration was found to occur in the direction of the residual sediment transport (which in turn was controlled by the tidal asymmetry, in this case). Stronger wave activity led to higher migration rates, but migration still required a residual sediment transport. Based on the results of the morphodynamic modelling, Roos et al. (2008) developed a semi-analytical tool for studying the effects on pit infilling and migration of varying design parameters such as pit length, width and orientation with respect to the tidal current. They demonstrated that, amongst other things, smaller and wider pits tend to fill in, but larger and elongated pits tend to erode and deepen at their centres.

van Rijn et al. (2005) summarised as follows the morphodynamic effects of extraction pits as revealed by a range of modelling studies conducted in the USA, UK, Canada and the Netherlands:

> “… the cross-shore morphological changes are relatively small for pits seaward of the 15 m depth contour; the migration rates are mainly affected by the local water depth and not by the pit dimensions (depth, width, length). The migration velocity of the pit in longshore direction was found to be 10 to 15 m/year. The morphological changes remain within the local surrounding of the pits. On the time scale of 100 years the overall longshore migration of the pit is of the order of 1 to 2 km. The sedimentation of the pit (infilling rate) increases strongly with decreasing water depth outside the pit.”

> "The presence of a sand pit results in the formation of circulation cells which may trigger the development of a sandbank pattern (based on stability analysis studies). As time evolves, the sand bank pattern spreads out and migrates, alternatingly generating trough and crest zones. [In this case the] pit itself deepens and the pattern spreads at a rate of 10 to 100 m/year. The migration rate of the centre of the pit is of the order of 1 to 10 m/year."

van Rijn et al. noted that the "modelling of morphodynamics is not very accurate due to the absence of accurate field data of sand transport processes. In the absence of such data the uncertainty margins are relatively large (up to factor 5)".

Gonzalez et al. (2010) developed what they called a "semi-analytical" morphodynamic model of pits. Bed-level changes were formulated in terms of the continuity equation for sediments, which was reduced to a single differential equation following Ribberink (2004) and Ribberink et al. (2005). Ribberink (2004) and Ribberink et al. (2005) found an analytical solution to the continuity equation so expressed, which consisted of a sinusoidal bed wave associated with the pit that travels with migration velocity V_{bed} and that has an amplitude that decays on the timescale T_{bed}. (In this case, T_{bed} is the time it takes for infilling to reduce the amplitude of the perturbation by a factor of 1/*e*.) Using Bailard's (1981) formulation that splits the total sediment transport into bedload and suspended-load components and which takes into account the combined effect of waves and currents, diffusion induced by the bottom slope, and the lag between the flow and the sediment transport in suspension, Ribberink (2004) developed a series of analytical relationships for V_{bed} and T_{bed}. These relationships, which depend on the relative importance of the waves and currents, are functions of flow parameters, sediment characteristics, sediment transport rate, and the initial geometry of the pit. Ribberink et al. (2005) concluded that "using relatively small calibration factors for the sediment transport (range: 0.5–1) the migration and infill behaviour of the trenches [estimated using the analytical solution to the continuity equation that includes analytical relationships for V_{bed} and T_{bed}] could be well described in a qualitative as well as in a quantitative sense". This conclusion was based on laboratory and field validation tests (Gonzalez et al. 2010).

Gonzalez et al. applied their model to predict the evolution of two pits (35 m and 20 m water depth) off the Spanish Balearic Islands. The simulation period was around one decade, and the model was driven by 3-hourly waves and currents. Amongst other things, the temporal evolution of a nondimensional damping parameter and a nondimensional migration velocity were estimated. These predictions were compared to observations (from pit surveys) and found to compare very favourably, including the average migration distance of the pit, which was the same order of magnitude as that measured in field. They also estimated an average V_{bed} and T_{bed}. For instance, for the pit at 20-m water depth, the average migration velocity V_{bed} was 0.36 m/mo (0.012 m/d) and the decay time T_{bed} was 5164 years, with a recuperation time for 50% and 90% being 5113 years and 5376 years, respectively. The authors noted that these results are the same order of magnitude presented by Boers (2005) and Chesher et al. (2005) for pits in water depths greater than 18 m. A key observation from the model simulations was that waves accelerate the morphodynamic evolution greatly, and step changes in the pit morphology are correlated with storms.

Gonzalez et al. analysed their model to show how pit migration rate and infill time depend on the currents, waves, sediment and pit geometry. Gonzalez et al.'s analysis of pit behaviour, and the design recommendations that follow on from that, are essentially restatements of the behaviour of Ribberink's analytical relationships for V_{bed} and T_{bed}, which underpin Gonzalez et al.'s model.

6.2.2 Engineering approaches

Engineering approaches to solving morphodynamic problems typically employ a range of tools including graphs, tables and simple analytical equations. Such tools may have been derived by laboratory or field experimentation, analysis, or numerical simulations using process-based morphodynamic models.

van Rijn (1986) showed that dredged channel infill rates can be estimated by combining a "trapping efficiency" with estimates of sediment transport rate in a simple continuity equation. van Rijn presented graphs of suspended-sediment trapping efficiency e_s, derived from several hundred numerical simulations, in which the trapping efficiency is presented as a function of the approach current speed and angle, approach depth, approach shear velocity, sediment settling speed, wave height, channel depth, channel width, channel side slopes and bed roughness. For current speeds in the range 0.8 – 1.2 m/s, relative wave height in the range 0 – 0.3, and relative bed roughness in the range 0.02 – 0.06, the error in e_s is in the range ±25%. The wave height relative to the water depth and the bed roughness relative to the water depth were both found to have minor influences on the trapping efficiency.

6.2.3 Observations

The literature contains a variety of observations of the behaviour of dredged pits in coastal and inner shelf waters. van Rijn et al. (2005) provided a summary of infilling rates of existing extraction pits in the coastal waters of the USA, Japan, UK and the Netherlands, which is reproduced in Table 6-1.

Table 6-1: van Rijn et al.'s (2005) summary of observations of infilling rates of existing extraction pits in the coastal waters of the USA, Japan, UK and the Netherlands.

Pit location	Infill characteristics
Pit at foot of beachface (2 to 5 m depth contour).	Infill from beachside and from seaside (annual infill rate is not more than about 3% of initial pit volume; infill rates are between 5 and 15 m^3/m/yr, depending on wave climate; filling time scale is 20 to 30 years).
Pit in upper shoreface zone (5 to 15 m depth contour).	Relatively rapid infill of extraction pit with sediments from landside (beach zone); annual infill rates up to 20% of Initial pit volume in shallow water (filling time scale is 5 to 10 years).
Pit in middle shoreface zone (15 to 25 m depth contour).	Infill of extraction pit mainly from landside with sediments eroded from upper shoreface by near-bed offshore-directed currents during storm events; annual infill rate is about 1% of initial pit volume (filling time scale is 100 years).
Pit in lower shoreface zone (beyond 25 m depth contour).	Minor infill of sand in extraction pit; only during super storms.

6.3 Mounds

de Lange and Healy (1994) proposed three different approaches for assessing the stability of dredge spoil mounds on the inner shelf that are subject to the action of waves and currents.

The first method was based on a now-outdated concept, which we will not discuss further.

The second method uses an equation (Komar 1973; 1975) for the critical wave-orbital motion to initiate sediment transport, converts this into combinations of wave height and wave period that yield the critical orbital motion at the water depth over the mound in question, and then compares those wave heights and periods to the joint wave height–period probability distribution to estimate how frequently the mound is disturbed by waves. Although this method does not estimate the rate of mound deflation, it does give a feel for the likely stability and persistence of the mound. A similar approach could be developed for estimating how often a mound is disturbed by currents or by waves combined with currents.

The third method does calculate the mound deflation rate, which it does by using standard equations to calculate the bedload and suspended-load transport rates from input time series of waves and currents, and deflating the mound at a rate that is equivalent to the volumetric transport rate. This method is based on two assumptions. The first assumption is that there is no upstream source that deposits sediment on the mound at the same time that waves and currents are eroding the mound. Note that this is not the same as assuming that sediments are not impinging on the mound from upstream, just that such sediments are not depositing on the mound. The higher the mound stands above the surrounding seabed, the more likely it is that this assumption will be correct, since both current speeds and wave-orbital speeds (under all but shallow-water waves) increase with elevation above the seabed, which will hinder sediment settling. The second assumption is that the sediment eroded from the mound by the waves and currents does not settle on the mound before being swept over the edge onto the surrounding (lower) seabed. For mounds that are small relative to the tidal excursion and that are exposed to a relatively uniform wave field this assumption will also hold.

6.4 Estimates of pit infilling and mound deflation

6.4.1 Methods

Choice of method

van Rijn's (1986) trapping efficiency method was used to estimate the rate of pit infilling at each of three mean water depths, and de Lange and Healy's (1984) third method was used to estimate the rate of mound deflation also at three water depths. van Rijn's method was chosen because it is an expedient approach that incorporates all the relevant parameters, and is based on extensive simulations with a robust numerical model. de Lange and Healy's approach was chosen because it has a reasonable conceptual basis and can be formulated using the same transport equations that are used in van Rijn's method, which makes the two methods consistent with each other.

Water depths

The water depths were 20 m, 35 m and 50 m. For the calculations, the conditions at sites 6, 7 and 10 in the South Taranaki Bight were taken as representative of the mean water depths 20 m, 35 m and 50 m, respectively (Table 6-2). Sites 6 and 7 are sites where current, wave and suspended-sediment measurements were collected during 2011 and 2012. At site 10, currents and suspended-sediment measurements were collected, not waves. The measurements, and descriptions of the sites, were reported by MacDonald et al. (2012).

Table 6-2: Parameters used in South Taranaki Bight calculations.

h_0	20 m	35 m	50 m
C_{bed}	0.65	0.65	0.65
D (mm)	0.20 (site 6)	0.29 (site 6)	0.35 (site10)
X	0.001 (site 6)	0.02 (site 7)	0.001 (site 6)
Λ	0.145	0.145	0.145
w_{s} (cm/s)	1.98	3.27	4.21
σ (cm)	2 (site 6)	12 (site 7)	2 (site 6)
Waves and currents	Model, site 6	Model, site 7	Model, site 10

Definitions

A “pit” is defined as a hole 300 m wide, 300 m long and 10 m deep. A mound is defined as an accumulation of sediment 300 m wide, 300 m long and 10 m high.

Note that for the purpose of our calculations pit morphology is schematised as a rectangular box with vertical sides. In reality the pit will have sloping sides, the exact nature of which will be determined by the shape of the cut face and subsequent slumping which is dependent on the geomechanical properties of the seabed sediments.

Pits

Figure 6-1 shows a 1-m cross-section of a pit. The pit width is B and its depth below the adjacent undisturbed seabed is d. The mean water depth at the undisturbed seabed is h_0. The x direction is parallel to the width of the pit.

The volumetric rate of suspended-sediment transport impinging on the upstream edge of the pit in the x direction is $q_{\mathrm{s}}\sin\alpha_{\mathrm{s}}$, where q_s applies at the water depth h_0. The units of $q_{\mathrm{s}}\sin\alpha_{\mathrm{s}}$ are volume of sediment per unit time per unit length of the pit normal to x, and q_s is the volumetric suspended-sediment transport rate impinging on the upstream edge of the pit at an angle α_s; q_s has units of volume of sediment per time per unit of width of seabed normal to the direction of transport. Bedload is analogously defined, with $q_{\mathrm{b}}\sin\alpha_{\mathrm{b}}$ the volume/length bedload transport rate impinging at the upstream edge of the pit, and q_{b} also applies at the water depth h_0.

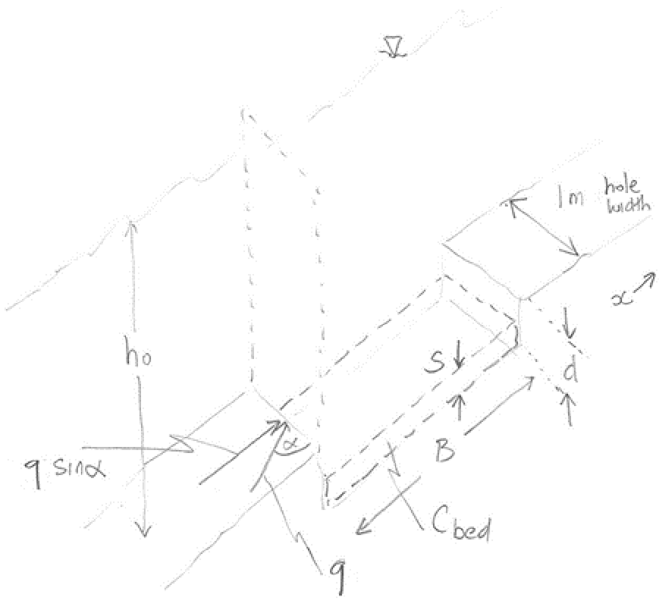

Figure 6-1: Definition sketch: 1-m cross-section of a pit.

Following van Rijn's approach, sediment is assumed to be deposited uniformly in the pit at a rate that equals the transport of sediment into the pit in the x direction multiplied by the trapping efficiency. Hence, over the time interval $\Delta t = (t_i - t_{i-1})$ the volume of sediment deposited in the pit per unit length of the pit is $(e_s q_s \sin\alpha_s + e_b q_b \sin\alpha_{b)} \Delta t$, where e_s is the suspended-sediment trapping efficiency and e_b is the bedload trapping efficiency. Over the same time interval, the change in volume of the pit per unit length of the pit is SB, where S is the sedimentation depth. Assuming C_{bed} is the ratio of the bulk density at which sediment settles in the pit to the mineral density of the suspended-sediment particles then $(e_s q_s \sin\alpha_s + e_b q_b \sin\alpha_{b)} \Delta t = SBC_{bed}$ and:

$$S = (e_s q_s \sin\alpha_s + e_b q_b \sin\alpha_{b)} \Delta t / BC_{bed} \quad (6.1)$$

For all mean water depths (h_0 = 20 m, 35 m and 50 m), C_{bed} was taken as 0.65.

The new pit depth at time t_i is now $d_{i-1} - S$ where d_{i-1} is the depth at time t_{i-1}, and the percentage reduction in pit depth at time t_i relative to the initial pit depth is $\left(1 - \frac{d_{i-1} - S}{d}\right) * 100$. Finally, T_n is the time it takes for d to reduce to $\left(1 - \frac{n}{100}\right) d$, where n is the percentage reduction of the original pit depth.

Mounds

Figure 6-2 shows a 1-m cross-section of a mound. The mound width is B and its height is M. The mean water depth at the undisturbed seabed is h_0; therefore, the mean water depth on the top of the mound is $h_0 - M$. The x direction is parallel to the width of the mound.

The volumetric rate of suspended-sediment transport off the downstream edge of the mound in the x direction is $q_s \sin\alpha_s$, where q_s applies at the water depth $h_0 - M$. The units of $q_s \sin\alpha_s$ are volume of sediment per time per unit length of the mound normal to x. Likewise, $q_b \sin\alpha_b$ is the volume/length bedload transport rate off the downstream edge of the mound, and q_b also applies at the water depth $h_0 - M$.

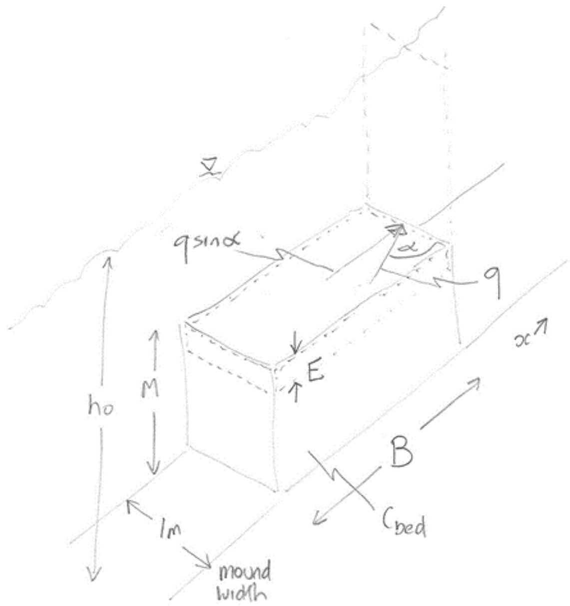

Figure 6-2: Definition sketch: 1-m cross-section of a mound.

Following de Lange and Healy, sediment is assumed to be eroded uniformly from the mound at a rate that balances the transport off the mound in the x direction. Hence, over the time interval $\Delta t = (t_i - t_{i-1})$ the volume of sediment eroded from the mound per unit length of the mound is $(q_\mathrm{s}\sin\alpha_\mathrm{s} + q_\mathrm{b}\sin\alpha_{\mathrm{b})}\Delta t$. Over the same time interval, the change in volume of the mound per unit length of the mound is EB, where E is the erosion depth. Assuming C_bed is the ratio of the density of the mound bed sediment to the density of the suspended-sediment particles then $(q_\mathrm{s}\sin\alpha_\mathrm{s} + q_\mathrm{b}\sin\alpha_{\mathrm{b})}\Delta t = EBC_\mathrm{bed}$ and:

$$E = (q_\mathrm{s}\sin\alpha_\mathrm{s} + q_\mathrm{b}\sin\alpha_{\mathrm{b})}\Delta t / BC_\mathrm{bed} \tag{6.2}$$

C_bed was taken as 0.65 for the erosion calculations for all mean water depths (h_0 = 20 m, 35 m and 50 m).

The new mound height at time t_i is now $M_{i-1} - E$ where M_{i-1} is the height at time t_{i-1}, and the percentage reduction in mound height at time t_i relative to the initial mound height is $\left(1 - \frac{M_{i-1} - E}{M}\right) * 100$. Finally, T_n is the time it takes for M to reduce to $\left(1 - \frac{n}{100}\right) M$, where n is the percentage reduction of the original mound height.

Determination of bedload sediment transport rates

Following Soulsby (1997) the two orthogonal components Φ_x and Φ_y of the dimensionless bedload sediment transport rate Φ_b under combined waves and currents are given as, for $U_\mathrm{w} > U_\mathrm{w,crit}$:

$$\Phi_{x1} = 12\sqrt{\Theta'_\mathrm{m}}(\Theta'_\mathrm{m} - \Theta'_\mathrm{crit}) \tag{6.3a}$$

$$\Phi_{x2} = 12(0.95 + 0.19\cos 2\psi)\sqrt{\Theta'_\mathrm{o}}\Theta'_\mathrm{m} \tag{6.3b}$$

$$\Phi_x = \mathrm{MAX}[\Phi_{x1}, \Phi_{x2}] \tag{6.3c}$$

and

$$\Phi_y = \frac{12(0.19\Theta'_{\mathrm{m}}\Theta_{\mathrm{o}}'^{2}\sin2\psi)}{\Theta_{\mathrm{o}}'^{3/2}+1.5\Theta_{\mathrm{m}}'^{3/2}} \tag{6.4}$$

and for $U_{\mathrm{w}} < U_{\mathrm{w,crit}}$, $\Phi_x = \Phi_y = 0$. Here, Φ_x is the component of Φ_{b} in the direction of the current, Φ_y is the component of Φ_{b} at right angles to direction of the current, ψ is the acute angle between the wave and the current, Θ'_{m} is the mean value of the dimensionless skin friction over the wave cycle, Θ'_0 is the amplitude of the oscillatory component of the nondimensional skin friction, Θ'_{crit} is the critical nondimensional skin friction for initiation of sediment motion, U_{w} is the wave-orbital speed at the bed, and $U_{\mathrm{w,crit}}$ is the critical wave-orbital speed for initiation of sediment motion.

The volumetric bedload transport rate q_{b} (volume of sediment transported as bedload per time and unit width of seabed normal to transport direction) is related to the dimensionless bedload transport as:

$$q_{\mathrm{b}} = \Phi_{\mathrm{b}}\left[\frac{(\rho_{\mathrm{s}}-\rho)}{\rho}gD^3\right]^{0.5} \tag{6.5}$$

where ρ is the fluid density (1025 kg/m^3), ρ_{s} is the sediment density (2650 kg/m^3), g is acceleration due to gravity (9.8 m/s^2), and D is the sediment grainsize.

For the South Taranaki Bight calculations, the mean sediment grainsize at site 6 of 0.20 mm was applied at $h_0 = 20$ m; the mean sediment grainsize at site 7 of 0.29 mm was applied at $h_0 = 35$ m, and the mean sediment grainsize at site 10 of 0.35 mm was applied at $h_0 = 50$ m (Table 6-2). Also, Θ'_0 was equated to the dimensionless wave-induced skin friction θ'_{w}:

$$\theta'_{\mathrm{w}} = \frac{\tau'_{\mathrm{w}}}{(\rho_{\mathrm{s}}-\rho)gD} \tag{6.6}$$

where τ'_{w} is the wave-induced skin friction, which has units of force per unit area of seabed, and which was estimated following Nielsen (1992) as:

$$\tau'_{\mathrm{w}} = 0.5\rho f'_{\mathrm{w}}U_{\mathrm{w}}^2 \tag{6.7}$$

where f'_{w} is the skin-friction wave friction factor, given by:

$$f'_{\mathrm{w}} = \exp\left[5.213\left(\frac{2.5D}{A_{\mathrm{w}}}\right)^{0.194} - 5.977\right] \tag{6.8}$$

$A_{\mathrm{w}} = U_{\mathrm{w}}T/2\pi$ is the near-bed wave-orbital semi-excursion and T is the wave period. For the South Taranaki Bight calculations, U_{w} was given by linear wave theory:

$$U_{\mathrm{w}} = \frac{\pi H}{T\sinh(k_{\mathrm{w}}h_0)} \tag{6.9}$$

where H is the wave height and k_{w} is the linear-theory wavenumber corresponding to T and h_0.

Soulsby (1997) recommended a wave–current model be used to evaluate Θ'_{m}, which is related to the mean skin friction over the wave cycle, τ'_{m}, as:

$$\theta'_{\mathrm{m}} = \frac{\tau'_{\mathrm{m}}}{(\rho_{\mathrm{s}}-\rho)gD} \tag{6.10}$$

For the South Taranaki Bight calculations, we used Soulsby's (1995) model:

$$\tau'_{\mathrm{m}} = \tau'_{\mathrm{c}}[1 + 1.2\left(\frac{\tau'_{\mathrm{w}}}{\tau'_{\mathrm{c}}+\tau'_{\mathrm{w}}}\right)^{3.2}] \qquad (6.11)$$

where τ'_{c} is the current-induced skin friction that would occur due to the current alone. Using the law-of-the-wall:

$$U'_{*\mathrm{c}} = (\kappa U_z)/\ln(\frac{z}{Z_0}) \qquad (6.12)$$

where κ is von Karman's constant (0.41), U_z is the mean current speed at elevation z above the bed, $U'_{*\mathrm{c}}$ is the current-induced skin-friction friction velocity and Z_0 is the seabed roughness length, which, in the case of a skin friction, is given by:

$$Z_0 = 2.5D/30 \qquad (6.13)$$

$U'_{*\mathrm{c}}$ is related to τ'_{c} by:

$$\tau'_{\mathrm{c}} = \rho U'^{2}_{*\mathrm{c}} \qquad (6.14)$$

For the South Taranaki Bight calculations, Komar and Miller's (1973; 1975) model was used to predict $U_{\mathrm{w,crit}}$, where

$$\frac{\rho U^2_{\mathrm{w,crit}}}{(\rho_{\mathrm{s}}-\rho)gD} = 0.21(\frac{A_{\mathrm{w,crit}}}{D})^{1/2} \qquad (6.15)$$

holds at initiation of motion, and $A_{\mathrm{w,crit}} = U_{\mathrm{w,crit}}T/2\pi$ is the near-bed critical wave-orbital semi-excursion. Green (1999) found that Komar and Miller's model performed well at predicting the onset of sand transport under waves at 7 m and 12 m depth seaward of the surfzone. Figure 6-3 shows the performance of the Komar and Miller model at sites 6 and 7 (MacDonald et al. 2012) in the South Taranaki Bight.

Θ'_{crit} is related to the critical wave-orbital speed for initiation of sediment motion as:

$$\Theta'_{\mathrm{crit}} = \frac{\tau'_{\mathrm{crit}}}{(\rho_{\mathrm{s}}-\rho)gD} \qquad (6.16)$$

where:

$$\tau'_{\mathrm{crit}} = 0.5\rho f'_{\mathrm{w}} U^2_{\mathrm{w,crit}} \qquad (6.17)$$

is the critical skin friction for initiation of sediment motion.

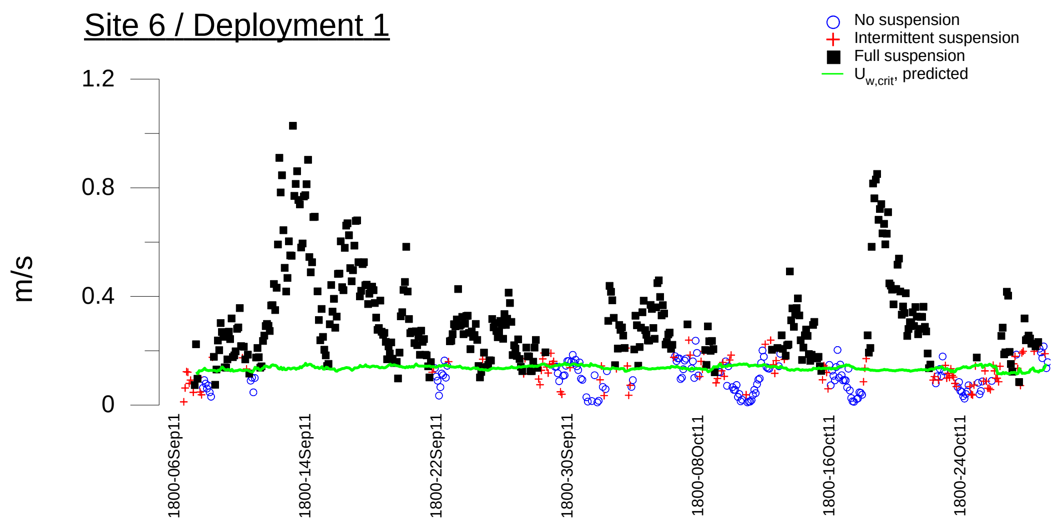

Figure 6-3: Near-bed wave-orbital speed U_{w} classified according to whether sediment was observed to be in full suspension, intermittent suspension or immobile at the time of the measurement. As assessed from acoustic backscatter data (MacDonald et al. 2012). Also shown is $U_{\mathrm{w,crit}}$ predicted by Komar and Miller's (1973; 1975) model. $U_{\mathrm{w,crit}}$ is seen to do a reasonable job at dividing the full-suspension datapoints from the other datapoints. (a) Site 6, deployment 1.

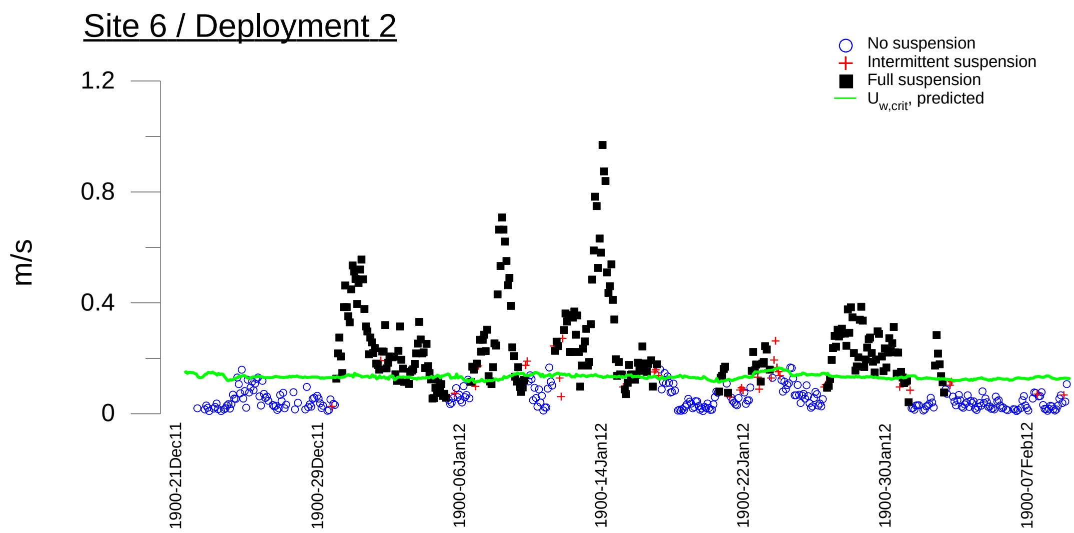

Figure 6.3 (b) Site 6, deployment 2.

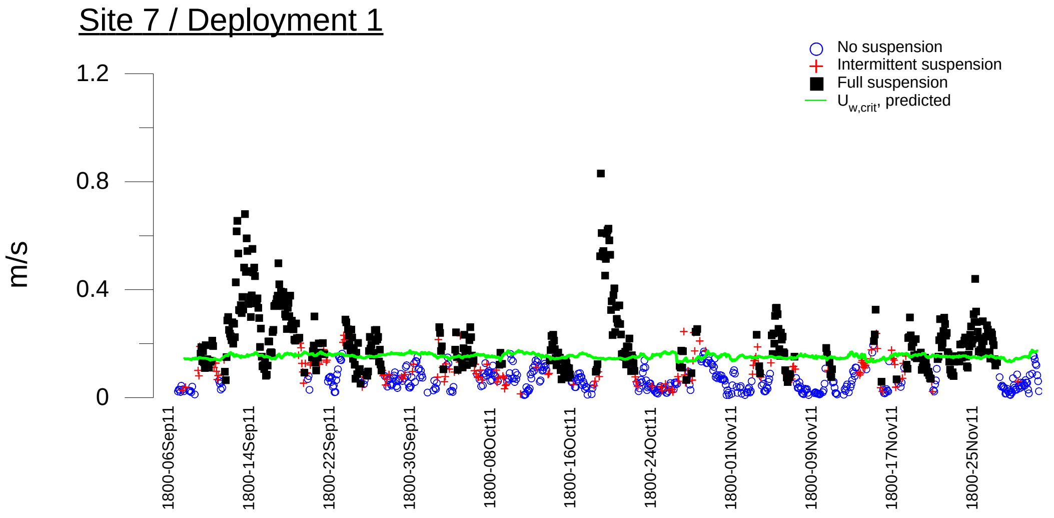

Figure 6.3 (c) Site 7, deployment 1.

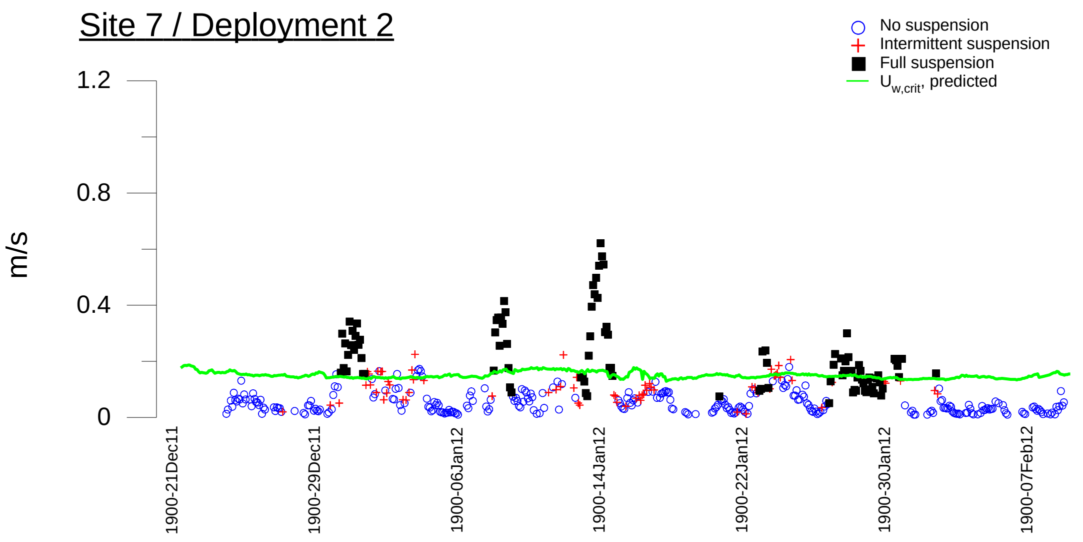

Figure 6.3 (d) Site 7, deployment 2.

Determination of suspended-sediment transport rates

The depth-integrated suspended-sediment transport is given as:

$$q_{\mathrm{s}} = \frac{1}{\rho_{\mathrm{s}}} \int_0^{h_0} U_z C_z \text{ , } U_{\mathrm{w}} > U_{\mathrm{w,crit}} \tag{6.18a}$$

$$q_{\mathrm{s}} = 0 \text{ , } U_{\mathrm{w}} < U_{\mathrm{w,crit}} \tag{6.18b}$$

where C_z is the mean suspended-sediment concentration at elevation z above the bed, and the suspended-load may be assumed to be transported in the direction of the mean current. With C_z expressed as mass/volume, q_s is a volumetric transport rate, with units of volume of sediment transported in suspension per time and unit width of seabed normal to transport direction.

Typically, the suspended-sediment concentration fell below 5 mg/L within 1 m of the bed at sites 6 and 7 in the South Taranaki Bight (MacDonald et al. 2012). Hence, near-bed approximations of the current-speed profile and the suspended-sediment-concentration profile were used in the South Taranaki Bight calculations, and the upper limit of integration in equation (6.12a) was replaced with the elevation above the bed at which C_z fell below 5 mg/L.

Close to the bed, the current-speed profile using the steady-flow law-of-the-wall is:

$$U_{\mathrm{z}} = \frac{U_{*\mathrm{c}}}{\kappa} \ln\left(\frac{z}{Z_0}\right) \tag{6.19}$$

where $U_{*\mathrm{c}}$ is the current-induced friction velocity and Z_0 is the seabed roughness length that reflects the total seabed roughness. Z_0 can be calculated from the drag coefficient $C_{D,\mathrm{z}}$ referenced to U_z using the law-of-the-wall:

$$Z_0 = z / \left[\exp\left(\frac{\kappa}{\sqrt{C_{D,z}}} \right) \right] \tag{6.20}$$

and $U_{*\mathrm{c}}$ is related to U_z as:

$$U_* = (\kappa U_z) / \ln\left(\frac{z}{Z_0}\right) \tag{6.21}$$

For all mean water depths (h_0 = 20 m, 35 m and 50 m), $C_{D,100}$ was taken as 0.0025, which corresponds to Z_0 = 0.0275 cm.

Close to the bed, the suspended-sediment concentration profile assuming a balance between the sediment settling flux and the upward diffusive flux of sediment, with the sediment diffusivity constant with elevation above the bed, is given by:

$$C_z = C_{\mathrm{ref}} \mathrm{e}^{-z/l_{\mathrm{s}}} \tag{6.22}$$

where C_{ref} is the suspended-sediment reference concentration and l_{s} is the suspended-sediment mixing length. Figure 6-4 shows some example near-bed suspended-sediment-concentration profiles from the South Taranaki Bight compared to equation (6.22).

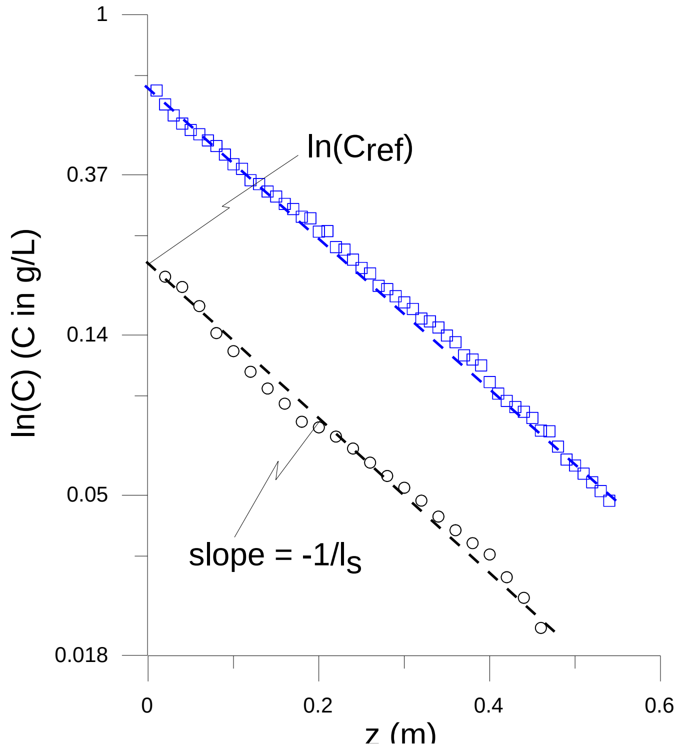

Figure 6-4: Two suspended-sediment concentration profiles. One measured at site 6 (black symbols) and one measured at site 7 (blue symbols), showing the correspondence of the data to the model, equation (6.22) (dashed lines)

For the South Taranaki Bight calculations, C_{ref} was estimated following Nielsen (1992):

$$C_{\mathrm{ref}} = X \rho_{\mathrm{s}} \theta_{\mathrm{w}}'^{3} \tag{6.23}$$

where X is an empirical constant.

Green and Black (1999) verified equation (6.23) using data from two depths on the inner shelf. They found that X = 0.10 for rippled beds and X = 0.005 when there was sheet flow over hummocks. By applying a correction to τ_{w}' to account for flow acceleration above the ripples, the data over both seabed types were found to collapse onto the one curve. C_{ref} in this case was defined as the suspended-sediment concentration in the bottom 1 cm of the water column (in contact with the seabed). Figure 6-5 shows the performance of equation (7.23) at sites 6 and 7 in the South Taranaki Bight, which shows a good fit of model to data, with $X = 0.001$ for site 6 and $X = 0.02$ for site 7. For the calculation of C_{ref} at $h_0 = 20$ m, the site 6 value of X was used, and for the calculation of C_{ref} at $h_0 = 35$ m, the site 7 value of X was used (Table 6-2). Although reference concentration data are available from site 10, there are no wave data. Hence, we cannot use field data to decide on a value of X for $h_0 = 50$ m. However, visual observations by divers and images from towed cameras revealed that the seabed at site 10 (small wave-generated ripples, height approximately 2 cm) was more similar to the seabed at site 6 (wave-generated ripples with height 2 cm and wavelength 70–80 cm) than it was to the seabed at site 7 (near the contact with a rippled scour depression, with ripples 12 cm high and 75 cm wavelength). Given the known dependence of X on bedforms, the site 6 value of X was therefore assumed to apply at site 10, and so the site 6 value of X was used to calculate C_{ref} at $h_0 = 50$ m (Table 6-2).

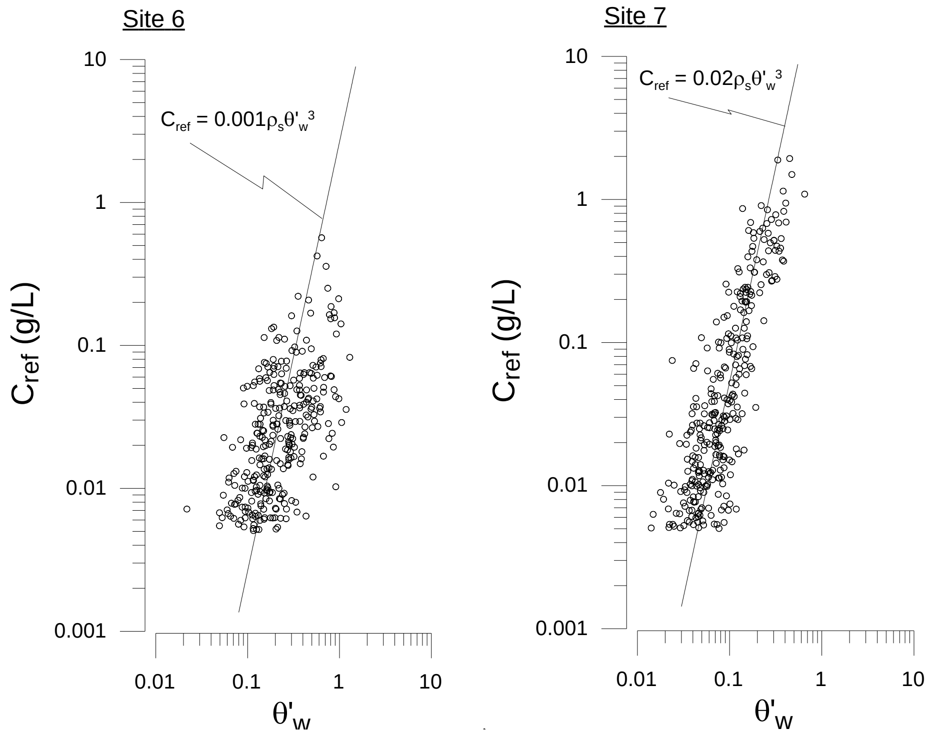

Figure 6-5: Suspended-sediment reference concentration C_{ref} plotted against dimensionless wave-induced skin friction θ'_{w} at site 6 and site 7 in the South Taranaki Bight. C_{ref} is the suspended-sediment concentration in the bottom 1 cm of the water column (in contact with the seabed).

For the South Taranaki Bight calculations, l_{s} was estimated following Nielsen (1992):

$$l_s = \Lambda \frac{A_w \omega}{w_s} \sigma \qquad (6.24)$$

where Λ is an empirical constant, $\omega = 2\pi/T$ is the wave radian frequency, w_{s} is the sediment settling speed and σ is the bedform height. Figure 6-6 shows the performance of equation (6.24) at sites 6 and 7 in the South Taranaki Bight, which yields Λ = 0.145. This value for Λ was used for the South Taranaki Bight calculations (Table 6-2). The sediment settling speed w_{s} at each water depth (h_0 = 20 m, 35 m and 50 m) was predicted from mean grainsize D using Jiminez and Madsen (2003) (Table 6-2). The site 6 ripple height of 2 cm was applied at $h_0 = 20$ m , the site 7 ripple height of 12 cm was applied at $h_0 = 35$ m, and the site 10 ripple height of 2 cm was applied at $h_0 = 50$ m (Table 6-2).

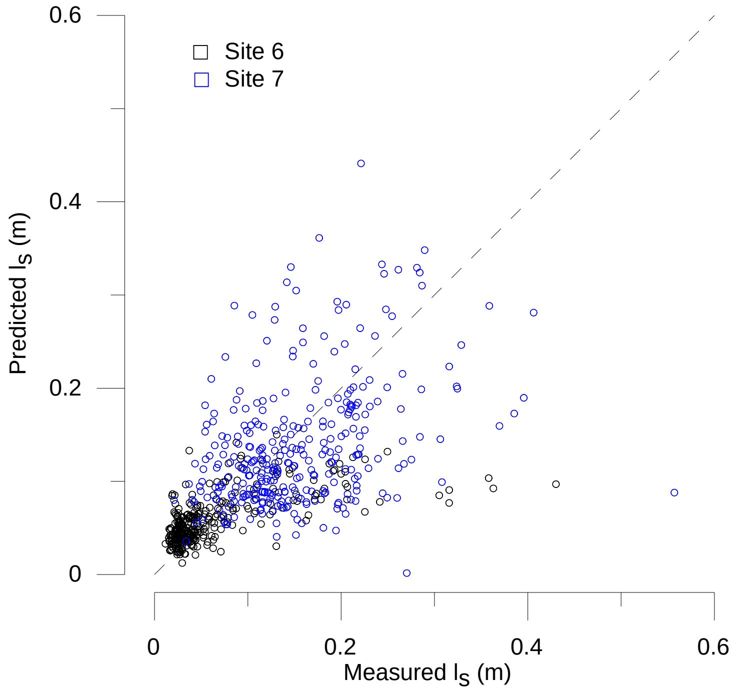

Figure 6-6: Measurements of the suspended-sediment mixing length at sites 6 and 7 in the South Taranaki Bight vs model predictions using equation (6.24) with Λ = 0.145.

6.4.2 Implementation

Predictions of infilling and erosion using the above methods were driven by time series of waves and currents at each of the three mean water depths h_0 = 20 m, 35 m and 50 m.

Input data

The time series of waves and currents for driving the calculations were extracted from the South Taranaki Bight model of waves and currents (Hadfield, 2013) at locations that correspond to the field-measurement sites 6, 7 and 10. The mean water depth h_0 at site 6 was 23 m, at site 7 it was 31 m, and at site 10 it was 42 m. For the infilling/erosion calculations, the site 6 model waves and currents were taken to apply at $h_0 = 20$ m, the site 7 model waves and currents were taken to apply at $h_0 = 35$ m, and the site 10 model waves and currents were taken to apply at $h_0 = 50$ m (Table 6-2). The time series were of significant wave height H, mean spectral period T, mean current speed at 50 cm above the bed U_{50}, and direction of the current (setting to) ψ_c. The model time step Δt was 1 hour, and the model time series length was 3 years. For the infilling/erosion calculations, the model time series were simply repeated and placed to back-to-back to span whatever period was necessary to be able to calculate T_{50} and T_{90}.

Figure 6-7 shows the three-year model time series extracted for site 7, which were applied in the infilling/erosion calculations at $h_0 =$ 35 m. Shown in that graph is the water depth h at $h_0 = 35$ m, which shows tidal variations in water depth around a mean of 35 m. The time series of h was constructed by taking the zero-mean model-predicted water depths at site 7 and adding a 35-m mean depth. Also shown in Figure 6-7 is the time series of U_w for $h_0 =$ 35 m, where U_w was predicted using equation (6.9). Figure 6-7 shows that the model spanned a range of events, including several very large storms in which wave height exceeded 5 m.

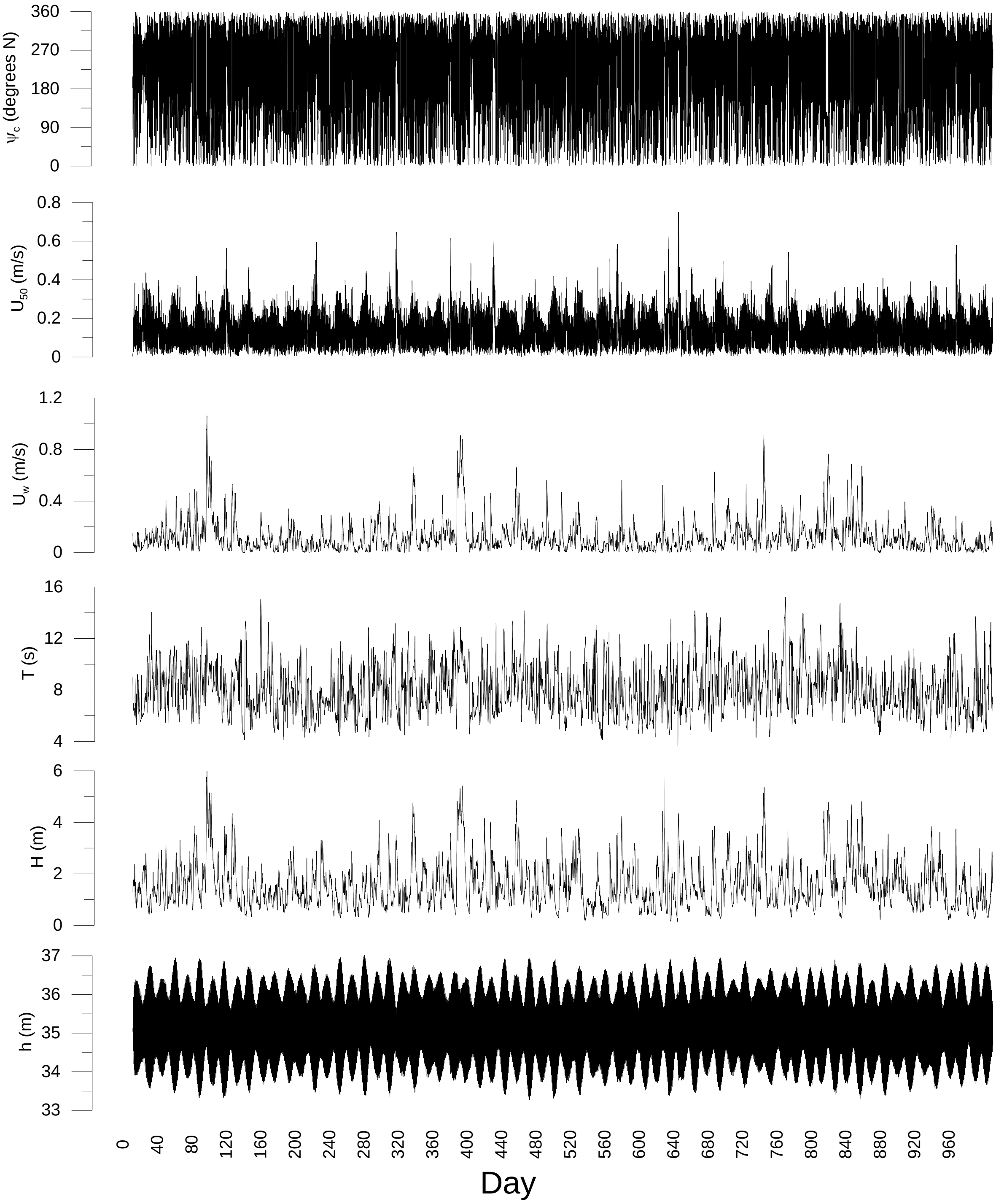

Figure 6-7: Three year time series of waves, currents and water depth. Three-year time series of waves (significant wave height H and mean spectral period T), currents (speed U_{50} and direction ψ_c at 50 cm above the bed) and water depth h extracted from the South Taranaki Bight model at site 7 and applicable at $h_0 = 35$ m.

Transport direction relative to pits and mounds

For the pit infilling, α_{s} and α_{b} were assumed to be 90 degrees, since in this case the pit length (normal to the x direction) is the same as the pit width (parallel to the x direction), which means the pit infills at the same rate regardless of the direction of sediment transport.

Similarly, for the mound erosion, α_{s} and α_{b} were assumed to be 90 degrees, since in this case the mound length (normal to the x direction) is the same as the mound width (parallel to the x direction), which means the mound erodes at the same rate regardless of the direction of sediment transport.

Bedload trapping efficiency

e_{b} was set to 1 following van Rijn et al. (2005), and e_{s} was interpolated from the graphs given in van Rijn (1986). The following describes how we did this.

Suspended-sediment trapping efficiency

van Rijn noted that the graphs of suspended-sediment trapping efficiency are accurate to within $\pm$25% over a range of near-bed current speeds of 0.8 – 1.0 m/s, a range of bed roughness to mean water depth ratio of 0.02 – 0.06, and a range of wave height to water depth ratio of 0 – 0.3. However, van Rijn also noted that the influence of all of these on e_{s} is small. The near-bed current speed in the South Taranaki Bight was typically 0.6 m/s, or higher, when the waves were largest (Figure 6-7), which is just below the lower end of the current-speed range. Assuming the bed roughness is $30Z_0$ and Z_0 = 0.0275 cm, then this gives ratios of bed roughness to mean water depth of 0.00041, 0.00025 and 0.00018 at h_0 = 20 m, 35 m and 50 m, respectively. These values are considerably smaller than the bed roughness to mean water depth range; in this case e_{s} estimated from van Rijn may be an underestimate, which would cause T_{50} and T_{90} to be overestimated. The characteristic wave height in the South Taranaki Bight when waves are actively suspending bed sediments is ~4 m, which gives H/h_0 = 0.20, 0.11 and 0.08 at h_0 = 20 m, 35 m and 50 m, respectively, which is in the range of wave height to water depth.

To demonstrate how e_{s} behaves, Figure 6-8 shows van Rijn's e_{s} as a function of nondimensional pit width B/h_o and the ratio of sediment settling speed w_{s} to bed friction velocity U_{*0} (to be defined, below) for the particular case α_s = 15 degrees and d/h_0 = 0.4. For the South Taranaki Bight, the nondimensional pit widths are 15, 8.6 and 6 for h_0 = 20 m, 35 m and 50 m, respectively, which places the South Taranaki Bight estimates of e_{s} at the extreme left edge of the graph. e_{s} is seen to decrease with a decrease in the ratio w_{s}/U_{*0} and, at the extreme left edge of the graph, e_{s} begins to rapidly decrease towards zero with a decrease in the ratio B/h_o for any given w_{s}/U_{*0}.

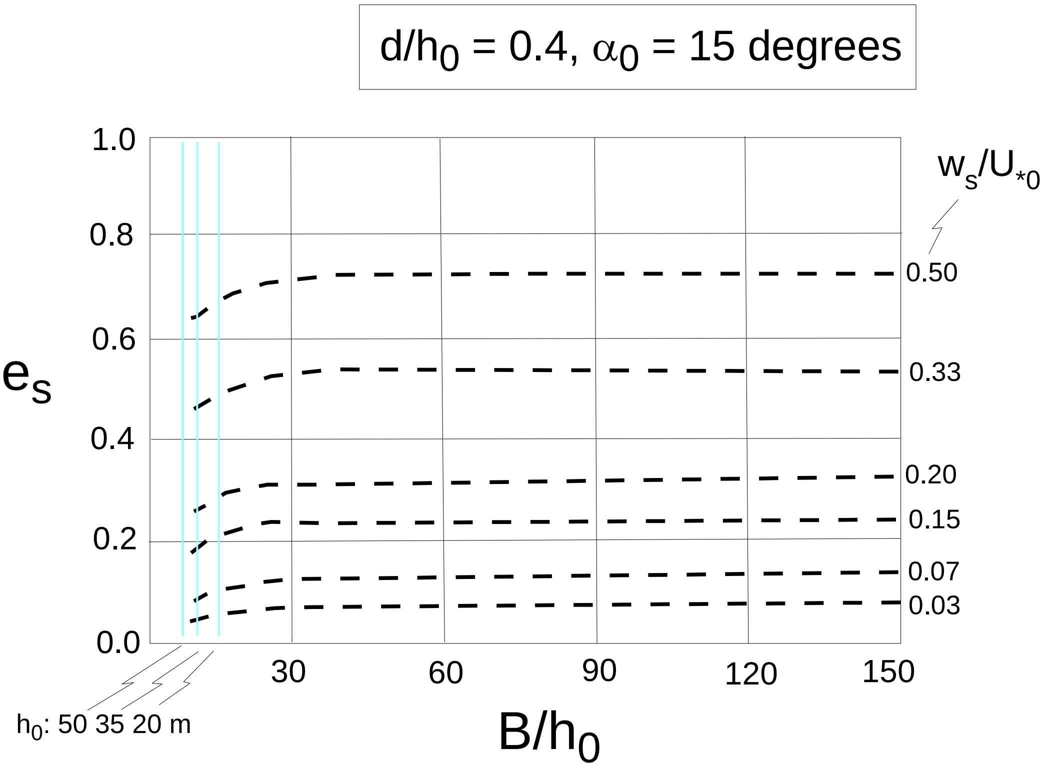

Figure 6-8: van Rijn's e_s as a function of B/h_0 and the ratio of sediment settling speed w_s to bed friction velocity U_{*0} for the case α_s = 15 degrees and d/h_0 = 0.4

The symbols in Figure 6-9 show e_s extracted from van Rijn's graphs for d/h_0 = 0.5, a range of angles (15, 30 and 60 degrees), and the nondimensional pit widths B/h_0 = 15, 8.6 and 6 (which correspond to h_0 = 20 m, 35 m and 50 m, respectively). A curve has been fitted to $e_{\mathrm{s}\,[\mathrm{d}/h_0=0.5,\alpha_\mathrm{s}=60]}$ versus w_s/U_{*0} for each value of B/h_0, where the subscript $[\mathrm{d}/h_0 = 0.5, \alpha_\mathrm{s} = 60]$ indicates that e_s applies at $\mathrm{d}/h_0 = 0.5$ and $\alpha_\mathrm{s} = 60$ degrees. The curves are:

$$e_{\mathrm{s}\,[\mathrm{d}/h_0=0.5,\alpha_\mathrm{s}=60]} = 0.336\ln\left(\frac{w_\mathrm{s}}{U_{*0}}\right) + 0.889,\; B/h_0 = 15\; [h_0 = 20\ \mathrm{m}] \qquad (6.25a)$$

$$e_{\mathrm{s}\,[\mathrm{d}/h_0=0.5,\alpha_\mathrm{s}=60]} = 0.391\ln\left(\frac{w_\mathrm{s}}{U_{*0}}\right) + 0.861,\; B/h_0 = 8.6\; [h_0 = 35\ \mathrm{m}] \qquad (6.25b)$$

$$e_{\mathrm{s}\,[\mathrm{d}/h_0=0.5,\alpha_\mathrm{s}=60]} = 0.440\ln\left(\frac{w_\mathrm{s}}{U_{*0}}\right) + 0.810,\; B/h_0 = 6\; [h_0 = 50\ \mathrm{m}] \qquad (6.25c)$$

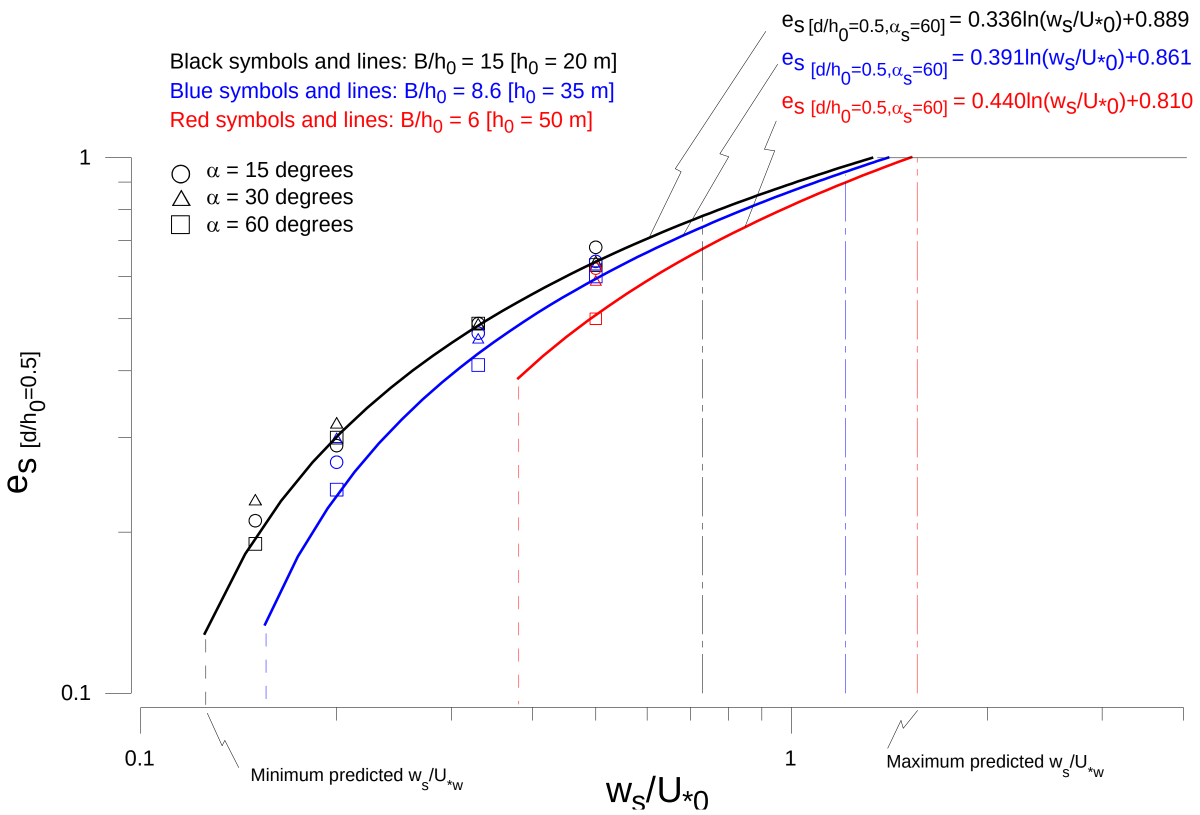

Figure 6-9: The symbols show e_s extracted from van Rijn's graphs for d/h_0 = 0.5, a range of angles (15, 30 and 60 degrees), and the nondimensional pit widths B/h_0 = 15, 8.6 and 6 (which correspond to h_0 = 20 m, 35 m and 50 m, respectively). A curve has been fitted to $e_{s\,[d/h_0=0.5,\alpha_s=60]}$ versus w_s/U_{*0} for each value of B/h_0, where the subscript $[d/h_0 = 0.5, \alpha_s = 60]$ indicates that e_s applies at $d/h_0 = 0.5$ and $\alpha_s = 60$ degrees.

Figure 6-10 plots $e_{s\,[d/h_0,\alpha_s=60]}/e_{s\,[d/h_0=0.5,\alpha_s=60]}$ against d/h_0, which shows how e_s changes with d/h_0. The symbols in Figure 6-10 show $e_{s\,[d/h_0=1.0,\alpha_s=60]}/e_{s\,[d/h_0=0.5,\alpha_s=60]}$ extracted from van Rijn's graphs for the nondimensional pit widths B/h_0 = 15, 8.6 and 6 and w_s/U_{*0} = 0.50, 0.33, 0.20 and 0.15. A single curve has been fitted through those data points and the data point ($e_{s\,[d/h_0=0.5,\alpha_s=60]}/e_{s\,[d/h_0=0.5,\alpha_s=60]}, d/h_0$), and the curve has been extended to the left so that the trapping efficiency tends towards zero as d/h_0 tends towards zero. The equation for the curve is:

$$e_{s\,[d/h_0,\alpha_s=60]}/e_{s\,[d/h_0=0.5,\alpha_s=60]} = 0.231\ln[d/h_0] + 1.16 \tag{6.26}$$

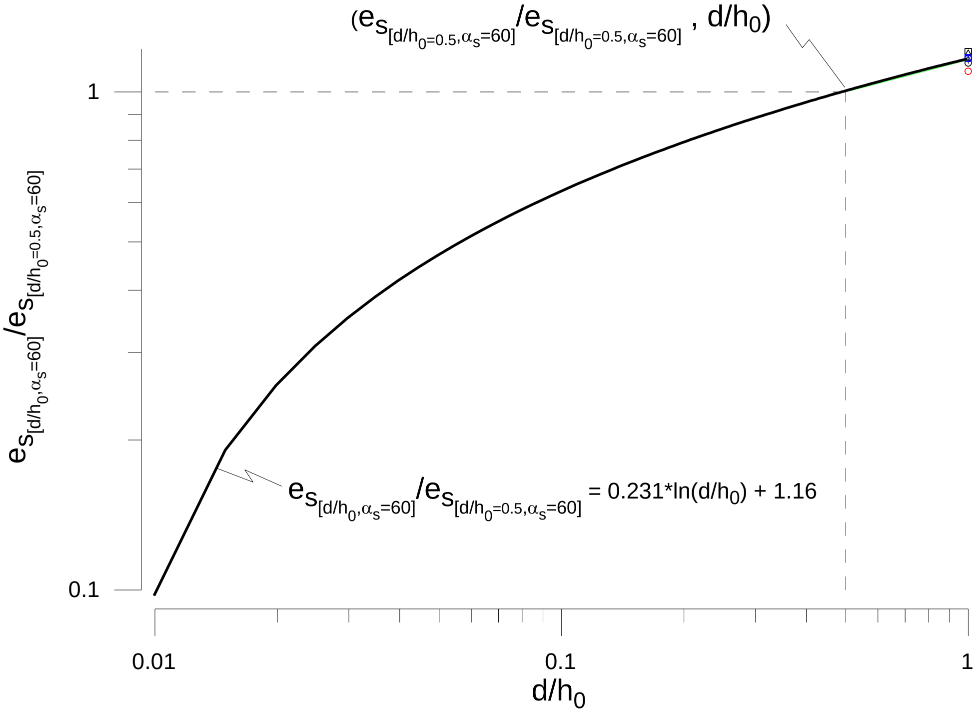

Figure 6-10: Plot of $e_{s\,[d/h_0,\alpha_s=60]}/e_{s\,[d/h_0=0.5,\alpha_s=60]}$ against d/h_0, which shows how e_s changes with change in d/h_0. Refer to the text for a full explanation.

For estimating e_s in the South Taranaki Bight calculations, the following procedure was used.

Firstly, we interpreted the bed friction velocity U_{*0} as the wave-induced friction velocity U_{*w} corresponding to the total seabed roughness k_r (as opposed to the wave-induced skin friction, which is related to the roughness of the individual sediment grains that compose the seabed). In this case:

$$U_{*w} = (0.5 f_w U_w^2)^{1/2} \tag{6.27}$$

where f_w is the wave friction factor that reflects the total seabed roughness, which is given by:

$$f_w = \exp\left[5.213(\frac{k_r}{A_w})^{0.194} - 5.977\right] \tag{6.28}$$

and

$$k_r = 28\sigma^2/\lambda \tag{6.29}$$

where λ is the bedform wavelength. When evaluating e_s, we replaced U_{*0} in the equations for e_s with U_{*w} calculated for the South Taranaki Bight.

Secondly, for any given B/h_0 and w_s/U_{*0} we calculated $e_{s\,[d/h_0=0.5,\alpha_s=60]}$ using equation (6.25). Note that Figure 6-9 shows the maximum and minimum values of w_s/U_{*w} over the simulation at each of the three water depths h_0 = 20 m, 35 m and 50 m in the South Taranaki Bight, which shows that $e_{s\,[d/h_0=0.5,\alpha_s=60]}$ varied between about 0.1 and 0.75 at h_0 = 20 m, 0.1 and 0.9 at h_0 = 35 m, and 0.4 and 1.0 at h_0 = 50 m.

Finally, we converted $e_{s\,[d/h_0=0.5,\alpha_s=60]}$ to e_s at the appropriate d/h_0 using equation (6.26). Note that e_s calculated in this way strictly applies at α_s = 60 degrees. However, for the ranges of B/h_0 and w_s/U_{*0} in the South Taranaki Bight e_s is not particularly sensitive to variations in α_s.

6.4.3 Results

From the predicted time series of infilling and erosion, T_{50} and T_{90} were calculated for the mounds and pits. The results are shown in Table 6-3.

Table 6-3: Predicted T_50 and T_90.

	$h_0 = 20$ m		$h_0 = 35$ m		$h_0 = 50$ m	
	T_{50} (years)	T_{90} (years)	T_{50} (years)	T_{90} (years)	T_{50} (years)	T_{90} (years)
Pit	39	72	54	106	297	533
Mound	9	22	9	20	163	353

The model predicts that at 50-m water depth it will take around 500 years for waves and currents to reduce the pit volume by 90% (around 300 years for 50% reduction). The model predicts that, at the same depth, it will take around 350 years for 90% of the mound to be deflated (150 years for 50% deflation).

Infilling and deflation will be faster at 35-m water depth: 100 years for 90% infilling of the pit (50 years for 50% infilling), and 20 years for 90% deflation of the mound (10 years for 50% deflation).

6.4.4 Discussion

Water depth controls the rate of pit infilling and mound erosion: the smaller the water depth, the greater the wave-orbital speed at the bed for any given wave height and period, and the larger the associated sediment transport. However, at the same time, the suspended-sediment trapping efficiency of the pit varies inversely with w_s/U_{*w} which, to a certain extent, counteracts the increase in sediment transport. This is not the case, however, for the mound deflation, which is not governed by any trapping efficiency.

The empirical constant X used in the equation for the suspended-sediment reference concentration (equation 6.23) that relates C_{ref} to the wave-induced bed shear stress is an order of magnitude larger at site 7 (h_0 = 35 m) than at site 6 (h_0 = 20 m) (Figure 6-5 and Table 6-2). Hence, for a given wave-induced bed shear stress, more sediment is suspended at site 7. This explains why the mound deflates faster at 35 m depth than at 20 m depth (Table 6-3). However, the pit at 35 m depth does not infill faster than the pit at 20 m depth. The reason is that suspended-sediment transport is proportionately less important to the erosion of the mound than it is to the infilling of the pit.

Figure 6-11 shows predicted time series of pit infilling and mound deflation at h_0 = 20 m. Note that the suspended-sediment trapping efficiency reduces over the duration of the simulation, which is due to the direct dependence of e_s on the ratio d/h_0, which reduces as the pit infills. The mound deflates faster than the pit infills for two reasons. Firstly, the mound stands above the seabed and so it is subject to stronger wave-orbital motions than a pit at the same mean water depth. This difference reduces as the simulation proceeds and the mound is deflated. Secondly, the deflation of the mound is not governed by any trapping efficiency.

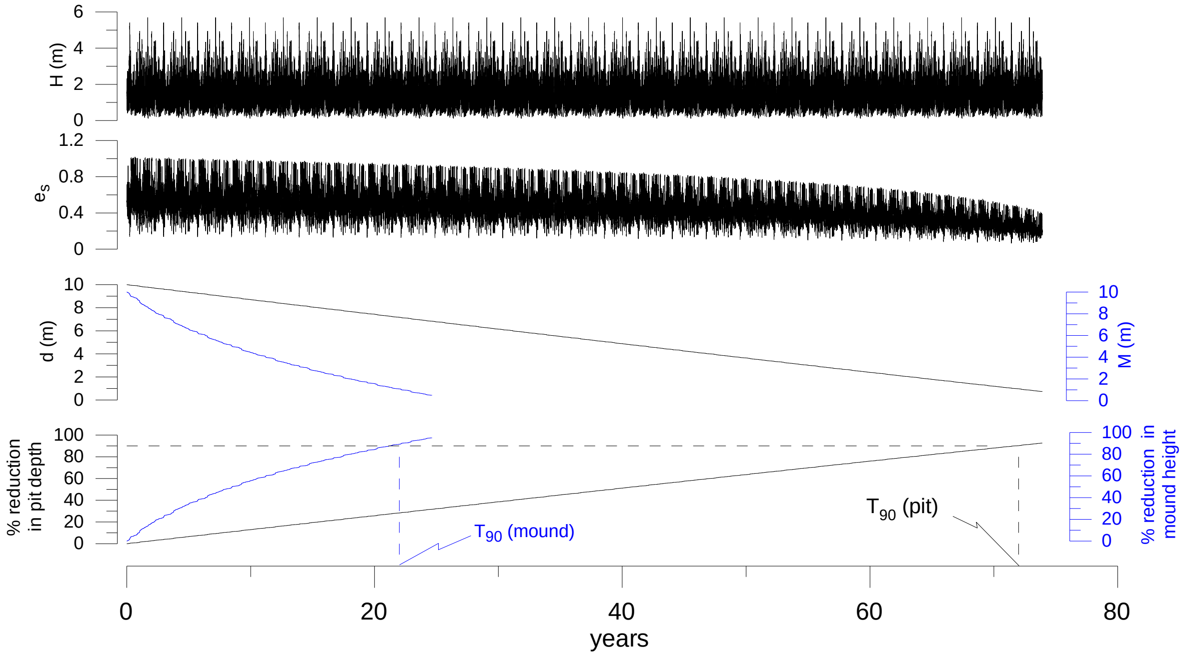

Figure 6-11: Predicted time series of pit infilling (black) and mound deflation (blue) at h_0 = 20 m. Also shown are significant wave height H and suspended-sediment trapping efficiency e_s.

Our predictions of pit infilling at h_0 = 20 m for the South Taranaki Bight are very similar to van Rijn's (2005) summary of observations of pit infilling rates (Table 6-1), which shows a filling timescale of about 100 years at water depths of 15 to 25 m. This does give us confidence in our predictions. For depths greater than 25 m, infilling is only "minor" according to van Rijn, which also corresponds to our prediction of pit infilling at h_0 = 50 m of about 500 years.

It is difficult to say whether our predictions are conservative (in the sense that they are likely to overestimate infilling and deflation times) or the opposite. Where possible, we have chosen and adjusted (by the choice of empirical coefficients) the sediment transport equations that we used based on South Taranaki Bight field data. Had we neglected the reduction in suspended-sediment trapping efficiency that occurs as pits infill, then we would certainly have underestimated the pit infilling time. However, we did account for that, albeit by interpolating van Rijn's graphs. Our assumptions regarding the angle at which sediment transport impinges on the pit are likely to result in us overestimating the pit infilling rate, and therefore underestimating the pit infilling time. We assumed that α_s and α_b were always 90 degrees, based on the modelling of a square pit. Since the sediment transport rate impinging on the pit is $q_s \sin\alpha_s + q_b \sin\alpha_b$, in this case the infilling rate is maximum ($\sin 90^o = 1$). However, where the pit is greatly elongated in one direction or the other, the sediment transport rate impinging on the pit will be less than the sediment transport rate on the surrounding seabed. We understand, however, that pits are likely to be aligned approximately perpendicular to the shoreline, which is also approximately perpendicular to the typical sediment-transport direction anyway, in which case α_s = α_b = 90 degrees.

In summary, the model predicts that at 50-m water depth it will take around 500 years for waves and currents to reduce the pit volume by 90% (around 300 years for 50% reduction). The model predicts that, at the same depth, it will take around 350 years for 90% of the mound to be deflated (150 years for 50% deflation). Infilling and deflation will be faster at 35-m water depth: 100 years for 90% infilling of the pit (50 years for 50% infilling), and 20 years for 90% deflation of the mound (10 years for 50% deflation).

7 Potential effects of sand extraction on geomorphic character, erosion and physical drivers and processes

This section addresses questions posed in the Introduction about how sand extraction activities as they relate to consenting requirements may:

- Adversely affect natural landforms, physical drivers, erosion, geomorphic character, influences that humans have and/or are having on the coast.
- Adversely affect public access to the marine environment.
- Involve the deposition of substances to the foreshore and seabed (such as mud deposition on the beaches from the dredge plume).
- Adversely affect physical drivers and processes that cause coastal change.
- Adversely affect the risk of accelerated coastal erosion or accretion along the regions coastline.
- Modify natural hazard processes.
- And whether the effects of climate change and associated sea level rise will affect any of the above.

7.1 Effects on natural landforms and geomorphic character

Studies were made of the natural landforms and geomorphic character along the 140 km stretch of coast between Opunake and Whanganui.

The near-vertical sections of 30 – 50 m tall cliffs along 70% of the coast owe their geomorphic character to their geology and uplift by tectonic activity and the natural processes of waves attack, weathering and gravitational failure that cause them to erode. Their character will not change with sand extraction. What could potentially change is the rate of erosion of the cliffs if the buffer of beach sands and gravels at their toe is stripped away from the base of the cliffs by the sea – either because the sand supply from the offshore shelf is reduced or because more wave energy is focussed onto the shore.

The beaches at the base of the cliffs owe their geomorphic character in part to their environmental setting. Sand is able to “park-up” in re-entrants on the shoreline (such as the small valleys where streams emerge on the coast) where there is some protection from wave energy provided by the re-entrant. These beaches are able to survive even large storm events when waves overwash the upper part of the beach and reflect off the cliffs eroding sediment above high tide level. They rebuild during calmer periods when low swell brings sand ashore. Sand also accumulates at river mouths such as Patea, where the flood and ebb of the tide traps sand forming sand bodies known at tidal deltas. Further south, where the beaches front low lying topography e.g., Waiinu, sand dunes form where sand is blown inland over low terrain by the strong prevailing SW winds. These environmental settings and their associated geomorphic features are common around the world and their overall geomorphic character will not be affected by offshore sand extraction.

Besides environmental setting, the geomorphic character of beaches around the world is determined by tide range, grain size and wave climate (or more specifically breaker height at the shore) as described in the beach state model of Short (1991 and 1999).

The grain size of sediment on the beaches is unlikely to change with sand extraction offshore. The medium-coarse sands and gravelly sands forming the beaches have as their primary source river inputs and cliff erosion (providing the coarser material), and also sand being fed in from the sea. The composition (the proportions of sand and gravel) of the river and cliff sediment inputs will not change with sand extraction offshore. Our observations show that under existing conditions the grain size of sediment on the beaches changes as fresh sediment is delivered to the beach by rock falls and slumping of the cliffs. This material is then broken down by the waves and distributed along the shore. Sand extraction and subsequent processing of the seabed sediment to extract the iron ore will result in slightly finer sand size material being returned to the seabed. However we have shown that there is little connection between sand at the extraction site some 22 to 35 km offshore and that on the beaches. For these reasons extraction is unlikely to significantly affect the grain size of sediment on the beaches which in general are formed of coarser material (medium to coarse sands). The slope of beaches is primarily determined by the grain size, so if grain size does not change then the slope of the beach will remain unchanged.

7.2 Effects on public access to the marine environment

If sand extraction operations were to cause erosion of the shore and access ways then public access to beaches could be hindered for vehicles and bikes.

All of our studies suggest that coastal erosion will not change significantly in the future with sand extraction offshore and therefore public access to the marine environment will not be hindered. However, continual cycles of cut and fill on the beaches due to natural events will hinder access from time to time as they have in the past.

7.3 Effects from deposition of substances to the foreshore and seabed

The plume modelling (Hadfield 2013) demonstrates that the very fine sands and muds (silt + clay size material) generated by sand extraction operations drifts primarily southeast from the dredging site and to the shore and that some of it accumulates on the seabed in the nearshore in the region of Patea and Wanganui. The issue addressed here is “Will this make the beaches muddy?”

Hadfield (2013) presents maps of the suspended sediment concentrations (SSC) associated with the plumes from the extraction operation. Figure 7-1 shows near-bottom concentrations for Source (A) at the landward end of the extraction operation, mapped as the model median and 99th percentile of the SSC time series at each model grid point, evaluated over the final 2-years of the simulation. The 99th percentile (indicating where the SSC is less than the given value for 99% of the time) is chosen as a robust indicator of the high end of the concentration distribution while the median represents typical values. The figure shows the plume has highest SSC values at the source and are 10 – 20 mg/L (median) and 100 mg/L (99^{th} percentile). Highest values at the coast are 6 – 10 mg/L (median) and 60 – 100 mg/L (99^{th} percentile). The plume footprint has approximately the same shape on the bottom as at the surface, but the surface concentrations are far less than those near the seabed.

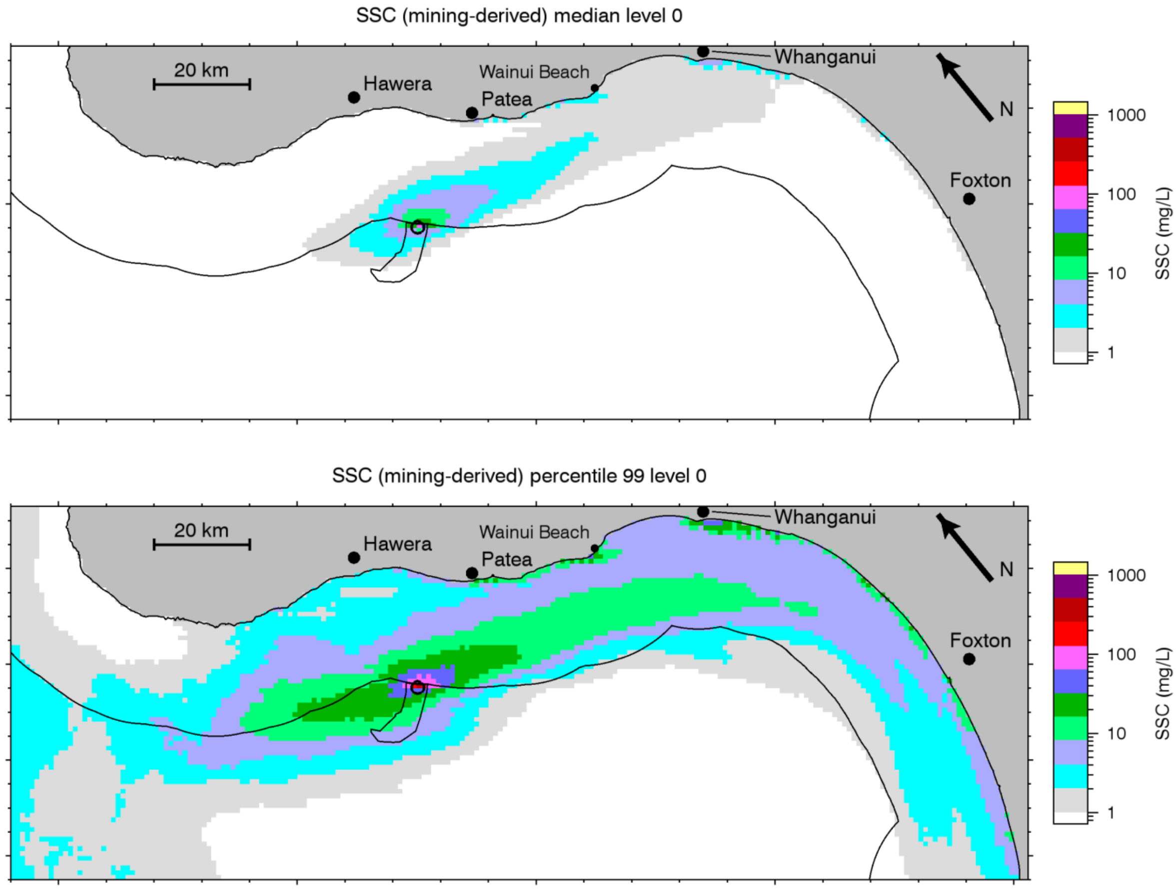

Figure 7-1: Bottom concentration of extraction-derived sediment (source A). The source location is indicated by a black, open circle at the north end of the extraction area. Top plot shows median (50th percentile) suspended sediment concentration; bottom plot shows the 99th percentile. (Source Hadfield 2013).

Our observations made during the beach profile monitoring (MacDonald et al. 2012) show that very energetic wave conditions at the shore during storm events continually rework sand in the beach. During the 12-month long beach monitoring period we never observed mud layers on the beaches, nor was it observed in pits dug in the beaches where we would expect to see evidence of historical mud deposition preserved. Our grain size analyses found that the mud content of the beach sediment was everywhere less than 1 %. There was a complete lack of mud on the beaches despite that fact that river flood events deliver 2 M m^3 of fine sediment and turbid water to the shoreline and adjacent to beaches we surveyed (Table 2-2 and Figure 2-14).

In summary, very fine sands and muds generated by sand extraction operations will not make the beaches muddy. While sediment plumes from extraction operations will reach the shore the absence of mud from existing beach sediments, even close to the sites of river inputs, indicates that if deposited on the beaches fine sediment will be quickly winnowed from the beach sediment by wave action and transported offshore not build-up on the beach.

7.4 Effects on physical drivers and processes that cause coastal change – Currents and cross shelf sand transport

Throughout the study area the prevailing current flows in a direction (NW to SE) that parallels the shoreline and shelf depth contours. Currents reach speeds of 0.3 – 0.4 m/s at peak flow of the tides and large current speeds of around 1 m/s were measured on a number of occasions during periods of high winds. During strong winds, currents could set in a constant direction for more than 24 hours; during calm conditions, currents reversed approximately every 6.2 hours with the tides re-asserting dominance. The currents deviate locally in the vicinity of the large shoreface attached and unattached ridges on the seabed. Bathymetric irregularities such as the pits (to 10 m deep) and mounds (to 9 m tall) at the extraction sites form features of the order of several kilometres long and 0.5 km wide and of a similar size to naturally occurring ridges on the seabed. While producing a localized effect on currents they are not expected to impact prevailing or ambient currents and flow characteristics.

Currents on the inner shelf are the principle mechanism for driving sediment toward the shore and the surf zone (the area of breaking waves in the nearshore) where wave dominated currents transport sediment back and forth along the shoreline and also in the offshore and onshore direction beaches. Sand coming ashore by this mechanism can nourish the beaches. The potential source of seabed sands to nourish the beaches extends well beyond the sand extraction area and is potentially vast. If for instance, seabed sands were supplied from all the seabed within the 30 m isobath, then assuming an average width of seabed to the 30 m isobath of 20 km, then over the 120 km of coast under consideration the potential seabed area that can supply sand to the shoreline is of the order of 2,400 square kilometres. If the onshore flux added over the whole 120 km long study shoreline amounted to a significant component of the littoral budget, then extraction over an 8 km wide (in a NW – SE direction) sand extraction zone would only intercept a relatively small proportion of the onshore flux from about of this zone. If pit infilling is very slow then the amount of interception will be even less.

A key question is the nature of the connection between seabed sediments in the extraction area and the surf zone, and is seabed sand in the area of the extraction operations some 22 to 35 km off the coast a significant source for sand on the beaches? And, if it is, will sand extraction diminish the supply to the beaches and promote beach erosion?

While the principle current direction is strongly shore parallel there are only very weak cross shore flows. This suggests that sediment transport will predominantly be back and forth along that principal axis rather than across the shore. Long (2-year) model simulations incorporating tide, wind and oceanic forcings show that the time-averaged water movements at the extraction site are very weak and of the order of 1 – 2 cm/s and are directed primarily SE, deviating only locally from that path as currents are steered about large ridges on the seabed. Between the project area and the shore the mean current is very weak (<1 cm/s) and directed towards the shore between Hawera and Patea, while further east of Patea it is directed more to the east. The net current patterns suggest only a weak connection between sands at the extraction site and sediment at the shoreline.

The 2-year simulations that were run with the plume model over a patch of sand in the extraction area show that while sand at the extraction site gets lifted into suspension reasonably often, it is primarily advected to the SE and it doesn't travel far before it is deposited again. The patterns of distribution of both the suspended sediment transport and deposition indicate that seabed sediment is not distributed far from the site, and that the transport of sand to the shore from this site (or a deficit therein) will take a lot longer than 2 years.

In summary, it would appear that there is little connection between seabed sediments in the extraction area and the surf zone, and seabed sand in the area of the extraction operations some 22 to 35 km off the coast is not a significant source for sand on the beaches. This suggests that sand extraction will not have significant effects on sand supply to the beaches and will not promote beach erosion.

7.5 Effects on physical drivers and processes that cause coastal change – Waves

The proposed sand extraction operations will result in pits, elongate depressions (lanes) and mounds in the seabed. The effects of these on wave conditions were addressed by nearshore numerical wave modelling as described in Section 5.3 above, and more fully reported in Gorman (2012, 2013). Note that, as described earlier, climate change will have little effect on the wave climate so that the predictions made here will be unaffected by climate change.

Scenario-based simulations

This first part of this work considered eight potential cases of bathymetry modification consistent with the sand extraction plan. Of these, case 1 represented the “worst case” with the most extensive possible modifications at the completion of all extraction operations. Other cases represented a range of possible intermediate seabed configurations.

The effects of these bathymetry modifications on wave conditions were then tested by running short model simulations under six scenarios of offshore wave conditions, representing a range of input directions and representing storm as well as moderate conditions (Table 5-1). It also compared the resulting wave parameters with those in a corresponding baseline simulation (i.e., unmodified bathymetry).

The maximum changes in significant wave height, observed in the vicinity of the extraction operations, were found to range between 0.09 and 0.44 m, or 4.6 – 12.6% of the baseline values, for the eight bathymetry modification cases.

At the 10 m isobath, which is about the seaward edge of the surf zone, the changes in wave characteristics due to extraction are much smaller than the changes further offshore. The magnitude of change as a percentage of the baseline value show changes in significant wave height remain less than 9.2% for the maximal case 1 bathymetry modifications, and less than 4.8% for other cases. Case 1 is a worst case situation where large pits and mounds occur at the start of every lane. This assumes that the pits will not infill and the mounds will not slump or be eroded by waves and currents to any degree over the time that it takes to extract from the whole area (perhaps 10 years). Changes in wave direction are generally less than 1 degree, increasing locally to 3 degrees west of Manawapou. This is insignificant when compared to the variability in wave approach throughout the year (refer to Figure 5-4 and Figure 5-5).

The overall conclusion from the scenario-based modelling is that the proposed sand extraction operations will have only minor effects (discounting case 1) on the physical driver of waves by refraction (bending the wave path) and diffraction (lateral dispersion of wave energy) and locally by shoaling (changing the wave height) them as they pass over the modified seabed. The changes in both wave height and direction are very small.

Long-term simulations

A 12-month long simulation which allows for the effects of the bathymetry modifications on the wave characteristics to be tested for case 1 (representing the most extensive possible bathymetry modifications) over a wide sampling of the local wave climate, provided a full time series outputs of wave statistics on the 10 m isobath.

This showed that the bathymetry modifications introduce a mean decrease (by < 5 cm) in significant wave height on the coast near Patea, with smaller increases (of < 2.5 cm) further west. The individual scenarios are consistent with the yearly averages, which generally correspond to the lower end of the range of variability covered by the scenarios. Similar results apply to mean wave direction and bed orbital velocity, while the bias in mean period differs from zero by somewhat less than one standard deviation. Mean wave period decreases (by < 0.1 seconds) in the vicinity of Patea, and increases (by < 0.06 seconds) to the west. Mean wave direction is slightly decreased (i.e., changes in an anticlockwise sense) on average along the majority of the coast, as far east as Waverley, beyond which there is zero change. For all four variables, this range of variability in the differences associated with the bathymetry changes is considerably less than the corresponding natural range of variability in baseline values illustrated in Figure 5-21. These small changes are also reflected in other statistical measures such as:

- the root-mean-square difference (RMSD), between case 1 and baseline statistics, which shows the typical wave height differences of < 2.0 cm for much of the coast, up to a maximum of 5.5 cm near Patea
- the mean relative magnitude difference, which shows changes < 2.7% for significant height and mean period, and
- dividing the root-mean-square difference by the standard deviation (SDh), which shows changes < 8% of one standard deviation (SDh) for significant wave height, < 15% of one standard deviation for mean period and < 10% of one standard deviation for bed-orbital velocity.

In summary, both the scenario-based simulations and the long term simulations of changes in wave climate show that the bathymetry modifications due to sand extraction will have only very minor effects on the wave characteristics landwards of the extraction site and that the range of variability in the differences associated with the bathymetry changes is considerably less than the corresponding natural range of variability in baseline values.

7.6 Effects on physical drivers and processes that cause coastal change – Longshore and cross shore transport

Longshore transport is the process by which waves arriving at an angle to the shore drive sediment along the shore. The sediment is driven along and across the beach face and also through the surf zone, which on an energetic coast like the South Taranaki Bight extends at times from the swash zone seawards to about the 10 m depth contour. Longshore transport is a primary mechanism for supplying sand to beaches from sources alongshore (e.g., rivers, eroding seacliffs) and is also a mechanism for taking sand away. Gradients in longshore transport can either lead to accretion or erosion, depending on their sign. A key issue for this study is to establish an acceptable level of change in longshore transport and impact on the shoreline due to offshore extraction.

There have been a number of studies of the effects of sand extraction pits on wave climate and adjacent beaches associated with borrow pits for beach nourishment projects in the USA. In many recent studies, wave modelling has been used as a tool to optimise pit design (depth of cut, pit shape, water depth, distance of pit from the shore e.g., Benedet et al. 2013), assess and the physical and biological effects on the shore (e.g., Byrnes et al. 2004) and evaluate shoreline response and quantify the significance of potential environmental impacts (Kelley et al. 2004). Relevant to this study is the work by Kelley et al. (2004), which undertook a detailed analysis of the inter-annual wave climate, beach profile change and sediment transport variability along shorelines in New Jersey, North Carolina and Florida. They came up with a criterion for “accepting” or “rejecting” a potential sand borrow (extraction) site based on a range of one-half standard deviation ($\pm 0.5s$) about the mean (m) of the longshore transport potential. We adopt that approach to establish whether the proposed sand extraction by TTR is “acceptable”.

The analytical approach of Kelley et al. (2004) incorporates analysis of nearshore wave transformation and wave-induced longshore sediment transport. Calculation of longshore sediment transport potential for a series of wave cases provided a method for determining the extent and magnitude of alterations to nearshore processes, but the magnitude of change alone did not provide enough information to determine the significance of changes for a particular coastline. Therefore wave modelling was performed at three locations (New Jersey, North Carolina and Florida) for the entire 20-year wave hindcast time series and for 20 one-year-long blocks of the wave record. The annual and overall averages were calculated, the standard deviation of the annual averages was calculated, and longshore sediment transport potential was determined every 200 m along the shoreline. Assuming the temporal component of sediment transport potential is normally distributed, the suggested criterion for accepting or rejecting a potential extraction site was based on a range of one-half a standard deviation ($\pm 0.5s$) about the mean (m).

This normal distribution simplifying assumption is based on comparisons relative to the distribution of wave energy approaching a shoreline. If any portion of the curve between average sediment transport potential versus distance alongshore associated with a sand extraction project crosses outside a band $\pm 0.5s$ about the equivalent curve for existing (pre-dredging) conditions, the site would be rejected. In a Normal distribution, half a standard deviation (s) incorporates approximately 38% of the variability. Therefore, for s determined from 20 one-year model runs, there is a 62% chance that the mean transport for any given year will fall outside the $\pm 0.5s$ envelope about the mean, and an 85% chance of falling outside this envelope during any two-year period. The envelope provides a basis for judging the impacts of a borrow site relative to natural variability of the sediment transport climate along a coastline. Because there is a greater than 50% chance that the transport computed for a particular year will fall outside of the $\pm 0.5s$ envelope about the mean, impacts determined for a particular borrow site that fall within this envelope likely will be indistinguishable from observed natural variations. For this reason, sites with large natural variation in wave climate and associated sediment transport potential could sustain greater impacts associated with an offshore sand extraction project.

In section 5.3.4 we reported the results of long-term wave climate simulations, undertaken in a similar manner to Kelley et al. (2004), although noting that we undertook a one-year simulation compared to Kelley et al's 20 years, and hence characterised natural variability through standard deviation (SDm) of monthly rather than annual means. This provided various statistics on longshore wave energy flux and sediment transport potential. The results, summarised in Figures 5.26 to 5.34 show the difference in wave energy characteristics and sediment transport potential at the shore for the existing (baseline) seabed condition versus the post-sand extraction situation for case 1. This case represented a worst case situation in terms of potential effects on the shore, as it contains the greatest number of pits and mounds and represents extraction over 10 years with no pit infilling or mound deflation or slumping by natural processes. The graphs have plotted on them the $\pm 0.5s$ envelope about the mean. It can be seen that the differences in longshore wave energy flux and sediment transport potential as a consequence of the proposed extraction, lie well within the envelope. That is to say, the extraction proposed by TTR for the case 1 situation meets the Kelley et al. (2004) criterion for "accepting" a sand extraction site.

A shoreline like the South Taranaki Bight that experiences a wide variety of wave conditions (see Figure 5-4 and Figure 5-5) will experience large variability in sediment transport rates and changes in sand storage on the beaches. The large variability in processes is also contributed to by changes in the alignment of the coast orientation along the shore, headlands, and ridges and banks on the inner shelf which bend and refract waves approaching the shore. It follows therefore that the level of acceptable impacts from sand extraction offshore should be relatively high on this type of shore, compared for instance to a shore that experiences a more limited range of wave conditions.

7.7 Effects on the risk of accelerated coastal erosion and accretion along the region's coastline and modification to natural hazard processes

Beach profile surveys and observations made at eight sites between Ohawe and Kai Iwi, spanning a stretch of about 70 km of coast show that the beaches are very active. The profiles were surveyed over an 11 month period (providing 352 profile records), and captured a wide range of wave conditions including sizeable storm events. The level of the beach fluctuates up and down 1 – 2 m and the beach face shows excursions back and forth of about 10 – 40 m over time scales of weeks and months in response to erosion during storm events and the calmer periods of beach building in between. Active beach building is evidenced by swash bars on the lower beach (waves of sand 0.6 m tall and 30 m long) coming ashore and by slugs of sediment in low, broad, shore-normal waves of sand. These large fluctuations in the storage of sand along the shore are primarily a function of changes in the physical forcings by waves incident at the shore in response to changing patterns in swell and wind generated waves from the Southern Ocean and Tasman sea. The beaches of the South Taranaki Bight are characterised by considerable erosion and accretion over short time scales (months and probably years) under natural conditions (no extraction) as a consequence of this environmental setting. Changes in wave characteristics due to pits and mounds on the seabed resulting from sand extraction operations some 22 – 35 km offshore have been shown to have no significant influence on the wave climate in the nearshore. The extraction site has been shown to have no significant connection with the coast in terms of sand supply. It follows that sand extraction offshore will have no significant effect on the beaches in terms of the natural processes of erosion and accretion which under natural conditions induce substantial variability in beach size and condition.

8 References

Anderson, T., MacDiarmid, A., Stewart, R. (2013) Nearshore epibenthos and surficial sediments of the South Taranaki Bight. Report prepared for Trans-Tasman Resources Ltd. *NIWA Client Report* No: NEL2013-012: 43.

Bailard, J.A. (1981) An energetics total load sediment transport model for a plane sloping beach. *Journal of Geophysical Research,* 86: 10938–10964.

Beaumont, J., Anderson, T.J., MacDiarmid, A. (2013) Benthic flora and fauna of the South Taranaki Bight. *NIWA Client Report* No: WLG2012-55: 187.

Benedet, L., Finkl, C.W., Dobrochinski, J.P.H. (2013) Optimisation of nearshore dredge pit design to reduce impacts on adjacent beaches. *Journal of Coastal Research,* 29(3): 519–525.

Boers, M. (2005) Effects of a deep sand extraction pit. *Final report of the PUTMOR measurements at the Lowered Dump Site,* RIKZ/2005.001.

Byrnes, M.R., Hammer, R.M., Thibaut, T.D., Snyder, D.B. (2004) Physical and biological effects of sand mining offshore Alabama, U.S.A. *Journal of Coastal Research,* 20(1): 6–24.

Carter, L. (1980) Ironsand in continental shelf sediments off western New Zealand – a synopsis. *New Zealand Journal of Geology and Geophysics,* 23: 455–448. DOI:10.1080/00288306.1980.10424116

Chesher, T.J., Soulsby, R.L., Foley, W.J. (2005) Scenario Testing Approach and Results for Sand Mining Pits. SANDPIT, Sand Transport and Morphology of Offshore Sand Mining Pits. Final report. Brussels, Belgium: European Union Commission. *EC Framework V Project.* No. EVK3-2001-00056: A1–AO14.

Coastal Explorer. http://wrenz.niwa.co.nz/webmodel/coastal. NIWA website.

Cowie, N.A., Healy, T.R., McComb, P.J. (2009) Sediment Flux on the High Energy Taranaki Coast, *New Zealand. Journal of Coastal Research*, Special Issue 56: 703–707.

de Lange, W., Healy, T. (1994) Assessing the stability of inner shelf dredge spoil mounds using spreadsheet applications on personal computers. *Journal of Coastal Research,* 10(4): 946–968.

Gonzalez, M., Medina, R., Espejo, A., Tintore, J., Martin, D., Orfila, A. (2010) Morphodynamic evolution of dredged sandpits. *Journal of Coastal Research,* 26(3): 485–502.

Gorman, R.M. (2012) South Taranaki Bight Iron Sand Mining Nearshore Wave Modelling: Phase 2 and Phase 3 Studies. Report prepared for Trans-Tasman Resources Ltd. *NIWA Client Report* No: HAM2012-141: 238.

Gorman, R.M. (2013) South Taranaki Bight Iron Sand Mining Nearshore Wave Modelling: Phase 4 Studies. Report prepared for Trans-Tasman Resources Ltd. *NIWA Client Report* No: HAM2013-091: 146.

Green, M.O. (1999) Test of sediment initial-motion theories using irregular-wave field data. *Sedimentology*, 46: 427–441.

Green, M.O., Black, K.P. (1999) Suspended-sediment reference concentration under waves: field observations and critical analysis of two predictive models. *Coastal Engineering*, 38: 115–141.

Hadfield, M. (2012) Sediment Plume Modelling for South Taranaki Bight Ironsand Mining. Phase 3 interim report prepared for Trans-Tasman Resources Ltd, October 2012. *NIWA Client Report* No: WLG2012-51: 52.

Hadfield, M. (2013) South Taranaki Bight iron sand extraction sediment plume modelling. Phase 3 studies. Report prepared for Trans-Tasman Resources Ltd, July 2013. *NIWA Client Report* No: WLG2013-56: 59.

Hume, T., Ovenden, R., MacDonald, I. (2012) Coastal stability of the South Taranaki Bight – Phase 1 Historical and present day shoreline change. Report prepared for Trans-Tasman Resources Ltd. *NIWA Client Report* No: HAM2012-083: 89. September 2012: 96.

Idier, D., Hommes, S., Briere, C., Roos, P.C., Walstra, D.-J., Knaapen, M.A.F., Hulscher, S.J.M.H. (2010) Morphodynamic models used to study the impact of offshore aggregate extraction: a review. *Journal of Coastal Research,* SI51: 39–52.

IPCC AR4 WG1 (2007) Solomon, S., Qin, D., Manning, M., Chen, Z., Marquis, M., Averyt, K.B., Tignor, M., Miller, H.L. (ed.). *Climate Change 2007: The Physical Science Basis,* Contribution of Working Group I to the Fourth Assessment Report of the Intergovernmental Panel on Climate Change, Cambridge University Press, ISBN 978-0-521-88009-1 (pb: 978-0-521-70596-7).

Jiminez, J.A., Madsen, O.S. (2003) A simple formula to estimate settling velocity of natural sediments. *Journal of Waterway, Port, Coastal, and Ocean Engineering,* 129(2): 70–78.

Kelley, S.W., Ramsey, J.S., Byrnes, M.R. (2004) Evaluating shoreline response to offshore sand mining for beach renourishment. *Journal of Coastal Research,* 20(1): 89–100.

Komar, P.D., Miller, M.C. (1973) The threshold of sediment movement under oscillatory water waves. *Journal of Sedimentary Petrology,* 43(4): 1101–1110.

Komar, P.D., Miller, M.C. (1975) On the comparison between the threshold of sediment motion under waves and unidirectional currents with a discussion of the practical evaluation of the threshold. *Journal of Sedimentary Petrology,* 45: 362–367.

Lewis, K.B. (1979) A storm-dominated inner shelf, western Cook Strait, New Zealand. *Marine Geology,* 31: 31–43.

Lewis, K.B. (1994) The opening of Cook Strait: Interglacial tidal scour and aligning basins at a subduction to transform plate edge. *Marine Geology,* 116: 293–312.

MacDiarmid, A., Anderson, O., Beaumont, J., Gorman, R., Hancock, N., Julian, K., Schwarz, J., Stevens, C., Sturman, J., Thompson, D., Torres, L. (2010) South Taranaki Bight iron sand mining baseline environmental study. Report prepared for Trans-Tasman Resources Ltd. *NIWA Client Report* No: WLG2010-46.

MacDonald, I., Ovenden, R., Hume, T. (2012a) South Taranaki Bight iron sand mining: Shoreline monitoring data report. Report prepared for Trans-Tasman Resources Ltd. *NIWA Client Report* No: HAM2012-083: 97.

MacDonald, I.T., Budd, R., Bremner, D., Edhouse, S. (2012) South Taranaki Bight Iron Sand Mining: Oceanographic Measurements Data Report. *NIWA Client Report* HAM2012–147, August 2012.

McGlone, M.S., Neal, V.E., Pillans, B.J. (1984) Inaha Terrace deposits: a late Quaternary terrestrial record in South Taranaki, New Zealand. *New Zealand Journal of Geology and Geophysics,* 27: 35–49.

Nielsen, P. (1992) Coastal Bottom Boundary Layers and Sediment Transport. *World Scientific,* Singapore: 324.

Nodder, S. (1993) Neotectonics of the offshore Cape Egmont Fault Zone, Taranaki Basin, New Zealand. *New Zealand Journal of Geology and Geophysics,* 36: 167–184.

Orpin, A., Bostock, H., Bardsley, S., Mackay, K. (2009) Offshore Desktop Study of Prospecting Permits PP 50 383 and PP 50 753, North Island West Coast. *NIWA Client Report* No: WLG2009-21: 45 + app.

Proctor, R., Carter, L. (1989) Tidal and sedimentary response to the late Quaternary closure and opening of Cook Strait, New Zealand: results from numerical modelling. *Paleoceanography,* 4: 167–180.

Ribberink, J.S. (2004) Migration and in fills of trenches in the marine environment: an analytical engineering model. *Report EU Project Sand Pit*. Twente, The Netherlands: University of Twente: 68.

Ribberink, J.S., Roos, P.C., Hulsater, S. (2005) Morphodynamics of trenches and pits under the influence of currents and waves – simple engineering formulas. *In: Proceedings of Coastal Dynamics '05*. Barcelona, A.S.C.E.: 14.

Roos, P.C., Hulscher, S.J.M.H. (2004) Modelling the morphodynamic effects of different design options for offshore sandpits. *Marine Sandwave and River Dune Dynamics,* April 2004, Enschede, Netherlands: 262–269.

Roos, P.C., Hulscher, S.J.M.H., de Vriend, H.J. (2008) Modelling the morphodynamic impact of offshore sandpit geometries. *Coastal Engineering,* 55 (9): 704–715.

Short, A.D. (1991) Macro-meso tidal beach morphodynamics – An overview. *Journal of Coastal Research,* 7: 417–436.

Short, A. D. (editor) 1999 Beach and Shoreface Morphodynamics. *John Wiley and Sons*, Chichester: 379.

Soulsby, R. (1997) Dynamics of Marine Sands. *Thomas Telford*, United Kingdom: 249.

Sousby, R. (1995) Bed shear-stresses due to combined waves and currents. *In: Advance in coastal Morphodynamics*, ed. M.J.F. Stive, H. J. de Vriend, J. Fredsoe, L. Hamm, R. L. Soulsby, C. Teisson and J. C Winterwerp, Delft Hydraulics, Netherlands: 4-20 to 4-23.

Taranaki Regional Council (2009) *Coastal Erosion Information: Inventory and recommendations for state of environment monitoring*: 77. http://www.trc.govt.nz/assets/Publications/guidelines-procedures-and-publications/Coastal/coastal-erosion09.pdf

Tolman, H.L. (1991) A third-generation model for wind waves on slowly varying, unsteady, and inhomogeneous depths and currents. *Journal of Physical Oceanography,* 21: 782–797.

Tolman, H.L. (2007) The 2007 release of WAVEWATCH. *10th International Workshop on Wave Hindcasting and Forecasting and Coastal Hazard Symposium,* North Shore, Oahu, Hawaii.

Uppala, S.M., KÅllberg, P.W., Simmons, A.J., Andrae, U., Bechtold, V.D.C., Fiorino, M., Gibson, J.K., Haseler, J., Hernandez, A., Kelly, G.A., Li, X., Onogi, K., Saarinen, S., Sokka, N., Allan, R.P., Andersson, E., Arpe, K., Balmaseda, M.A., Beljaars, A.C.M., Berg, L.V.D., Bidlot, J., Bormann, N., Caires, S., Chevallier, F., Dethof, A., Dragosavac, M., Fisher, M., Fuentes, M., Hagemann, S., Hólm, E., Hoskins, B.J., Isaksen, L., Janssen, P.A.E.M., Jenne, R., McNally, A.P., Mahfouf, J.F., Morcrette, J.J., Rayner, N.A., Saunders, R.W., Simon, P., Sterl, A., Trenberth, K.E., Untch, A., Vasiljevic, D., Viterbo, P., Woollen, J. (2005) The ERA-40 re-analysis. *Quarterly Journal of the Royal Meteorological Society,* 131 (612): 2961–3012.

van Rijn, L.C. (1986) Sedimentation of Dredged Channels By Currents and Waves. *Journal of Waterway, Port, Coastal and Ocean Engineering*, 112: 541–559.

van Rijn, L.C., Soulsby, R.L., Hoekstra, P., Davies, A.G. (2005) SANDPIT. Sand transport and morphology of offshore sand mining pits. *Process knowledge and guidelines for coastal management*. Aqua Publications, The Netherlands: 716.

WRENZ http://wrenz.niwa.co.nz/webmodel/. NIWA website.

9 Appendix: List of symbols used in section 6

$A_{\mathrm{w,crit}}$	near-bed critical wave-orbital semi-excursion
A_{w}	near-bed wave-orbital semi-excursion
B	pit width or mound width
C_{bed}	ratio of bulk density at which sediment settles in the pit to the density of the suspended-sediment particles, or, the ratio of the density of the mound bed sediment to the mineral density of the suspended-sediment particles
C_{ref}	suspended-sediment reference concentration
C_z	mean suspended-sediment concentration at elevation z above the bed
$C_{D,z}$	seabed drag coefficient referenced to current speed at elevation z above the bed
d	pit depth
D	sediment grainsize
e_{b}	bedload trapping efficiency
e_{s}	suspended-sediment trapping efficiency
E	erosion depth
g	acceleration due to gravity
f'_{w}	skin-friction wave friction factor
f_{w}	wave friction factor (corresponding to the total seabed roughness k_{r})
h	water depth
h_0	mean water depth
H	wave height
k_{r}	total seabed roughness
k_{w}	wavenumber
l_{s}	suspended-sediment mixing length
M	mound height
q_{b}	volumetric bedload transport rate per unit width of seabed normal to the direction of transport
q_{s}	volumetric suspended-sediment transport rate per unit width of seabed normal to the direction of transport
t	time
S	sedimentation depth

T	wave period
T_n	time it takes for d to reduce to $\left(1-\frac{n}{100}\right)d$ or for M to reduce to $\left(1-\frac{n}{100}\right)M$, where n is a percentage
U_{w}	wave-orbital speed at the bed
$U_{\mathrm{w,crit}}$	critical wave-orbital speed for initiation of sediment motion
U_z	mean current speed at elevation z above the bed
$U_{*\mathrm{c}}$	current-induced friction velocity
$U'_{*\mathrm{c}}$	current-induced skin-friction friction velocity
$U_{*\mathrm{w}}$	wave-induced friction velocity (corresponding to the total seabed roughness k_{r})
U_{*0}	bed friction velocity in graphs of e_{s}
V_{bed}	pit migration velocity
w_{s}	sediment settling speed
x	direction parallel to the width of the pit or the width of the mound
X	empirical constant (suspended-sediment reference concentration)
z	elevation above the bed
Z_0	seabed roughness length
α_{b}	angle at which q_{b} impinges on the upstream edge of the pit
α_{s}	angle at which q_{s} impinges on the upstream edge of the pit
Δt	time interval
Λ	empirical constant (suspended-sediment mixing length)
Θ'_{crit}	critical nondimensional skin friction for initiation of sediment motion
Θ'_{m}	mean value of the dimensionless skin friction over the wave cycle in the wave-current bedload model
Θ'_0	amplitude of the oscillatory component of the nondimensional skin friction in the wave-current bedload model
θ'_{w}	dimensionless wave-induced skin friction
κ	von Karman's constant
λ	bedform wavelength
σ	bedform height
ρ	fluid density
ρ_{s}	sediment density
τ'_{c}	current-induced skin friction

τ'_{crit}	critical skin friction for initiation of sediment motion
τ'_{m}	mean skin friction over the wave cycle in the wave–current flow
τ'_{w}	wave-induced skin friction
Φ_{b}	dimensionless bedload transport rate
Φ_x	component of Φ_{b} in the direction of the current
Φ_y	component of Φ_{b} at right angles to direction of the current
ψ	acute angle between the wave and the current
ψ_{c}	direction of the current (setting to)
ω	wave radian frequency
λ	seabed bedform wavelength